OPTIMIZATION OF DIESEL ENGINE AND AFTER-TREATMENT SYSTEM FOR SERIES HYBRID FORKLIFT APPLICATION

By

ROMAN MAHARJAN

A THESIS

Submitted in partial fulfillment of the requirements for the degree of

MASTER OF SCIENCE

In Mechanical Engineering – Engineering Mechanics

MICHIGAN TECHNOLOGICAL UNIVERSITY

2019

This thesis has been approved in partial fulfillment of the requirements for the Degree of MASTER OF SCIENCE in Mechanical Engineering- Engineering Mechanics.

Department of Mechanical Engineering – Engineering Mechanics

Thesis Advisor: *Dr. Mahdi Shahbakhti*

Committee Member: *Dr. Jeffrey D. Naber*

Committee Member: *Dr. David D. Wanless*

Department Chair: *Dr. William W. Prebedon*

Table of Contents

List of Figures

List of Tables

Preface

The work presented in this thesis is accomplished with validated sub-models provided by IAV GmbH. NOx model and predictive DI-pulse combustion model validated by IAV GmbH for similar application are employed to study engine performance and emissions. Wall thermal layer property model for the catalyst is used to predict heat transfer of catalyst component accurately. The engine model developed in this study is validated against the experimentally validated IAV engine model data. Along with that, the vehicle model specification for forklift in this study is also provided by IAV GmbH, which has been implemented in the GT-Suite® simulation environment to study the performance of designed series hybrid powertrain.

Acknowledgments

I would like to thank my advisor, Professor Mahdi Shahbakhti, for giving me the opportunity to learn about this project, and I appreciate his tremendous support, encouragement, and guidance to complete it.

I am grateful to my seniors of IAV Automotive Engineering Dr. Yinyan Huang, Dr. Thaddaeus Delebinski, Dr. Salem Al-Assadi, and John Cergnul along with seniors of IAV GmbH Dr. Reza Rezaei and Rico Moellmann for their guidance during my entire work.

Thanks to Dr. Jeffrey D. Naber and Dr. David D. Wanless for allocating their valuable time to serve on my committee.

Also, I would like to thank my friends, Ashish Wagh, Sumit Shrestha, Binay Pandey, Arun Sanjel, Sumit K. Shrestha, and Anil Silwal for their valuable suggestions and support to accomplish my thesis work.

Finally, I would like to express my deep sense of gratitude to my parents, brother, and sister for their support and prayers throughout my life.

Nomenclature

Symbol	Unit	Description
g	m/s^2	Gravity constant
f_R	-	Rolling resistance coefficient
A	m^2	Front Area
C_A		Air drag coefficient
ρ_A	kg/m^3	density of air
$\emptyset$	radian	Maximum road grade
V_{oc}	Volt	Open circuit Voltage
P	kW	Power
m	kg	Mass
$\dot{m}$	kg/hr	Mass flow rate
v	m/s	Vehicle speed
t	s	Time
R_{cell}	ohm	Resistance of cell
CA	degrees	Crank Angle
T	$K/^0C$	Temperature
H	-	efficiency
V	liter	Volume
$P_{cyl,max}$	bar	Maximum cylinder Pressure
T_a	K	Activation temperature
A		Pre-exponent Multiplier
T_{max}	N-m	Maximum Brake Torque
RPM_{max}	Rev/min	Maximum motor speed
N_p	-	Number of cells in parallel
N_s	-	Number of cells in series

P_{Max}	kW	Maximum Available Power
$P_{traction}$	kW	Traction Power demand
Acc_{vehicl}	m/s^2	Vehicle acceleration
$Limit_{regen}$	kW	Regenerative Braking limit
C_{ent}	-	Calibration constant for entrainment multiplier
C_{ign}	-	Calibration constant for ignition delay
C_{pm}	-	Calibration constant for pre-mixed phase
C_d	-	Coefficient of discharge for injector nozzle
$Vcyl$	-	Cylinder volume
S	m	Spray penetration length
u_{inj}	m/s	Injection velocity
t_{ign}	s	Injection delay
ρ_l	Kg/m^3	Density of fuel
m_{inj}	kg	Mass of injected fuel
ΔP	Pa	Pressure difference
k	-	Reaction rate constant
λ	-	Air-fuel equivalence ratio
C_{df}	-	Calibration constant for diffusion multiplier
T_b	K	Burned sub-zone Temperature
Q	W	Convective heat transfer rate
h	W/m^2K	Convective heat transfer coefficient
α	-	Weighting coefficient
T_u	K	unburned zone temperature
T_g	K	Effective gas temperature
T_w	K	Wall temperature
ρ	kg/m^3	density

List of Abbreviations

AC	Alternating Current	DOC	Diesel Oxidation Catalyst
AFR	Air Fuel Ratio	DOE	Design of Experiments
ATDC	After Top Dead Center	DPF	Diesel Particulate Filter
BMEP	Brake Mean Effective Pressure	EGR	Exhaust Gas Recirculation
BMS	Battery Management Systeme	EGT	Exhaust Gas Temperature
BSFC	Brake Specific Fuel Consumption	EPA	Environmental Protection Agency
BSHC	Brake Specific Hydrocarbons	EV	Electric Vehicles
BSNOx	Brake Specific Nitrogen Oxides	FDR	Final Drive Ratio
CA deg.	Crank Angle degree	HC	Hydrocarbon
CARB	California Air Resource Board	HEV	Hybrid Electric Vehicle
CD	Charge Depleting	ICE	Internal Combustion Engines
CI	Compression Injection	IPM	Interior Permanent Magnet
CO	Carbon Monoxide	Li-ion	Lithium-ion
CO_2	Carbon dioxide	MPRR	Maximum Pressure Rise Rate
COV	Coefficient of Variation	NH_3	Ammonia
CS	Charge Sustaining	NOx	Oxides of Nitrogen
Cu-CHA	Copper Chabazite	NO	Nitrous oxide
DC	Direct Current	NO_2	Nitrogen dioxide
DEF	Diesel Exhaust Fluid	NMHC	Non-Methane Hydrocarbon

O_2	Oxygen	SAE	Society of Automotive Engineers
OCV	Open Circuit Voltage	SCR	Selective Catalytic Reduction
PM	Particulate Matter	SOC	State of Charge
PN	Particle Number	SOI	Start of Injection
PGM	Precious Group Metal	SVR	Swept Volume Ratio
RPM	Revolution Per Minute	VDI	Verband Deutscher Ingenieure

Abstract

More and more off-highway applications take advantage of hybridization using hydraulic or electric hybrid systems to increase the productivity and efficiency of the machines. The application of interest for this study is forklift that consists load cycle with intermittent peak load, which can provide the maximum benefits utilizing an optimum hybrid powertrain layout. In addition to this, there is also an interest to reduce tailpipe emissions or create a zero-emission solution due to strict emission regulations. Therefore, diesel engine performance and the after-treatment system are optimized in this thesis for a series hybrid forklift application in GT-Suite® simulation environment for fuel consumption benefits and emission reduction.

A GT-Suite® holistic modeling approach is utilized to establish a model-based hardware definition for an engine and after-treatment system that would accurately predict engine performance and emissions of the system. The developed engine model performance is validated with the experimentally verified IAV engine model data used for a similar application. The engine is optimized at a single operating point for optimal fuel consumption considering the performance of the after-treatment components. In addition, the effect of thermal management strategy like retarding injection timing and late post-injection of fuel during cold start is studied. The result shows tailpipe-NOx emission can be reduced by 40% by retarding the injection timing 15 CA deg. ATDC. Along with that, a series hybrid powertrain is designed to represent the series hybrid forklift architect with a heuristic-based controller that defines different modes of operation. The developed hybrid powertrain system can meet the performance requirement for 20% gradeability.

The energy utilization for a developed series hybrid forklift in VDI 2198 cycle is mainly used for the vehicle rolling resistance as the vehicle mass including the rated load is high equivalent to 5.90 kW-hr. The energy required to overcome drag is only 0.01 kW-hr due to low vehicle speed in the cycle. The fuel consumption of conventional forklift is

compared with a developed series hybrid forklift for the 60 VDI 2198 cycles, which shows reasonable fuel saving. The result shows optimally designed hybrid electric forklift can minimize fuel consumption by 20%. Furthermore, the cost of after-treatment components can be reduced by 19.7% using smaller catalyst volume for a single point operating diesel engine.

Chapter 1: Introduction

1.1. Background

Heavy-duty machinery encompasses a wide variety of vehicles and is generally manufactured for intensive use, often a repetitive task for several hours. These vehicles have a significant impact on global fuel consumption and emissions as fossil fuels are used as the primary source of energy. This has led to faster depletion of oil resources, and the growth in global oil demand is also increasing. In the US alone, diesel fuel consumption for construction equipment in 2005 was over 6 billion gallons per year [1]. And the fuel consumption will be continuously increasing because of the current market demand for the construction machinery. The growth has been projected to be 8.9% for these vehicles by 2025 [2]. So, the companies like Volvo, Toyota, Hyundai, Mitsubishi, Still, etc. are moving toward the electrification that offers a reduction of noise, emission and energy, operating and maintenance cost over the conventional combustion engine powertrain.

Forklifts are a type of construction vehicles that are primarily used for lifting and moving heavy loads to different locations in warehouse, shops or work sites. These vehicles can be classified into many categories, but they can be mainly grouped by the energy source: Internal combustion engine (ICE) forklift and electric forklift. These forklifts have their advantages and disadvantages depending on their application, price, operation, maintenance cost, fuel consumption, and emissions.

The diesel engine forklifts can be operated continuously for the long shifts while the electric forklifts have a limitation in those circumstances because the batteries take substantial recharging time after depletion of charge decreasing the productivity. On the other hand, the carbon emissions of ICE forklifts exceed by 120,000 pounds than the electric forklifts for 10,000 hours of operation [3]. As the general construction machinery, forklifts are also projected to grow at a compound annual growth rate of 1.93% from USD

16.00 billion in 2016 to USD 17.61 billion by 2021 [4]. This will have significant impact on the fuel consumption and emissions.

Governmental institutions like Department of Energy (DOE), Environment Protection Agency (EPA), and California Air Resources Board (CARB) have imposed strict regulations for vehicle emission and fuel consumption which has forced OEMs to strive for improvement in engine efficiency and vehicle technology continually. Particulate matter(PM) emission for Euro Stage V emission standard is 97% lower while hydrocarbons and oxides of nitrogen (NOx) emission are 94% lower than Euro Stage I emission standard [5]. To meet these emission requirements, the diesel engine used for a heavy-duty application requires sophisticated after-treatment systems.

Electric forklifts have gained popularity recently in the market due to awareness of climate change caused by exhaust emissions, and an increase in fuel cost. Electric forklifts offer many advantages as zero-emission, maintenance and operation cost, and noise reduction. As with any machines, electric forklifts also have its drawbacks. Compared to conventional engine forklifts, electric forklifts have higher investment for an additional battery and charger. Moreover, these cannot be operated continuously for a longer duration and takes an extended period of time to be fully charged. Due to these drawbacks, manufacturers like Toyota, Mitsubishi, Komatsu, etc. are working to build a hybrid powertrain to address gap between the combustion engine and pure electric drivetrain.

1.2. Motivation

An optimum powertrain layout strongly depends on the application as well as specific duty cycles, but in general, an optimized hybrid system can give a definite advantage. In addition to this, there is also an interest to reduce tailpipe emissions or create a zero-emission solution. Further potential can be exploited by optimizing a given engine and the after-treatment system for the use in a hybrid system if the engine operating conditions can be

restricted to a small part or a single point of a characteristic operating curve. Besides, this is a cost-effective approach, as manufacturers may have an engine from a standard application, which can be optimized for the use instead of designing an engine from scratch.

Furthermore, the hybrid powertrain provides the following advantages:

- Downsizing of engine and after-treatment systems
- Fuel saving as the engine is running at optimum BSFC
- Reduction of emission and noise
- The heavy batteries can be used to counter-balance the weight while lifting
- Further potential for the electrically operated auxiliary unit

Moreover, there is potential for better fuel consumption and oxides of Nitrogen (NOx) emission reduction if an engine is running at a constant point in series hybrid architect for forklift applications, particularly in a Verband Deutscher Ingenieure (VDI) 2198 cycle [6]. VDI 2198 is a standardized drive cycle for the forklift to measure performance and fuel consumption followed by manufacturers. The operating point of engine for 55 kW diesel engine in VDI 2198 cycle is shown in Figure 1.1. It can be noticed that the engine is mostly operating at the lower loads, which might affect the performance of after-treatment components.

Selective Catalytic Reduction (SCR) catalyst would require a longer time to reach a light-off temperature in a conventional diesel engine for a VDI cycle. NOx conversion starts only after reaching the light-off temperature, where diesel exhaust fluid (DEF) dosing is initiated. So, a series hybrid architect with the engine running slightly higher load would provide overall NOx emission benefits as the catalyst attains light off temperature faster and the surplus energy will be utilized to charge the battery during operation [7].

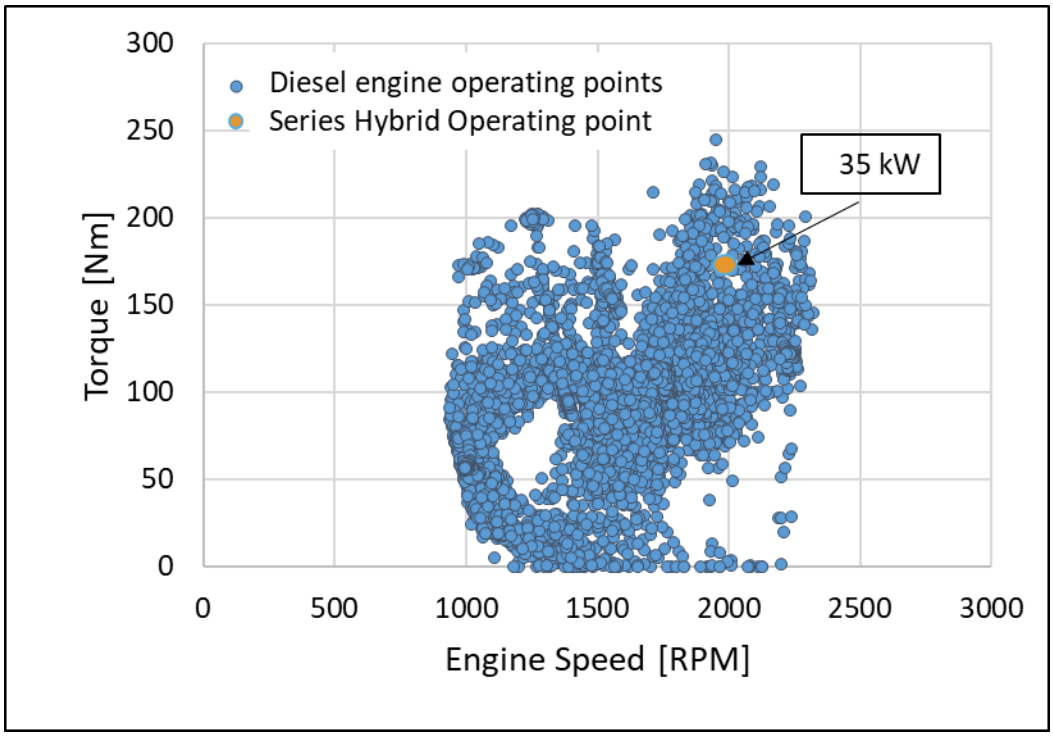

Figure 1.1: Engine operating points for 55 kW engine used in the diesel forklift during a VDI 2198 cycle – Data is provided by IAV GmbH

Furthermore, the diesel engine forklifts must be equipped with Diesel Particulate Filter (DPF) to meet new emission standards. As forklifts cycle are low load cycle with short peak loads, soot accumulation increases with the operation of the vehicle due to the limited soot regeneration process inside the DPF. Therefore, the accumulated soot in the DPF must be burned with the active regeneration process after certain hours of operation. This process is lengthy and requires running of an engine at full RPM about 20 to 30 minutes consuming a large amount of fuel and the productivity is also reduced as the lift trucks are not available for use [8]. A series hybrid diesel engine forklifts running at slightly higher load, however, can provide maximum benefits in this condition. The soot accumulated in the DPF goes through constant passive regeneration as the engine at a slightly higher load operating point. The engine operating at higher load decreases the frequent necessity of active soot regeneration process as soot is continuously retaining via the passive regeneration process.

Besides, better fuel consumption and NOx emission can be achieved if that single point is optimized with the performance of the particular engine and after-treatment components in detail and sizing of the hybrid powertrain component with an adequate control strategy. Therefore, the optimization of an engine at a single operating point considering the performance of the after-treatment components are investigated in this study which is aimed for use in a series hybrid forklift application.

1.3. Objective

The main objective of this thesis is to model engine, after-treatment and powertrain components for a hybrid forklift in 1-D simulation environment that would capture thermodynamic engine model, the reaction mechanism of after-treatment systems and powertrain architecture including control strategy of vehicle operation. Therefore, a GT-Suite® holistic modeling approach with the coupled engine and after treatment model is used to establish a model-based hardware definition and calibration optimization approach for the engine and after-treatment system of a defined off-highway application. Existing model in GT-Suite® library will be utilized to develop an initial engine model, and it will be validated against the experimentally verified engine model developed by IAV GmbH.

The engine is then optimized for a single operating point to achieve best fuel efficiency, which is coupled with after-treatment components. The optimal point for engine will be selected with DOE analysis and optimizer present in GT-Suite® application. The after-treatment model best suited for the specified application will be chosen from the GT Power library. The length of DOC, DPF, and SCR catalyst will be selected to meet the future emission requirement of a non-road diesel engine. The key powertrain components as electric motor and battery will be designed based on the existing literature, and other parts will be chosen to meet vehicle performance based on engineering judgments.

After modeling of the entire component, a control strategy for hybrid powertrain will be defined, which determines operating modes of the vehicle and vehicle overall analysis will be carried out. Cost benefits of the after-treatment components, energy utilization for vehicle drag and rolling resistance, and energy recuperation during regenerative braking in VDI cycle will also be evaluated. Along with that, vehicle performance will be compared with conventional diesel forklift based on the data provided in the manufacturer specification sheet.

1.4. Scope of Research

GT-Suite® has several pre-defined libraries that allow the building of sub-models to represent the engine, after-treatment, and vehicle model. These models can accurately predict combustion and emission formation as well as powertrain performance. So, entire study has been carried out in the GT-Suite® simulation environment. The baseline model is developed in GT-Suite® employing sub-models of the engine used for similar application provided by IAV GmbH. Furthermore, inbuilt sub-models are also implemented to predict the engine performance and emissions. For this study, the operating point for the engine is assumed as 2000 RPM with a 35kW load referencing to the engine operating points of the VDI cycle in Figure 1.1. In addition, the operating point will limit the continuous engine operation below 80% of the peak load suitable for the diesel series hybrid forklift application [9].

Parameters such as air-fuel ratio, boost pressure, injection timing, injection pressure, and compression ratio are studied to optimize engine performance and emissions. However, potential fuel benefits of using advanced technology like variable valve timing, cylinder deactivation, miller timing are not covered in this study.

The GT-Suite® library comprises a well-defined after-treatment model for DOC, DPF, and SCR validated with the experimental data from peer-reviewed references. So, the model

suitable for this study is chosen to represent after-treatment components. It is assumed that reaction kinetics is not altered by changing catalyst length for those models, so catalyst lengths are the only parameter that is optimized to meet emission requirement. In this thesis, ammonia is directly injected upstream of the SCR inlet to utilize the provided model in GT-Suite® without any modifications. However, in a real application, urea solution injected undergoes thermal decomposition and hydrolysis reaction to form ammonia, which isn't 100% efficient.

Cold-start emission is also investigated, but engine idling is not considered for this study. The ambient temperature and catalyst temperature is 25^0 C at the beginning of the cycle for this study, and engine simulation is performed without considering an idle operation. The temperature would increase slightly during engine operation at idling, which is not considered due to the limitation of available data for idling.

A series hybrid forklift with an engine operating at a single point can reduce tail-pipe NOx emission by attaining SCR catalyst light-off temperature faster, decreases the frequency of active regeneration process. So, a series hybrid forklift architect is developed by modeling key components such as traction motor, battery, generator with control strategies adequate for VDI cycle, and other parts are chosen based on engineering judgment that is suitable of the current application. The hydraulics lifting components are not designed in this study. So, data available in the reference [10] for 5000 kg load forklift is used to represent power consumption by hydraulic components during VDI 2198 cycle. Finally, performance and cost analysis are evaluated to compare the results of an optimized hybrid electric forklift with those from a conventional forklift that runs with a fuel-efficient diesel engine.

Chapter 2: Literature Review

2.1. Introduction

Numerous research studies have been carried out for hybrid forklifts. The combination of two or more energy sources like a battery, fuel cell, capacitors, and the internal combustion engine is used for hybrid forklift application. In the hybrid battery-capacitor forklifts, the battery is used as the main source of energy while super-capacitors are only utilized during higher power demand. Super-capacitors are used in conjunction with the batteries that can enhance the battery duration and maintain higher efficiency due to the reduced battery operating load[11].The fuel cell with battery and a relatively small ultracapacitor can significantly reduce the load variations are shown in another research article [12]. Optimization of fuel cell and battery size can also provide up to 24% benefit on hydrogen consumption [13] Therefore, the performance simulation and analysis of the fuel cell and the battery is carried out by parametric study in the reference [13] for optimal sizing of these components.

Diesel hybrid forklifts are also studied with different configurations for load handling and traction to reduce the consumption of fossil fuels. Fuel consumption of the diesel engine can be reduced almost by 39 % using a diesel hybrid in a VDI cycle, which is shown in the references [10]. The benefits of combining the different energy sources are realized in the earlier forklift research studies. There are some studies that are focused on the development of forklifts with hybrid energy sources and sophisticated control strategies to further reduce the energy consumption from its application but there is a gap, which is addressed in this thesis.

This study is focused on the reduction of fossil fuel consumption as well as minimizing the tailpipe emissions from the engine for the forklift application. So, engine performance and emission, after-treatment and the hybrid powertrain components are studied to optimize a

single point operating diesel engine for a series hybrid forklift application. In the following section, diesel engine performance, after-treatment system, emission standards for the non-road engine, and hybrid electric powertrain components are reviewed to develop a realistic diesel series hybrid forklift model in GT-Suite® simulation environment.

2.2. Diesel Engine

Diesel engines offer better fuel economy advantages over gasoline spark-ignition engines but engine out emissions as soot and NOx are significantly high due to complex diffusion combustion phenomenon occurring inside the cylinder. Parameters that effect the diesel engine combustions and emissions are discussed in this chapter, along with some of the advanced technologies to optimize fuel efficiency and emission.

2.2.1. Engine Operating Parameters

Diesel engine performance and emission are mainly affected by fuel injection strategy (Injection timing, injection pressure, and injection profiles), compression ratio, boost, EGR, engine speed, and load. Engine performance and emission of diesel engine are assessed by brake specific fuel consumption and brake specific emissions for soot, NOx, and hydrocarbons.

2.2.1.1. Injection Strategy

In a conventional diesel engine, fuel is injected directly into the combustion chamber using high pressure (700-2000 bar) injectors [14]. Injectors consist of a multi-hole nozzle which atomizes the fuel, making fuel particles finer and promote mixing of fuel and air for combustion inside the cylinder. Combustion in a diesel engine is sensitive to injection strategy and influenced by several factors.

2.2.1.1.1. Injection Pressure

Fuel must be injected at extremely high pressure into the combustion chamber for proper combustion with air charge mixture. The magnitude of injection pressure affects fuel consumption and exhaust emission. When injection pressure is high, in-cylinder pressure increases as fuel travels at high speed, making the area of pre-mixing faster. As a result, combustion duration becomes short, and most of the energy is released at the initial phase of combustion. Fuel is burned rapidly, resulting in very high pressure and temperature, a condition favorable for NOx formation. NOx formation also increases due to the increase in the peak cylinder temperature since the combustion is advanced [15]. However, fuel efficiency is increased, and soot formation is reduced due to the above-mentioned phenomenon for the high magnitude of injection pressure [16].

On the order hand, with a low magnitude of injection pressure, fuel is not atomized sufficiently to the finer particle leading to longer combustion duration and makes it difficult for fuel to penetrate the air-fuel mixture. This increases the formation of soot and fuel consumption while NOx emission is comparatively low as in-cylinder temperature and pressure don't reach favorable conditions for NOx formation. Modern diesel engines are equipped with an optimized fuel injection system that improves combustion efficiency and minimizes soot emission.

2.2.1.1.2. Injection Timing

Injection timing also plays a vital role in the combustion of the fuel-air mixture in a diesel engine. Injection timing can be retarded or advanced relative to the baseline start of injection timing to improve engine performance. Advancing of injection timing is an injection of fuel before the baseline timing while retarding means later injection than baseline. At the end of the compression stroke, air-charge is highly compressed, resulting in very high temperature and pressure. Fuel, when injected in those instances, burns

instantaneously releasing a high amount of energy, and the combustion is heterogeneous and takes place at constant pressure [17].

NOx reduction can be reduced retarding injection timing, but fuel consumption and PM emission must be compromised. Retarding injection timing can be used in conjunction with high injection pressure, higher compression ratio, and higher boost pressure to reduce fuel economy penalty [18]. Injection timing has a significant effect on the diesel engine equipped with the after-treatment system. Retarding injection timing form the main start of injection and late fuel injection increases Exhaust Gas Temperature (EGT) downstream of DOC as unburned fuel in the combustion chamber are oxidized at DOC. This promotes soot regeneration in DPF. However, excessive retarding of injection timing leads to engine oil dilution as fuel impinges on the cylinder wall and washes down due to piston movement [19]. Fuel seeping from the cylinder-wall could lead to the degradation of engine oil and increases engine wear that eventually decreases engine performance in the long run.

Fuel injection pressure, rate, and timing can be optimized to reduce the trade-off between oxides of Nitrogen (NOx) and Particulate Matter (PM) emissions [20]. A modern diesel engine uses electronic unit injector than can precisely control injection and employ multiple injections per cycle that can reduce noise, fuel consumption, and meet emission standards [15].

2.2.2. Exhaust Gas Recirculation

Exhaust Gas Recirculation (EGR) is the process of diverting a portion of exhaust gases into the intake manifold, using the pressure difference between the exhaust manifold and downstream of the compressor. EGR reduces NOx emission as a result of lower oxygen concentration in the air-fuel mixture. This reduction of O_2 concentration results in the drop in-cylinder combustion temperature and slows down the combustion rate mainly due to the higher heat capacity of exhaust gas than air [21].

EGR cooler must be used upstream of the EGR valve to cool down exhaust gas going into the intake manifold, which would further increase heat absorption in the combustion chamber and enhance NOx reduction [22]. EGR could be varied from 0% to 40% in the modern engine, which facilitates a reduction in NOx emission [20]. The NOx emission benefit of EGR, however, has a negative impact on fuel consumption, hydrocarbon, and soot emission, which must be addressed. So, EGR should be used along with increased fuel injection pressure, highly efficient DOC, and a higher boost for better NOx reduction with least impact on fuel efficiency and other emissions.

2.2.3. Turbocharger and Boost

The higher mass flow of air into an engine cylinder can be achieved by using turbocharger or supercharger. Diesel engines commonly use turbocharger that consists of a turbine driven by the exhaust gas flow and connected to the compressor through a shaft enclosed in a housing. Turbocharger assists in drawing atmospheric air and increases the air pressure and density entering the cylinder. Intercooler is used with a turbocharger to increase the density of boosted air furthermore and reduce the temperature that helps in NOx reduction [23]. Increasing boost pressure provides enough room for retarding injection timing to minimize NOx emission without compromising fuel efficiency and power [24]. The ignition delay period is short due to higher air charge density, which reduces the fraction of fuel burned during premixed combustion and results in lower NOx emissions [23].

Turbocharger performance is determined by operating characteristic curve of the turbine, and it depends on mass flow rate, efficiency, and pressure ratio at different operating speeds. Generally, two kind of turbines, fixed geometry, and variable geometry turbine are used for turbocharger application. Fixed geometry turbine has poor performance at low engine speed, but variable geometry turbine can perform well at low speeds too as a movable vane inside it provides flexibility over the pressure ratio/flow relationship [25].

This mitigates the predominantly noticeable turbocharger lags as well as improves low-speed torque characteristics [25].

The turbocharger in a forklift helps to provide higher power with better fuel economy and downsizing of the engine. A compact turbocharger with an electronically controlled variable nozzle is also used by some forklift manufacturers to deliver high torque even at low speeds [26].

2.2.4. Compression Ratio

The compression ratio (CR) of an engine is the ratio of the total volume of the combustion chamber when the piston is at the bottom dead center to the clearance volume. Diesel engines can operate at a higher CR compared to gasoline engines whose CR is limited by the engine knock. Increasing CR increases in-cylinder pressure and temperature that facilitates combustion and improves fuel consumption, but on the other hand, it increases NOx emission. However, exhaust gas temperature (EGT) also decreases when the CR is increased because of the complete combustion of fuel resulting in lower losses from cylinder [27]. This affects the conversion efficiency of after-treatment components, especially during cold start. Also, the CR of an engine is limited by the maximum in-cylinder pressure and temperature of an engine as well as EGT.

2.2.5. Engine Speed and Load

The diesel engine forklift operates between 800 RPM to 2200 RPM in VDI 2198 cycles as it is a low load cycle and the engine operating point for the cycle is mostly below 35 kW as seen in Figure 1.1. The engine speeds and load are also determining factors that affect fuel efficiency and emissions. Therefore, the optimum engine operating point selection can provide significant fuel consumption and emission benefits. The fuel consumption increases with increasing the engine speed due to the addition of frictional losses and

pumping losses [28]. Besides, the flame speed of diesel is limited, resulting in incomplete combustion during higher engine speed worsening fuel consumption [29]. The engine must not be operating at higher speeds for optimum fuel efficiency while operating at a fixed point. On the other hand, the engine operation at the higher loads also requires more amount of fuel injection into the combustion chamber, leading to a higher temperature and NOx emission [30].

The engine performances are determined by other parameters too, but for this thesis, it is limited to the five aforementioned parameters.

2.3. Emission Standards

Emission standards for off-road as well as on-road diesel engines are getting stricter. EPA and EU emission standard pertaining to a non-road diesel engine has defined engine emission restriction on CO, NMHC, NOx, and PM. The emission standards of engine depend on engine power category that is listed in Table 2.1 and Table 2.2. The engine above 56 kW requires substantial NOx reduction to meet emission standards. With the introduction of Stage V Euro emission standard Particle Number (PN) emitted must be limited to $1*10^{12}$/kW-hr to ensure highly efficient PM control technology. Euro emission standard and EPA emission standard are almost similar with all exhaust emission species, which can be realized from Table 2.1 [5].

With specific application categories, emissions for the non-road engine is measured based on steady-state cycle defined in the international standard for exhaust emission measurement ISO 8178 test cycles[31]. The weighting factor is used for different engine loads at rated speed and intermediate speed to determine weighted average emission of different operating point in ISO 8178 test cycles. With the introduction of Tier 4/Stage V of new emission standard by EPA and EU respectively, the non-road engine should also meet the non-road transient cycle along with the steady-state test. The transient cycle

accounts both cold start (5%) and hot start emission (95%) to evaluate overall emission. The transient testing, however, does not apply to any power capacity engine operating at a constant speed [32].

Table 2.1: Stage V emission standards for the non-road engine-adapted from reference [5]

Category	Ign.	Net Power	Date	CO	HC	NOx	PM	PN
		kW		*g/kWh*				*1/kWh*
NRE-v/c-1	CI	P < 8	2019	8.00	7.50[a,c]		0.40[b]	-
NRE-v/c-2	CI	8 ≤ P < 19	2019	6.60	7.50[a,c]		0.40	-
NRE-v/c-3	CI	19 ≤ P < 37	2019	5.00	4.70[a,c]		0.015	1×10^{12}
NRE-v/c-4	CI	37 ≤ P < 56	2019	5.00	4.70[a,c]		0.015	1×10^{12}
NRE-v/c-5	All	56 ≤ P < 130	2020	5.00	0.19[c]	0.40	0.015	1×10^{12}
NRE-v/c-6	All	130 ≤ P ≤ 560	2019	3.50	0.19[c]	0.40	0.015	1×10^{12}
NRE-v/c-7	All	P > 560	2019	3.50	0.19[d]	3.50	0.045	-

[a] HC+NOx
[b] 0.60 for hand-startable, air-cooled direct injection engines
[c] A = 1.10 for gas engines
[d] A = 6.00 for gas engines

Table 2.2: Tier 4 US emission standards for the non-road engine - adapted from reference [32]

Engine Power	Year	CO	NMHC	NMHC+NO_x	NO_x	PM
kW < 8 (hp < 11)	2008	8.0 (6.0)	-	7.5 (5.6)	-	0.4[a] (0.3)
8 ≤ kW < 19 (11 ≤ hp < 25)	2008	6.6 (4.9)	-	7.5 (5.6)	-	0.4 (0.3)
19 ≤ kW < 37 (25 ≤ hp < 50)	2008	5.5 (4.1)	-	7.5 (5.6)	-	0.3 (0.22)
	2013	5.5 (4.1)	-	4.7 (3.5)	-	0.03 (0.022)
37 ≤ kW < 56 (50 ≤ hp < 75)	2008	5.0 (3.7)	-	4.7 (3.5)	-	0.3[b] (0.22)
	2013	5.0 (3.7)	-	4.7 (3.5)	-	0.03 (0.022)
56 ≤ kW < 130 (75 ≤ hp < 175)	2012-2014[c]	5.0 (3.7)	0.19 (0.14)	-	0.40 (0.30)	0.02 (0.015)
130 ≤ kW ≤ 560 (175 ≤ hp ≤ 750)	2011-2014[d]	3.5 (2.6)	0.19 (0.14)	-	0.40 (0.30)	0.02 (0.015)

a - hand-startable, air-cooled, DI engines may be certified to Tier 2 standards through 2009 and to an optional PM standard of 0.6 g/kWh starting in 2010
b - 0.4 g/kWh (Tier 2) if manufacturer complies with the 0.03 g/kWh standard from 2012
c - PM/CO: full compliance from 2012; NOx/HC: Option 1 (if banked Tier 2 credits used)—50% engines must comply in 2012-2013; Option 2 (if no Tier 2 credits claimed)—25% engines must comply in 2012-2014, with full compliance from 2014.12.31
d - PM/CO: full compliance from 2011; NOx/HC: 50% engines must comply in 2011-2013

2.4. After-treatment Systems

Concerns on climate change and global warming have led the environmental protection agency all over the world to impose strict emission regulations for diesel engines. It is hard to meet the target emission level for a diesel engine without a well-equipped after-treatment system. After-treatment components like Diesel Oxidation Catalyst (DOC), Diesel Particulate Filter (DPF), and Selective Catalytic Reduction (SCR) that aid in reducing the tail-pipe emission releasing into the environment are briefly explained in the following section. The after-treatment components layout is shown in Figure 2.1. It comprises DOC at the beginning, which oxidizes unburned hydrocarbon and carbon monoxide emitting from the engine. DPF is located next to the DOC that captures soot and particulate matter in the wall and filter. SCR is placed just before the tailpipe end, which reduces NOx in the catalyst with the aid of NH_3 obtained from DEF fluid.

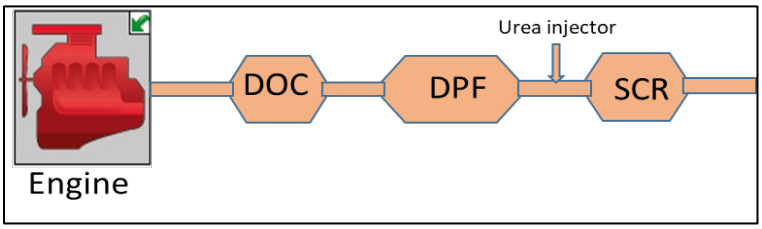

Figure 2.1: After-treatment components layout

The conversion efficiency of NOx in the SCR catalyst is calculated using the Equation (2-1), which is determined by the mass flow rate of NOx at upstream and downstream of the SCR.

$$\eta_{NO_x} = (\dot{m}_{NO_x,in} - \dot{m}_{NO_x,out})/\dot{m}_{NO_x,in} \quad (2\text{-}1)$$

where,

η_{NO_x} is the conversion efficiency of NO_x

$\dot{m}_{NO_x,in}$ is inlet mass flow rate of NO_x for catalyst

$\dot{m}_{NO_x,out}$ is outlet mass flow rate of NO_x for catalyst

In a similar manner, the conversion efficiency of HC, CO and NO are determined for DOC, and soot accumulation in the filter, PN are determined for DPF

2.4.1. Diesel Oxidation Catalyst (DOC)

DOC is used in diesel engine forklift to meet Tier 4/Euro V emission standards. DOC systems are simple, small, have an extended life, and requires less maintenance compared to DPF. The primary function of DOC is to oxidize hydrocarbon and carbon monoxide into carbon dioxide and water in the presence of a catalyst. The catalyst materials commonly used in DOC are expensive platinum and palladium [33]. So, the catalyst coating is applied to honeycomb metallic or ceramic substrates. DOC also oxidizes NO to NO_2 which plays a vital role in the performance of DPF and SCR located downstream of DOC. NO_2 conversion in DOC occurs after hydrocarbon conversion efficiency reaches around 80%, which can be seen in Figure 2.2.

As NO_2 is more reactive than oxygen, higher NO_2 concentration in NOx increases the efficiency of DPF by promoting soot oxidation in DPF, and overall NOx conversion in SCR as equimolar 1:1 NO_2/NO and NH_3 reaction are considered the fastest reaction in SCR [34]. DOC is effective only after reaching catalyst light-off temperature defined as the temperature at which catalyst actively start oxidizing CO and HC. DOC efficiency depends on exhaust gas composition, space velocity, type of catalyst, and volume of catalyst used illustrated in the reference [35]. The reactions occurring inside the DOC are exothermic. This leads to heat release and increasing enthalpy of the exhaust gas downstream of DOC [36].

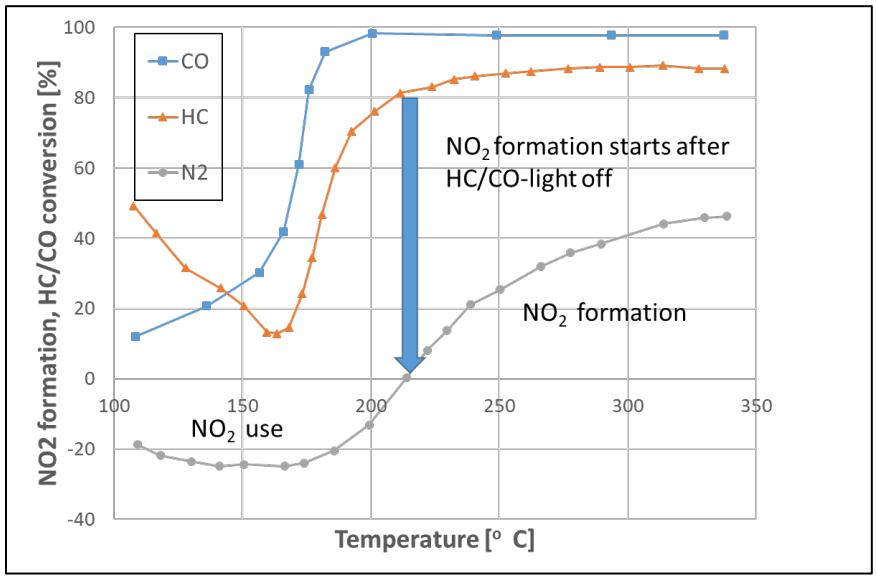

Figure 2.2: HC, CO and N_2 conversion as a function of EGT at DOC- adapted from reference [13]

2.4.2. Diesel Particulate Filter (DPF)

The diesel engine produces soot and other small diesel particles commonly known as particulate matter (PM) due to incomplete combustion of fuel-air charge inside the combustion chamber. New Euro V emission standard has imposed limit not only on PM but also on a number of particles emit to $1*10^{12}$/kW-hr [37]. This limitation has led to the implementation of DPF for every diesel engine forklifts to meet emission standards. DPF captures unburned soot and small diesel PM in the filter, minimizing emissions of those harmful components to the environment [38].

The typical particulate filter is either made of metal or ceramic. A ceramic filter Cordierite is a popular choice which is coated with the precious group metal (PGM). The catalyst substrate has a porous wall which captures small PM on it and the clean air exits through the outlet of the particulate filter.

Deposition of PM on substrate layer forms a PM cake layer. This PM cake layer also contributes filtration of PM flowing along with the exhaust gas, which is the reason for higher filtration efficiency (>95%) of DPF in most operating conditions [39]. The deposited PM in a DPF is oxidized either by oxygen or by nitrogen dioxide. NO_2 assisted oxidation is possible due to the catalytic coating on DPF. The amount of soot particle captured go on continuous passive regeneration at a lower temperature as NO_2 significantly reduce the light-off critical temperature of soot particles [40].

As soot accumulation inside the DPF increases, the pressure drop across DPF rises, which reduces the efficiency of an engine as a result of high back-pressure. So, in such circumstances, DPF active regeneration is required to burn soot accumulated. It can be accomplished by injection of the extra amount of fuel either in exhaust stroke or via late post-injection which burns at DOC raising exhaust gas temperature sufficiently higher to burn soot accumulation in DPF. For these purposes, additional combustion modes are defined in the advanced commercial diesel engine for exhaust temperature management to ensure completion of active DPF regeneration [41]. The active soot regeneration is a lengthy process, and it must be performed once or twice a week as forklifts run mostly in a low load cycle. So, the engine must be idled at full rpm until the regeneration is complete [8]. This results in additional fuel consumption, as well as trucks, are not available for use. Moreover, high load and lots of idling time increase the frequency of regeneration cycle [42]. And, skipping the active regeneration cycle might increase replacement frequency of DPF as it damages DPF permanently.

2.4.3. Selective Catalytic Reduction (SCR)

Selective Catalytic Reduction (SCR) of NOx is one of the widely used technologies in heavy-duty diesel engines to meet the current stringent emission standard imposed by worldwide emission legislations. NOx is reduced to harmless nitrogen (N_2) using a reducing agent as ammonia (NH_3) or urea solution in the presence of catalysts as Cu-

Chabazite, Fe-Zeolites, and vanadia-titania [43]. Each catalyst has its specific advantages and disadvantages. Cu-Chabazite catalysts have better conversion efficiency at a lower temperature (250^0 C -350^0 C) while the conversion efficiency of Fe-zeolites is superior at a temperature higher than 400^0 C [44]. The characteristic of those two catalysts is extensively studied using Global kinetic models in reference [44] to predict the prominent feature of SCR reactions.

NOx conversion mechanism is complicated and depends on many factors such as operating temperature range, catalyst volume, composition of different gases feed into the catalyst (1:1 ratio of NO_2 and NO results in higher conversion efficiency for Fe-zeolite catalyst [34]), exhaust mass flow rate, urea dosing strategy and presence of ammonia in the active catalyst site which is elaborated in the reference [45]. Along with that combination of Cu-Chabazite and Fe-Zeolite catalyst in the different arrangement has also an impact on the conversion efficiency of NOx at different temperatures as presented in the reference [44]. The result shows that a combination of those two catalysts offers better conversion efficiency for a wide range of temperatures.

SCR in the commercial diesel engine is more expensive after-treatment component than DPF and DOC [14] as it needs additional urea dosing component for the conversion of NOx. That includes urea tank, injector, an actuated membrane pump, piping link, urea dosing control for efficient conversion and NH_3 slip mechanism. Extensive studies have been carried out in [34, 46] for urea dosing strategy as controlling ammonia storage in ammonia poses many challenges and ammonia adsorbed in the catalyst cannot be directly measured. Closed-loop control can be implemented to improve performance, but it still has some limitations due to the urea injection system, SCR catalyst dynamics and NH_3 slip management and oxidation of NH_3 on catalyst surface at higher temperature [47].

2.5. Hybrid Electric Powertrain System

There are different powertrain layouts, but they can be broadly classified into Series, Parallel, or Series-Parallel Hybrid. The main differences between series hybrid and parallel hybrid are only electric motor propels the vehicle in series architecture while the engine and electric motor are mechanically coupled to the transmission which drives the vehicle in a parallel architecture. Series-parallel architect, introduced first by Toyota, uses a power-split device to blend series and parallel transmission path, providing better operational efficiency. All these architects have advantages and limitations, and the choice of powertrain architect depends on their application.

The application of forklift offers better advantage utilizing hybrid powertrain system due to vehicle dynamic operating patterns and regenerative opportunity during the work cycle, presented in the references [10, 48]. Hybrid forklift configuration in reference [10] uses a series hybrid configuration for traction motor and parallel hybrid configuration for the hydraulic power system, is shown in Figure 2.3 and Figure 2.4, respectively. The hybrid architect presented could improve fuel efficiency by 35% compared to the conventional diesel engine forklift. The reason for the improvement of fuel efficiency was downsizing of the engine, highly efficient driving traction motor for low speed and high torque condition, and regeneration during braking.

Another study of hybrid forklift truck uses series-parallel configuration for traction and parallel configuration for load handling that could provide a 39% reduction in fuel consumption [9]. These studies have shown hybridization of forklift can significantly reduce fuel consumption.

To implement a hybrid-electric powertrain for forklift application, energy storage system, engine, generator, power controller, electric motor, vehicle model, and vehicle controller strategy are required. These components are described in the following sections:

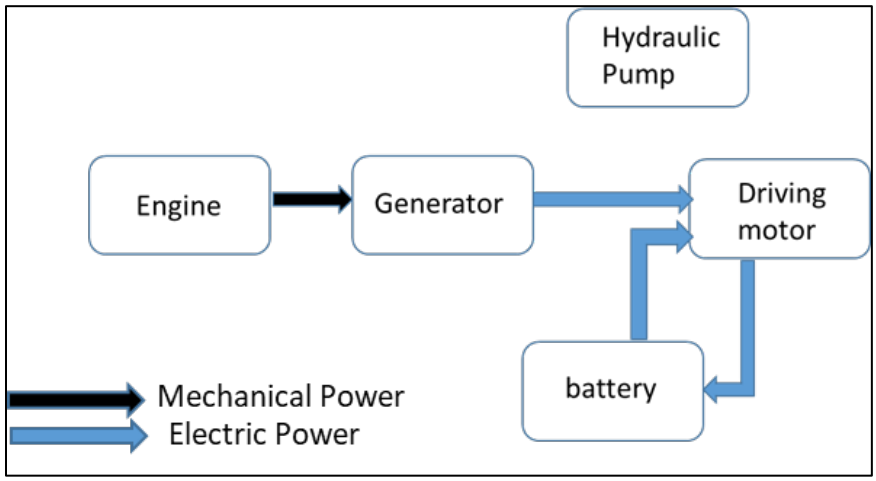

Figure 2.3: Parallel hybrid architect for forklift (Driving) [10]

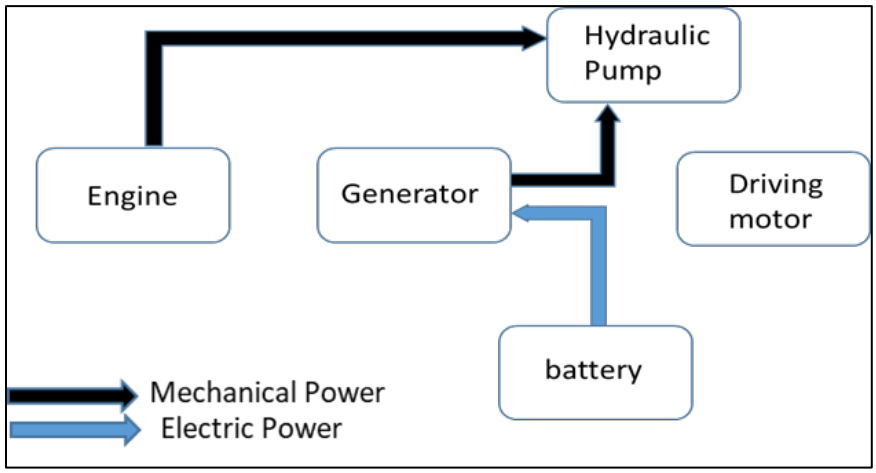

Figure 2.4: Parallel-Series hybrid forklift (Load handling) [10]

2.5.1. Energy Storage System

Energy is generally stored in a battery, ultracapacitor, and flywheel for a hybrid electric powertrain. Energy storage sizing is critical, which determines vehicle performance, fuel efficiency, and emission of the hybrid vehicle [49].

The battery serves as an energy storage system converting chemical energy into electrical energy on the requirement. Generally, the battery is combined in series and parallel to meet the required voltage and capacity demand, respectively. Adding the cells in series increases the voltages while adding the cells in parallel will increase the capacity of the battery. The battery is designed either for high power density or high energy density depending on performance requirements [49]. Figure 2.5 shows different kinds of batteries, depending on the materials used in the battery, and each battery has a specific performance. Lithium-based batteries like lithium-ion and lithium-polymer have high volumetric and energy density. While lead-acid has very low energy density and nickel-based battery as nickel-cadmium and nickel hydrides lying in between two. Lead-acid batteries are heavier, and they are intended to use for short-term use while the other two are the lightweight that could be used for intermediate or long- term [50]. Li-ion battery has gained a lot of attention recently due to better specific energy density and power density with more than 80% charge/discharge efficiency. The prices of these Li-ion batteries are also getting cheaper due to recent technological development [51], influencing many OEM including Hyundai, Ford, Renault, Tesla, Volkswagen, Nissan, Toyota to use Li-ion batteries in new vehicles.

Electric-powered forklifts require higher investment as they need larger capacity batteries along with a charger and an additional battery. In addition to that batteries must be charged after depletion of energy, which is a long and complex process. However, in hybrid electric powertrain, smaller capacity batteries can be used, which is charged through engine power. Li-ion batteries can provide a stable performance during fast charging and discharging, well-suited for hybrid application due to improvement in battery technologies [9]. So, Li-ion batteries are a popular choice in the market for present forklift application.

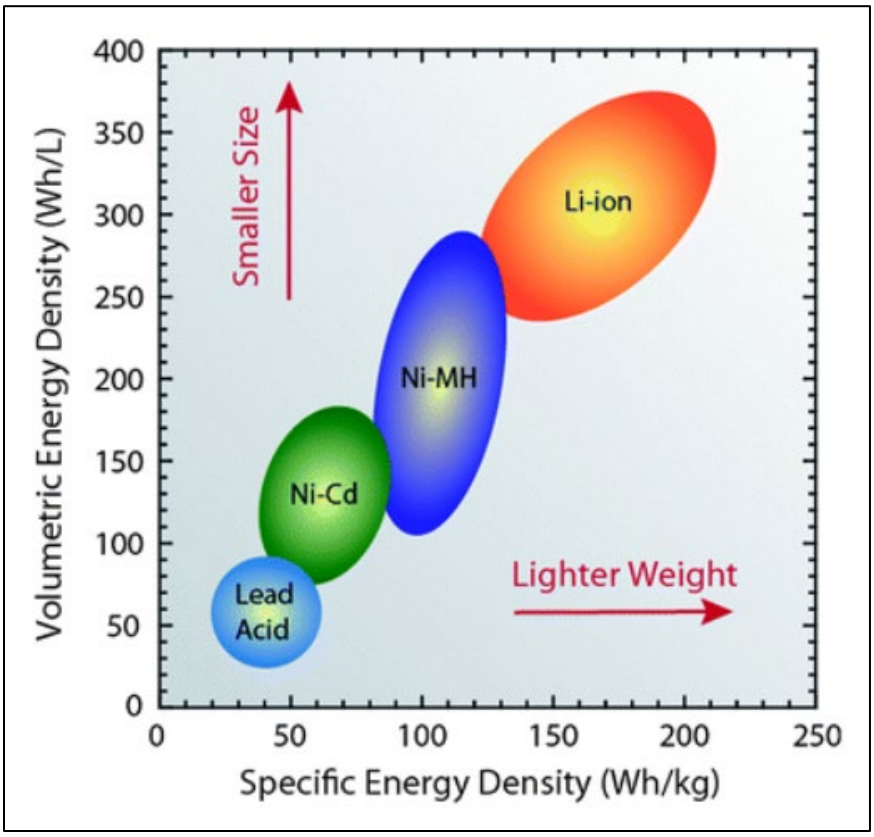

Figure 2.5: Energy density comparison of different battery type -adapted from reference [52]

Flywheel and ultracapacitor/supercapacitor are also used as an energy storage device, but they have very low energy density compared to the batteries. Ultracapacitor can be used especially for acceleration, high climbing, and during starting when high power is required. Combining ultracapacitor and battery can significantly reduce the size of the heavy battery, but rigorous research and development are needed to improve the performance and develop a better control strategy [53].

2.5.2. Electric Motor

An electric motor is connected to the drive components to provide traction power that converts electrical energy into mechanical energy. An electric motor is designed based on the power requirement, torque requirement, reliability, overload capability, controllability, and robustness at an affordable cost. An electric motor must be efficient at different operation torques and speeds, and suitable for regenerative braking. The electric motor is highly efficient compared to the combustion engine and can provide high torque at a lower speed, that can be seen in Figure 2.6. After attaining a base speed, constant power will be delivered by motor and power is reduced when the speeds are above critical speed. Motors are designed to run between 50% and 100% rated load, and the region with higher efficiency is near 75% of rated load [54]. The motor is designed with a service factor to prevent damage due to occasional overloading. Service factor is the indicator that gives a general idea about motor overloading capacity, and it must be noted that the efficiency of motor drastically drops if they operate continuously above rated load due to the heating of motor components impacting the durability period of motor [54].

Conventional electric forklifts use wound AC motors, but the current electric forklift manufacturers use permanent magnet DC motors or wound-field DC motors [55]. Permanent magnet DC motor uses strong permanent magnet while wound-field DC motor uses electromagnetic excitation to produce the motor's magnetic field. Permanent magnet DC motors are compact and operate efficiently for low speed- high torque condition with a better thermal characteristic, robustness, simplicity, high reliability, wide speed range, and low maintenance [56]. So, they are suitable for forklift traction motor which can be used for continuous duty application. Wound-field DC motors with a higher power rating and high stall torque can be used for steering and lifting pump drive application.

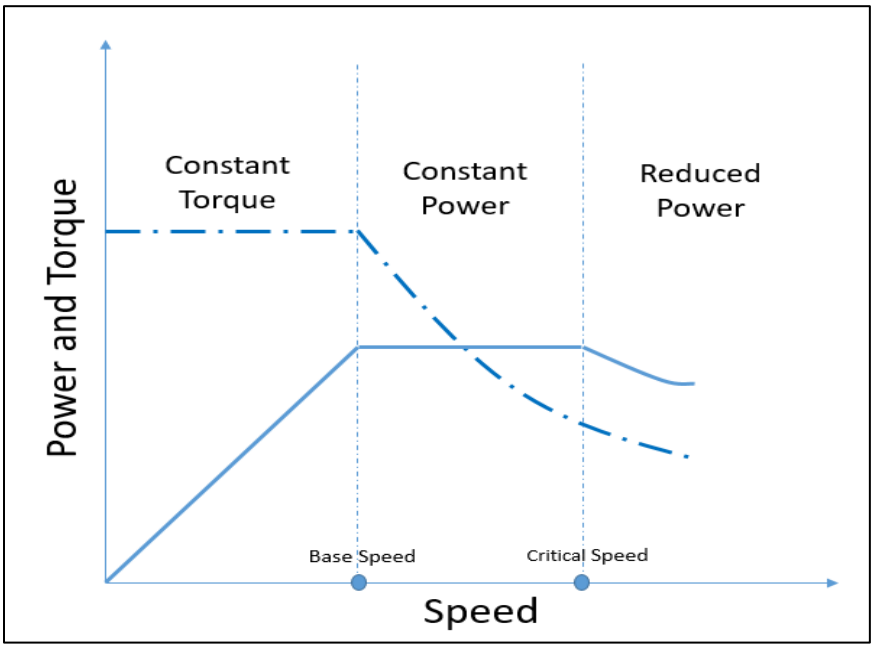

Figure 2.6: Standard torque-speed curve of an electric motor [57]

2.5.3. Power Electronic Converters

Power electronics is the core component of the hybrid and electric powertrain that converts electrical power from AC to DC, DC to AC as well as changes current and voltage level to the desired level. These conversions are required to operate the hybrid powertrain component effectively. Electric forklift uses DC electric motors for traction that usually needs a voltage control, DC-DC convertor using a buck/boost chopper circuit [58]. They are provided with a dedicated cooling system to prevent the component from being damaged because of excessive heating. Regenerative braking is possible due to the bidirectional nature of power electronics converter which allows recovering the energy during acceleration that would have been wasted if frictional braking were applied.

2.5.4. Supervisory Controller

Vehicle supervisory controller is the critical component of the modern hybrid electric powertrain that co-ordinates with an electrical power source, the internal combustion engine and transmission system to provide desired power, torque and speed commands for each wheel individually or simultaneously. It determines the regenerative braking and operating modes of the vehicle based on traction power demand and energy available in the battery. The operating modes must be defined properly to optimize the performance of the powertrain with the efficient utilization of available energy storage systems [59].

The supervisory control determines power splits between the electric and conventional engine power source, and provides engine start/stop command depending on power demand and SOC of the battery. It also estimates physical limitations of the components installed for drivability requirement and finally manages the dynamic coordination during transient maneuvers including different driving modes [59].

A supervisory controller can be classified into the heuristic controller, globally optimal controller, and locally optimal controller. Heuristic strategies are based on intuitive rules as ICE must be operated at optimum efficiency region, and battery SOC must lie within the maximum and minimum threshold range. A model-based integrated powertrain control that incorporates both energy and emission management for hybrid electric truck is developed in reference [60]. This model can optimize the cost of fuel consumption, urea consumption, and tail-pipe NOx emission. For, diesel hybrid forklifts accompanied by after-treatment components, temperature, and catalyst warm-up duration is also included in the strategy often known as rule-based approach.

The heuristic approach being an intuitive approach, several parameters must be tuned for setup and determining the priority of different components might lead to the poor performance of the entire system. On the other hand, the global optimal controller is non-

casual controller and solution of the system can be achieved with the knowledge of all operating characteristics during the entire time horizon [61]. For the local optimal controller, the result obtained from the optimization method as dynamic programming and model predictive control could be used. These controllers can generate a minimum energy consumption strategy for real-time implementation. Implementing a dynamic programming algorithm for optimal power management in a series hybrid off-road vehicle can provide around 7% to 9% better fuel economy than the rule-based approach [62]. The sophisticated control strategies could also be implemented in forklift for optimal power management as the forklift is often used for a repetitive task to provide maximum benefits.

2.5.5. Drive Cycle

VDI 2198 is a standardized drive cycle for the forklift to measure performance and fuel consumption followed by manufacturers. This drive cycle is an intensive cycle used for standard measurement. The sequence of actions carried out can be described with the help of Figure 2.7.

The starting position of the cycle is at point A in which the forklift is loaded with rated load. The vehicle moves in reverse until it reaches point C, then it moves about 30m forward to reach point B. At point B, the vehicle comes to rest where the rated load is lifted 2m high and again lowered back to the original height with the help of load handling devices. The driver returns to position A, where the lifting procedure is repeated._One complete VDI drive cycle takes 60 seconds. This cycle is used to evaluate fuel consumption forklifts. Since it is a very short cycle, variability can be brought up by operating time as well as acceleration and deceleration by the driver for each cycle. Therefore, the fuel consumption of forklift is calculated by repeating the VDI cycle for an hour, and the average fuel consumption is computed in liters per hour unit.

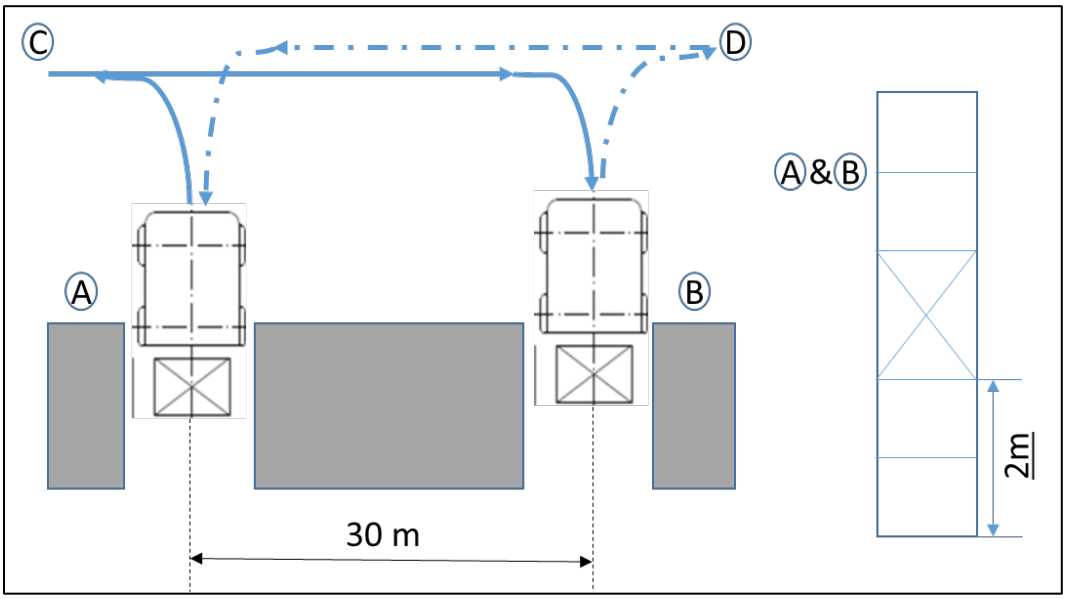

Figure 2.7: VDI 2198 drive cycle – Adapted from reference [63]

Chapter 3: Modeling of Engine, After-treatment and Powertrain Components

3.1. Introduction

The baseline model consists of an engine, exhaust after-treatment systems, and hybrid powertrain components including generator, power control module, battery, traction motor, hydraulic motor, vehicle model, and control systems. A series hybrid architect is selected for the powertrain modeling so that maximum benefits can be achieved from engine operating at the optimum operating point. The baseline model categorized into three subsystems for detail model setup in the GT-Suite® simulation environment is shown in Figure 3.1.

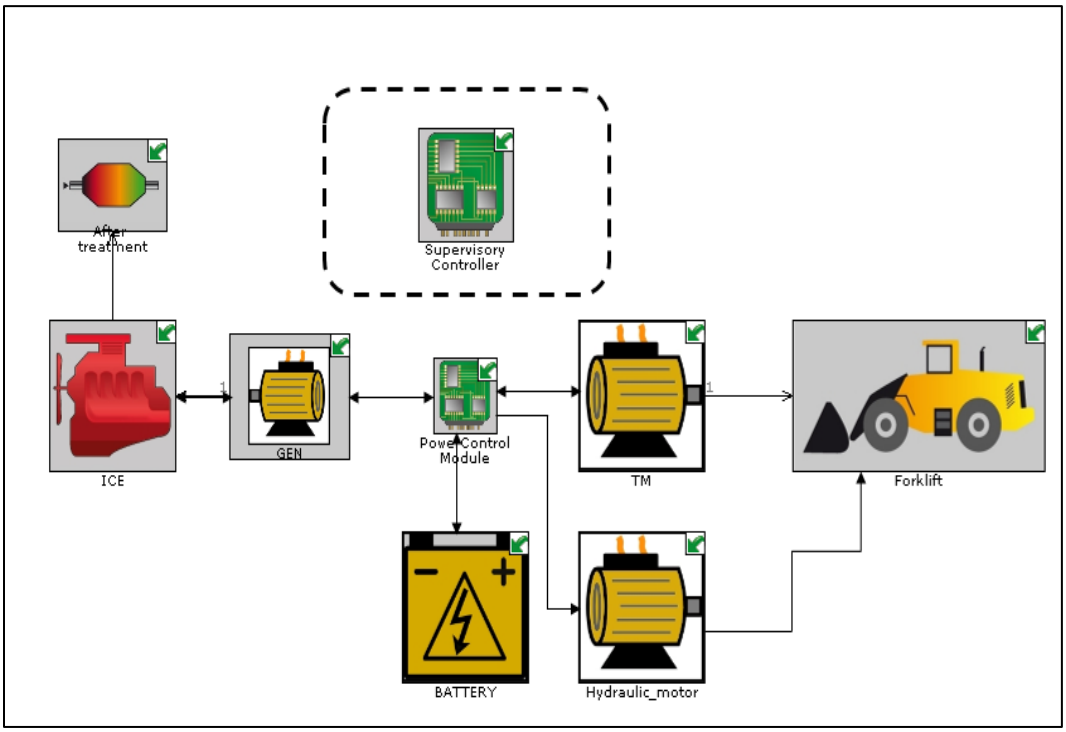

Figure 3.1: Baseline model for series hybrid forklift architect in GT-Suite®

3.2. Engine

The purpose of this thesis is to develop a generic diesel engine that can be optimized for best operating point to be used for series hybrid forklift applications. As modeling and validation of an engine component need lots of experimental data and is time-consuming, GT-Suite® example model was used for the starting model setup that comprehensively represents 1-D thermodynamic and combustion model. The starting model consists of the intercooler, VGT turbocharger, map-based injector, EGR cooler, fuel injection controller, throttle and EGR valve controller, and EGR controller. The model was calibrated to match the specification of engine data provided by IAV GmbH, which is used for forklift application. Necessary engineering judgments were taken to tune the model, so that engine performance emulates real engine behavior. Engine specifications used in the GT-Suite® model are listed in Table 3.1.

Table 3.1: Engine specification for the model

Displacement volume	2 L
Bore	86 mm
Stroke	86 mm
Number of cylinders	4
Compression ratio	17
Turbocharger	Fixed geometry turbocharger
EGR and Intercooler	Predictive EGR cooler
Fuel injection	DI with a smoke controller
Valves	4 (2 intakes and 2 exhaust) per cylinder
Connecting rod length	129 mm

Engine simulation environment in GT-Suite® is shown in Figure 3.2. Different sub-models are implemented to predict engine performance accurately. That sub-models are either experimentally verified model presented in GT-Suite® example model or provided by IAV

GmbH. The necessary sub-models and components that are required to build engine model are listed below.

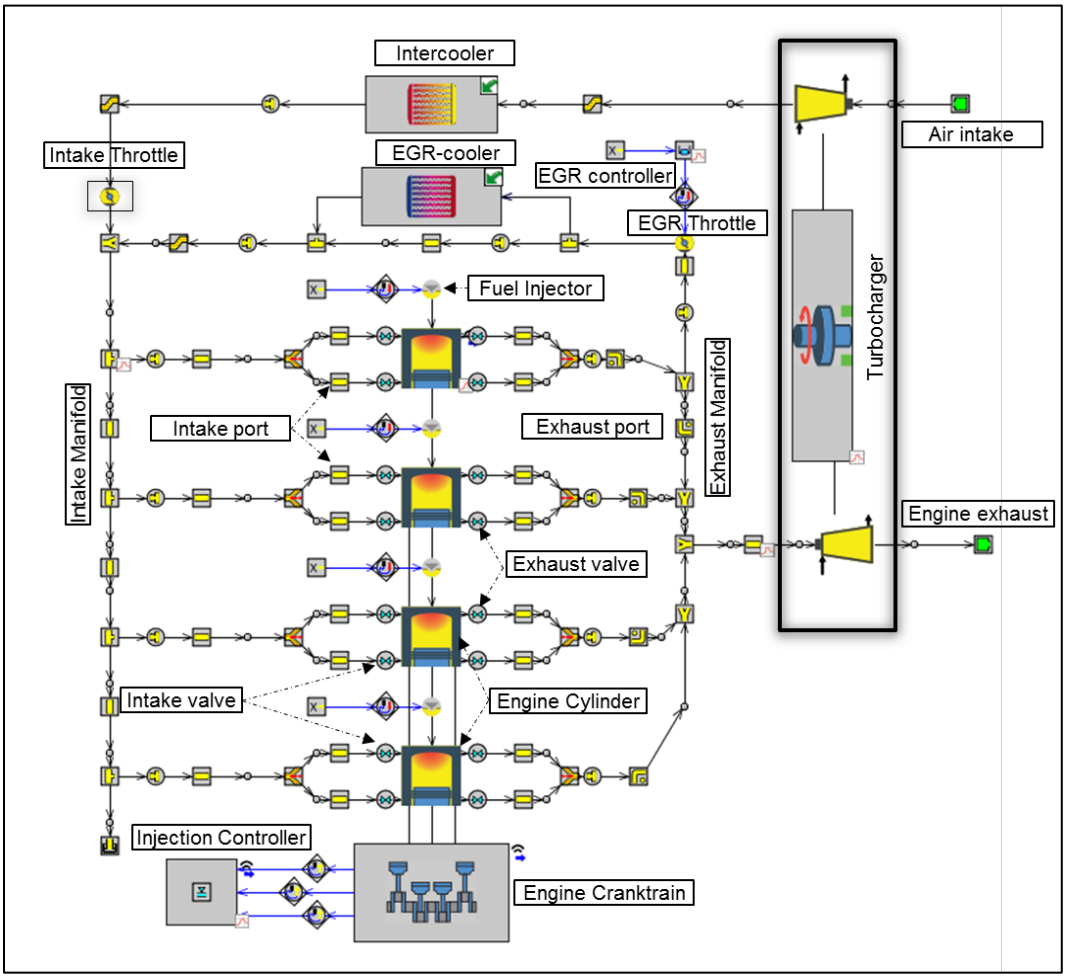

Figure 3.2: Engine simulation environment in GT-Suite®

3.2.1. Injection Model

ControllerDInject template was used in the model to target specific engine load and power, which will adjust the amount of fuel injected to the cylinder. This injection model can control engine output, including BMEP, brake-torque, and brake-power by adjusting the amount of fuel to be injected by the injector for a specific operating point. The fuel is

injected using the map-based injector, which allows multiple pulse injections. The map-based injector can predict the experiment results with high level of accuracy in terms of mass flow rate and the amount of total mass injection with maximum standard deviation less than 6% [64]. The injection rate map is based on BOSCH real injection model developed and validated by GT using experimental data provided in the reference.

3.2.2. Combustion Model

Predictive direct-injection (DI) diesel multi-pulse combustion model can accurately predict the effect of injection strategy and EGR on combustion rate and emission [65]. For this reason, experimentally verified combustion model and emission model were integrated into the model to study performance and emission of the engine.

DI-Pulse is a three-zone predictive combustion model in which the cylinder volume is discretized into three thermodynamic zones unburnt zone, spray unburnt zone, and spray burnt zone [65]. This model is sensitive to the burn rate, so experimentally verified multi-pulse combustion model developed by IAV GmbH is used for this study. This combustion model is validated for the 2L diesel engine with a similar application that have shown acceptable results. This thesis uses the combustion model parameters provided by IAV. The equations that are used for detail modeling and calibration of DI combustion model in GT-Suite® is included in Appendix A. Detail modeling procedure and explanation of these parameters can be found in the reference [66].

3.2.3. Emission Model

Extended Zeldovich NOx model is used to predict NO formation during combustion. This model is sensitive to oxygen percentage availability and temperature in the cylinder. NOx model is also provided by IAV GmbH, and the calibrated multiplier parameters are directly used in the emission model for this study as it shows good results for similar application.

These multipliers are used as parameters in the reaction rate Equations (B-1), (B-2) and (B-3) that are calibrated from the experimental data. The mechanism of NOx formation used for the extended Zeldovich NOx model are adapted from the reference [67]. The principal reactions involve formation of NO from molecular nitrogen and their reaction rates are included in Appendix B. Default GT-Suite® soot emission model based on two-step oxidation model, proposed by Morel and Deribar [68] and then improved by Morel, and Wahiduzzaman [69] is used to predict soot emission.

3.2.4. Heat Transfer Model

The cylinder heat transfer model used for simulation is WoschniGT which indicates that in-cylinder heat transfer is calculated using the similar equation used for classical Woschni correlation without swirl defined in "Internal Combustion Engine Fundamentals" by John B. Heywood [67]. The selection of heat transfer model can affect the predicted efficiency by 5%. Woschni model is dependent of engine heat transfer coefficient and remains constant over the range of equivalence ratio [70]. WoshcniGT model is used along with Chen-Flynn friction correlation discussed in section 3.2.5. In addition, cylinder wall temperature solver is used that will predict the structure temperature and surface temperature used in in-cylinder heat transfer calculation. Convective heat transfer rate for unburned and burned zones inside the combustion chamber is represented by the equations provided in Appendix C.

3.2.5. Engine Friction Model

Chen Flynn Engine Friction model is used as an engine friction model to evaluate the friction of the engine cylinder. The coefficients in the Chen Flynn model are commonly selected based on the literature published by Lavoie [70]. The model can predict thermodynamic efficiency within 3% of the experiment results expect for the homogeneous charge compression ignition at lowest load operation [70]. This model calculates engine

friction, which displays essential concept that friction is directly proportional to the peak cylinder pressure [70] shown in Equation (3-1).

$$\mathrm{FMEP} = \mathrm{FMEP_{Const}} + \mathrm{A} * \mathrm{P_{cyl,max}} + \mathrm{B} * \mathrm{c_{p,m}} + \mathrm{C}.\,\mathrm{c_{p,m}^2} \quad (3\text{-}1)$$

where,

$FMEP_{Const}$ is a constant part of friction mean effective pressure [bar]

A is the mean piston speed factor [bar s/m]

C is the mean piston speed squared factor [bar s^2/m^2]

$C_{p,m}$ is mean piston speed [m/s]

$P_{cyl,max}$ is maximum cylinder pressure [bar]

3.2.6. Turbocharger

A fixed geometry turbocharger is used in the model as the engine is supposed to be running at a single operating point. The efficiency of the turbine and compressor is kept constant. Turbocharging is an efficient way to boost engine power and torque without increasing engine size. The kinetic energy of exhaust gas is utilized by the turbine which drives compressor via a shaft. The compressor increases air density and temperature in the intake manifold and passes through an intercooler to cool down. Intercooler efficiency is not modeled, but the feature available in GT-Suite® is used to target the desired temperature downstream of the intercooler.

The components in the simulation environment are linked using round pipes, bend tubes, flow splits, of suitable dimension that would closely represent a realistic intake system and exhaust systems. In addition, thermal property for the wall is used along with external wall boundary condition to predict heat transfer from pipes and tubes accurately. However, the cooling of these components is not modeled. The intake throttle valve is used to control air-flow rate into the cylinder, and the EGR throttle valve is used to regulate the exhaust

gases going into the intake manifold. Exhaust gas passes through EGR cooler where it is sufficiently cooled down and mixed with intake air downstream of the intake throttle.

3.3. After-treatment Model

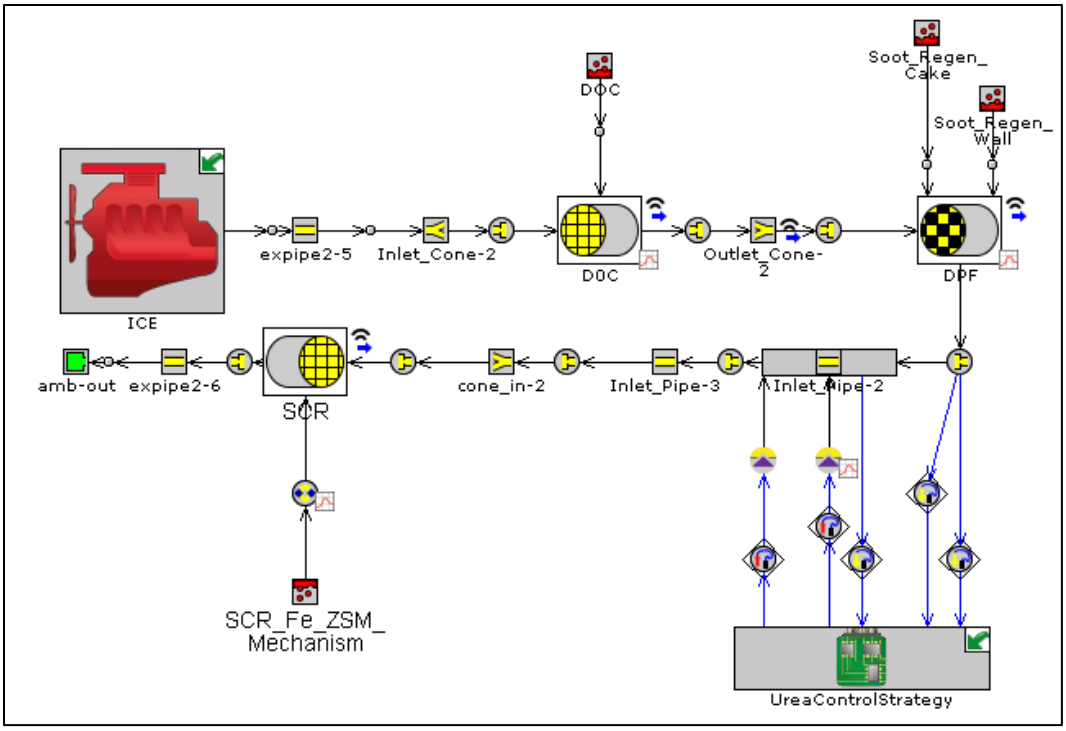

Figure 3.3: After-treatment model in GT-Suite®

The after-treatment model is connected to the outlet pipe downstream of the turbine and comprises catalyst brick and surface reaction sub-models, as shown in Figure 3.3 to represent detail reaction mechanism in the catalysts. Reaction kinetics objects account for bulk diffusion surface storage and surface reactions [71]. The dimension of catalyst substrate is provided in the catalyst brick along with other geometry as channel geometry, cell density, substrate wall thickness, and wash coat thickness. The catalyst substrate in GT-Suite® is represented by a substrate at the center and two outer walls, which can be seen in Figure 3.4. Outer wall layers are separated into sub-layers of different thickness

and material. Thermal properties of those layers are defined in the catalyst brick to predict the heat transfer from outer walls accurately. Data for the wall thermal property and thermal boundary condition for the catalyst brick is provided by IAV GmbH. These data are derived from geometrical data and recommend parameters are tabulated in Table 3.2 and Table 3.3 that shows plausible results.

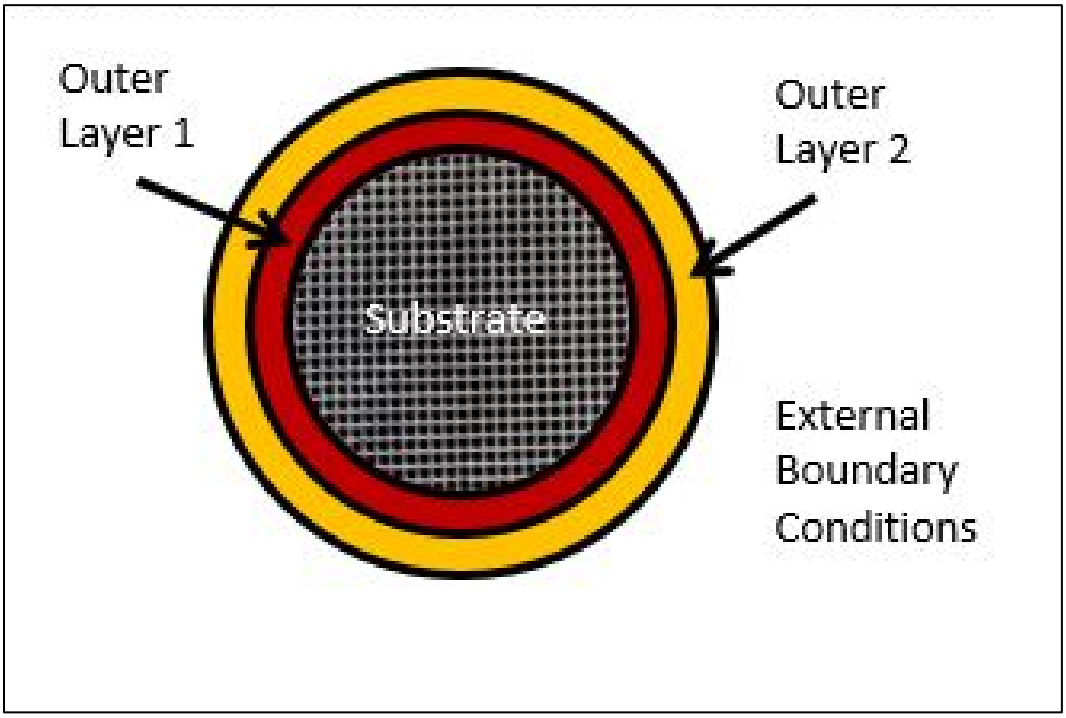

Figure 3.4: Catalyst brick representation in GT-Suite® – Adapted from reference [72]

Table 3.2: Wall thermal layer property of catalyst brick

Layer	**1**	**2**	**3**	**4**	**5**
Surface emissivity	0.6	0.1	0.6	0.8	0.6
Layer thickness (mm)	0.1	3	1.5	9	1.5
Layer material object	Cordierite	AirMatl	Canning	Insulation	Canning

Table 3.3: Wall thermal boundary condition for catalyst brick

External convection temperature	298.15 K
External radiation sink temperature	298.15 K
External convection coefficient	5 W/(m^2K)

Catalyst brick represents a flow-through or packed bed reactor connected to Surface Reaction template in GT power that defines catalytic surface reaction kinetics. The surface reaction in the catalyst is represented in the following standard form [72]:

$$R = A * \exp\left(-\frac{T_a}{A}\right) * \{conc\} * G(i) * \theta(i) \qquad (3\text{-}2)$$

where,

R is reaction rate (moles/sec)

A is pre-exponent multiplier

T is temperature (wall)

T_a is activation temperature

{conc} is concentration expression

G(i) is general and inhibition functions used for defining non-Arrhenius reaction rates, or any other general function of concentration, coverage, temperature or pressure, where 'i' is the index for the numerical position

θ(i) is coverage expression that specifies the coverage terms in evaluating the rate of progress of the reaction and 'i' is the index for the numerical positioning the coverage species

To accurately predict the detailed kinetic model inside that catalyst, pre-exponent multiplier and reaction rates must be calibrated for each reaction that occurs on the catalyst surface. GT-Suite® has a library of validated example model for DOC, DPF, and SCR, which is used for the thesis study. The architect of after treatment model

was chosen is DOC, DPF, and SCR in series with urea injection among different possible layouts.

3.3.1. DOC Model

The DOC model is taken from the example model provided by GT power, which functions as an oxidizer of HC, CO, and NO. The DOC model adapted from example is developed and validated by GT-Suite® using experimental data provided in reference paper [73]. The catalyst in the model uses Platinum group metal (PGM) and zeolites as site elements with active density 0.3 and zeolite 21.4, respectively defined in reference [73], and the reaction mechanism inside the catalyst is listed in Table 3.4.

The reaction mechanism includes oxidation of carbon monoxide, hydrocarbon, and Nitrous oxide that occurs at PGM site and adsorption and de-adsorption of unburned diesel fluid that takes place at the zeolite site. The reaction rates used in the model is first validated using curves generated by laboratory reactor experiments during light-off condition and it is further validated against the actual engine data for conventional and premixed compression ignition conditions [73]. So, it is assumed that model used can accurately predict conversion efficiency.

Table 3.4: Reaction mechanism in DOC catalyst – Adapted from reference [75]

Reaction site element	**Reactants**	**Products**	**Pre-exponent multiplier**	**Activation energy**
PGM	$CO+0.5O_2$	CO_2	1.18E+12	81330
PGM	$C_3H_6+4.5O_2$	$3CO_2+3H_2O$	1.57E+19	159400
PGM	$DF1+19.4O_2$	$13.5CO_2+11.8H_2O$	291800	24200
PGM	$DF2+19.4O_2$	$13.5CO_2+11.8H_2O$	291800	24200
PGM	$H_2+0.5O_2$	H_2O	98300	15310
PGM	$NO+0.5O_2$	NO_2	1327	6721

Zeolite	Z+DF1	ZDF1	13.48	0
Zeolite	ZDF1	Z+DF1	33060	45660

** DF1: adsorbable slow oxidizing HC

DF2: non-adsorbable slow oxidizing HC

Cordierite is used as a material for the substrate, and alumina is used as a washcoat. DOC geometry specification details are provided in Table 3.5. The intrinsic properties of the model are kept the same as reaction rates would be affected by altering those parameters. DOC length is varied for optimization, which is discussed in the following chapter considering a constant DOC diameter and assuming volume must be 0.5-1.5 times engine displacement [74].

Table 3.5: DOC geometry – Adapted from reference [72]

Frontal diameter	6”
Length	6”
Channel shape	square
Cell density	400 psi
Channel shape	square
Substrate wall thickness	150 microns
Washcoat thickness	30 microns

3.3.2. Catalyzed DPF Model

DPF sub-model for this study has been implemented in a similar manner as DOC, which uses measured data and reference from the published SAE paper [35]. A wall-flow filter used for DPF can predict pressure drop, particulate matter and ash filtration as well as soot regeneration and catalytic reaction. The geometry of the catalyst defined in the published paper was used by Gamma Technology for the development of the model, and the model was calibrated using the measured data from those papers. The additional reaction is

utilized to account for the NO oxidation reaction in the substrate, like the DOC model defined above. This catalyzed DPF model can predict soot regeneration in the cake layer and wall along with O_2 and NO_2 supported regeneration processes.

Table 3.6: Reaction mechanism for soot regeneration in the cake layer - Adapted from reference [75]

Reactants	**Products**	**Pre-exponent multiplier**	**Activation energy**
$C + NO_2$	$CO + NO$	1.00E+07	12000
$C + 2\ NO_2$	$CO_2 + 2\ NO$	1.00E+07	12000
$C + 0.5\ O_2$	CO	1.00E+08	24000
$C + O_2$	CO_2	1.00E+08	24000

Table 3.7: Reaction mechanism for soot regeneration in the wall - Adapted from reference [75]

Reactants	**Products**	**Pre-exponent multiplier**	**Activation energy**
$C + NO_2$	$CO + NO$	1.00E+07	12000
$C + 2\ NO_2$	$CO_2 + 2\ NO$	1.00E+07	12000
$C + 0.5\ O_2$	CO	1.00E+08	24000
$C + O_2$	CO_2	1.00E+08	24000
$NO+0.5O_2$	NO_2	1327	808.348

Two reaction mechanisms are connected to catalyst brick to define reactions for soot regeneration in cake and the wall. The reactions and reaction rates used for the kinetic model in GT-Suite® are listed in Table 3.6 and Table 3.7, and the specification of the DPF model used for simulation is tabulated in Table 3.8. DPF model is validated by GT-Suite® comparing the pressure drop and wall average temperature of the DPF with the experimental data that are shown in Figure 3.5 and Figure 3.6, respectively. The average

error values in pressure drop is 0.83 kPa with standard deviation of 0.97 kPa, and the mean error in wall average temperature is 17.95 K with standard deviation of 21.54 K. This model is used for the study as the comparison results show that the simulation data is close to measured data with acceptable margin of error.

DPF volumes are given reasonable values through technical practice and data provided in the literature [44], and the length of DPF is modified to promote continuous regeneration process inside DPF.

Table 3.8: DPF geometry specification - Adapted from reference [76]

Frontal diameter	6”
Length	10”
Channel shape	square
Cell density	200 psi
Channel shape	square
Substrate wall thickness	304.8 micron

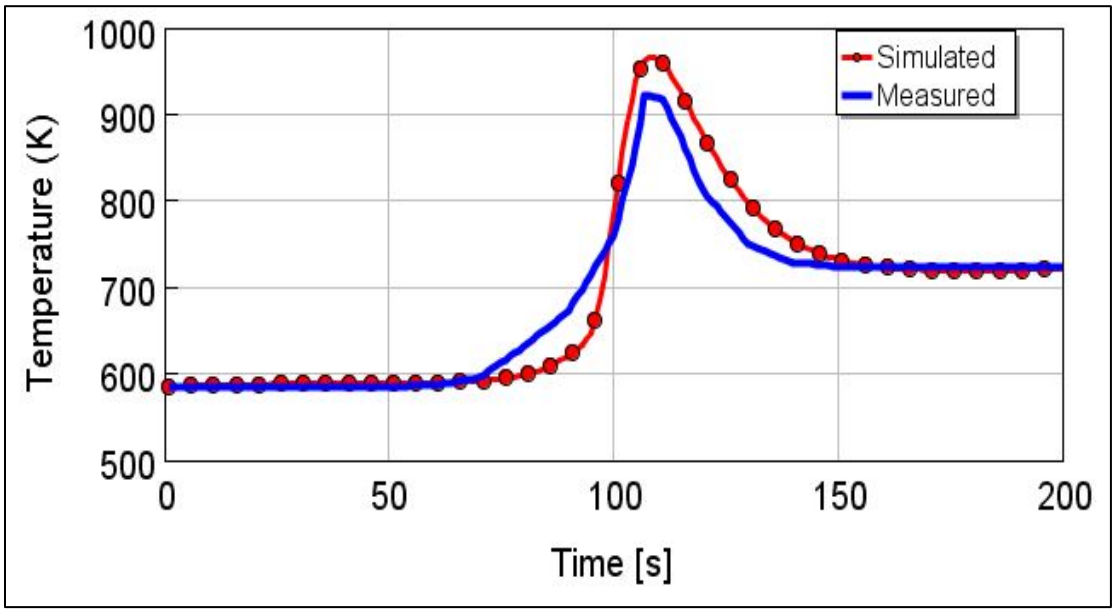

Figure 3.5: Comparison of simulated and measured data for the average wall temperature of DPF- Adapted from reference [77]

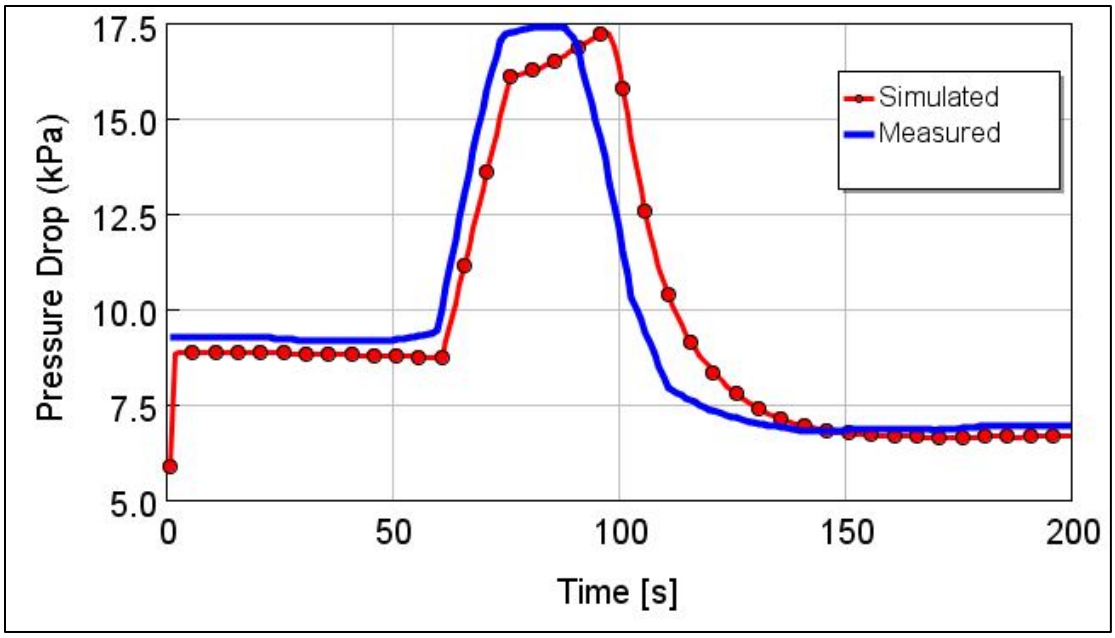

Figure 3.6: Comparison of simulated and measured data for pressure drop across DPF- Adapted from the reference [77]

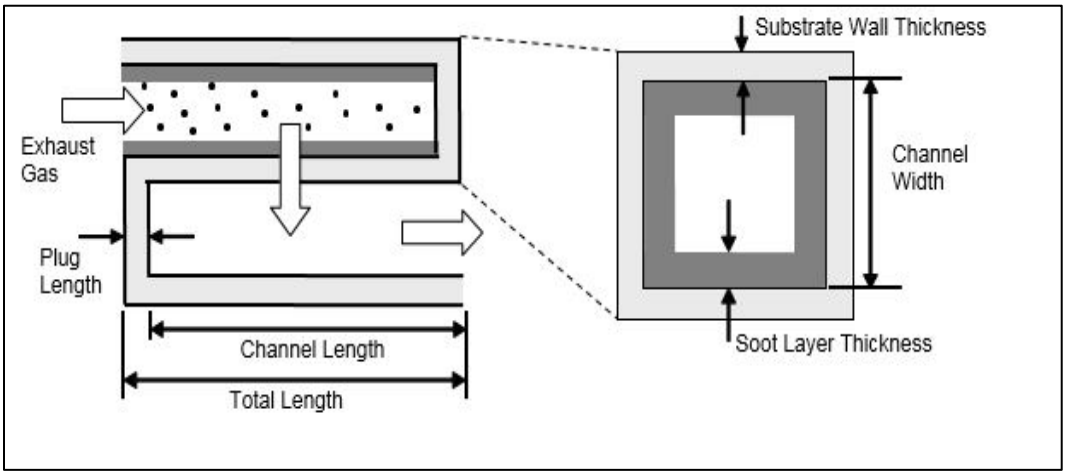

Figure 3.7: DPF geometry used in GT-Suite®:-Adapted from reference[78]

3.3.3. SCR Model

SCR components in the after-treatment model are taken from GT-Suite® SCR example models that use reaction mechanism, catalyst geometry, and inlet gas composition published in the reference [44]. The model is validated using experimental data published in the reference that covers detailed reaction chemistry inside SCR catalyst. The model also accounts for temperature-dependent gas diffusivity of different species that limits diffusion in NH_3-SCR model. NOx reduction by NH_3-SCR mechanism includes ammonia adsorption-desorption, Ammonia oxidation, NO oxidation, standard SCR, fast SCR, NO_2 SCR listed in the Table 3.9, which has been utilized to develop a global kinetic model. Performance of two SCR models Fe-zeolite and Cu-Chabazite are studied for this thesis. The reaction mechanism in those catalysts is listed in Table 3.9 and Table 3.10. It can be noticed that the reaction mechanism is almost the same, but the reaction rates vary due to the difference in the material property.

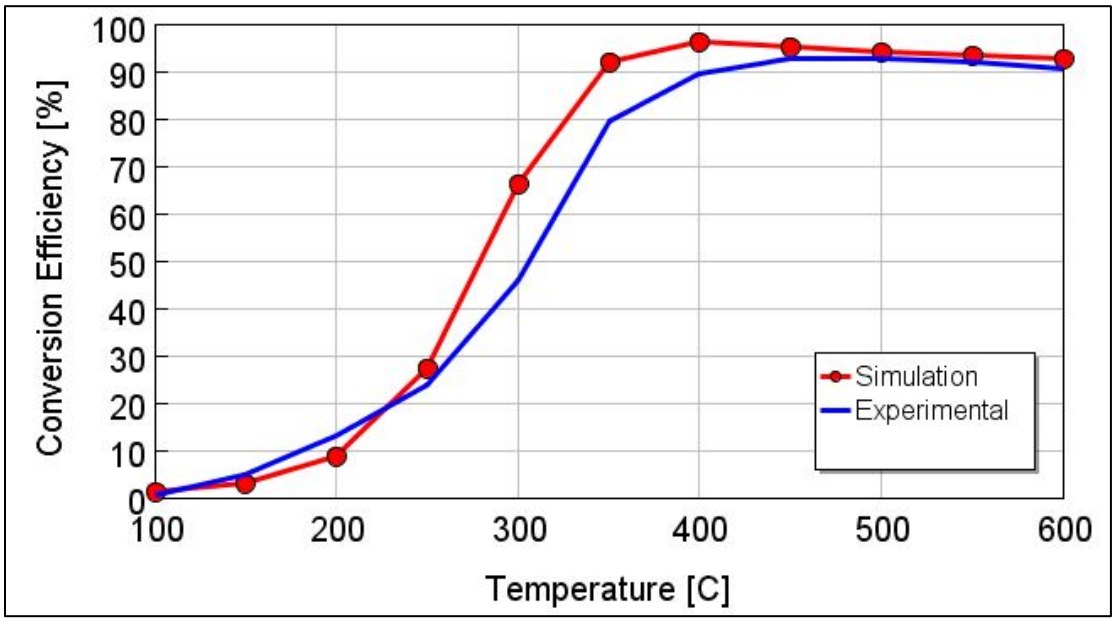

Figure 3.8: Comparison of simulation and experimental data for NOx conversion efficiency in Fe-Zeolite catalyst-Adapted from the reference [77]

Table 3.9: Reaction mechanism for Fe-Zeolite catalyst- adapted from reference [75]

Reaction site element	**Reactants**	**Products**	**Pre-exponent multiplier**	**Activation energy**
Fe-Z1	NH_3 + Z1	Z1NH_3	54.6	0
Fe-Z1	Z1NH_3	NH_3 + Z1	3.00E+08	0
Fe-Z1	2Z1NH_3 + 1.5O_2	N_2 + 3H_2O +2Z1	10000	11530
Fe-Z1	NO + 0.5O_2	NO_2	5.44	3210
Fe-Z1	4Z1NH_3 + 4NO +O_2	4N_2 + 6H_2O +4Z1	2140000	9090
Fe-Z1	2Z1NH_3 + NO + NO_2	2N_2 + 3H_2O + 2Z1	1.16E+13	9630
Fe-Z1	4Z1NH_3 + 3NO_2	3.5N_2 + 6H_2O + 4Z1	3.00E+12	17490

Fe-Z1	$2Z1NH_3 + 2NO_2$	$N_2 + Z1AN + H_2O + Z1$	18000	5420
Fe-Z1	Z1AN	$N_2O + 2H2O + Z1$	50000	5060
Fe-Z1	$2N_2O$	$2N_2 + O_2$	6.40E+07	16000
Fe-Z1	$2Z1NH_3 + 3\ N_2O$	$4N_2 + 3H_2O + 2Z1$	2350000	11440

** Fe-Z1: Fe zeolite

Z1: substrate

AN: Ammonium nitrate

Table 3.10: Reaction mechanism for Cu-chabazite catalyst- Adapted from reference [75]

Reaction site element	**Reactants**	**Products**	**Pre-exponent multiplier**	**Activation energy**
Cu-CHA	$NH_3 + S$	$S-NH_3$	6.68E+07	0
Cu-CHA	$S-NH_3$	$NH_3 + S$	4.00E+15	0
Cu-CHA	$2S-NH_3 + 1.5O_2$	$N_2 + 3H_2O + 2S$	5.56E+16	178.8
Cu-CHA	$NO + 0.5O_2$	NO_2	5.10E+07	56
Cu-CHA	$4S-NH_3 + 4NO + O_2$	$4N_2 + 6H_2O + 4S$	7.08E+13	89.1
Cu-CHA	$2S-NH_3 + NO + NO_2$	$2N_2 + 3H_2O + 2S$	1.00E+18	77.1
Cu-CHA	$4S-NH_3 + 3NO_2$	$3.5N_2 + 6H_2O + 4S$	1.96E+17	136.3
Cu-CHA	$2S-NH_3 + 2NO_2$	$N_2 + S-AN + H_2O + S$	2.28E+08	43
Cu-CHA	S-AN	$N_2O + 2H_2O + S$	1.25E+08	41.5

** Cu-CHA: Cu chabazite

AN: Ammonium Nitrate

S: Substrate

Table 3.11: Catalyst specification for SCR catalyst - Adapted from reference [72]

Frontal diameter	6”
Length	4.5”
Channel shape	square
Cell density	400 psi
Channel shape	square
Substrate wall thickness	165 microns
Washcoat thickness	50 microns

The Fe-zeolite and Cu-chabazite SCR models are is also validated by GT-Suite® using simulation and the experimental data. The mean errors in NOx conversion efficiency is 5.24% with standard deviation of 6.10% for Fe-zeolite catalyst, and 3.74% with standard deviation of 4.74% for Cu-chabazite catalyst. The results for Fe-zeolite model validation is shown in Figure 3.8 indicating that the simulation model can predict the NOx conversion efficiency with some acceptable errors. So, it is assumed that inbuilt SCR model is a good fit for this study. The catalyst geometry specifications used for simulation are listed in Table 3.11 [44], and like DOC and DPF, only length of the catalyst was varied that would meet NOx emission target for a future vehicle.

3.3.4. Urea Control Strategy

Urea control strategy plays a vital role in the conversion of NOx emission in the active catalyst site. Thus, urea dosing strategy is defined in the model that includes injector and controller block. For simplicity of the model, NH_3 is injected upstream of SCR catalyst instead of urea solution because the reaction mechanism defined in the published journal [44] verified by GT-Suite® can be directly used without any modification. The amount of

NH_3 to be injected is determined by sensing NOx molar flow rate upstream of SCR. The amount of NH_3 injected is calculated using a formula in the equation below:

$$\dot{m}(NH_3) = (\text{molar flow rate})_{NO_x} * (\text{molecular mass})_{NH_3} * \text{TF} \qquad (3\text{-}3)$$

where,

$\dot{m}$ is the mass flow rate

TF is a temperature factor

Temperature dependent factor is used for NH_3 injection to improve NOx conversion and reduce urea consumption. The temperature dependent factor is determined based on two factors

- NH_3 oxidation on catalyst surface at a higher temperature (above 400^0 C).
- NH_3 higher adsorption by catalyst at a lower temperature (below 300^0 C).

NH_3 is directly injected into the pipe upstream of SCR, so, thermal decomposition and iso-cyanic acid hydrolysis reaction model is not required to be implemented. A simple control strategy was implemented that has been used for optimal NOx conversion and urea consumption, which is as follows:

- Start dosing of urea after the temperature in SCR reaches 200^0 C as urea solution will crystallize at a lower temperature
- NH_3 slip mechanism is implemented which senses NH_3 concentration downstream of SCR and stops dosing if the concentration is greater than 5 ppm

3.4. Vehicle and Hybrid Powertrain Model for Forklift

Hybrid powertrain model for forklift includes engine, ECU, generator, battery, BMS, electric motor, supervisory controller, and vehicle model, which can be seen in Figure 3.1. Modeling of lifting mechanism is complex and requires major efforts for development, so for simplicity of the model, an electric motor is used that draws energy from the system to

follow load profile during lifting. Modeling of each component for the GT-Suite® simulation environment is described below.

3.4.1. Vehicle Model

The vehicle model is represented by a vehicle body model that is connected to the front and rear axles, as shown in Figure 3.9. This model calculates the longitudinal motion of the vehicle and loads on each axle. The traction motor is connected to the differential via shaft and differential rotates both the connected axles to rotate wheels in order to move vehicle. In forklift application generally, the differential uses two sets of reduction gear to attain high torque output but for simplicity large final drive ratio is used that accounts for both gear reduction. The vehicle is a front-wheel drive as forklift load carrier is located at the front part. Vehicle details are provided which is used to compute required force on the wheel at different speeds. Friction brakes are adopted in the model for instantaneous braking. The friction pedal position is determined by the brake controller using the following equation [79]:

$$\text{Brake Pedal} = \left(\frac{30000 * \text{Brake Demand}}{2 * \pi * \text{Speed}_{\text{axle}} * \text{T}_{\text{max}} * \text{N}_{\text{Axles}}}\right) * 100\% \quad (3\text{-}4)$$

where,

T_{max} is the maximum Brake Torque

$Speed_{axle}$ is the speed of the axle

N_{axles} is the number of axles

Road gradients can also be incorporated using a road template. The vehicle model in GT-Suite® is shown in Figure 3.9. The detail specification of the forklift vehicle model used for simulation is provided by IAV GmbH that are listed in Table 3.12.

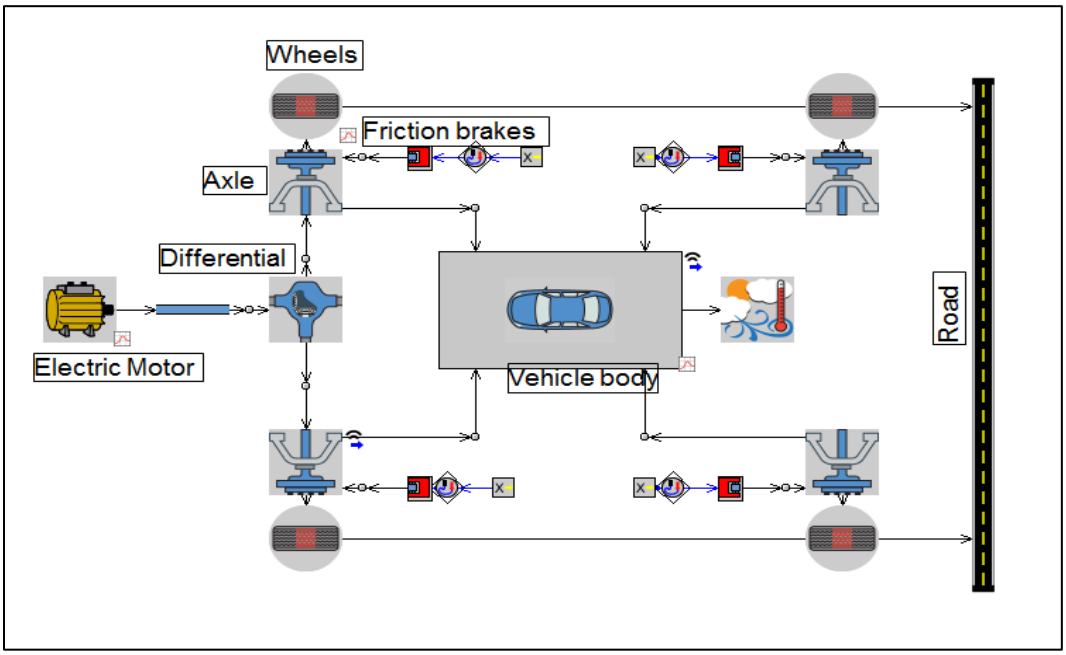

Figure 3.9: Vehicle model in GT-Suite®

Table 3.12: Forklift vehicle specification

Vehicle mass	7300 kg
Passenger and cargo Mass	5000 kg
Vehicle drag coefficient	0.7
Vehicle frontal Area	3 m^2
Vehicle wheelbase	2 m
Horizontal dist from last rear axle to the center of mass	1.75 m
Vertical distance from axles to the center of mass	0.2 m
Explicit tire rolling radius	0.42 m
Maximum static brake torque	2000 N-m
Brake effective radius	0.1 m

3.4.2. Driver Model

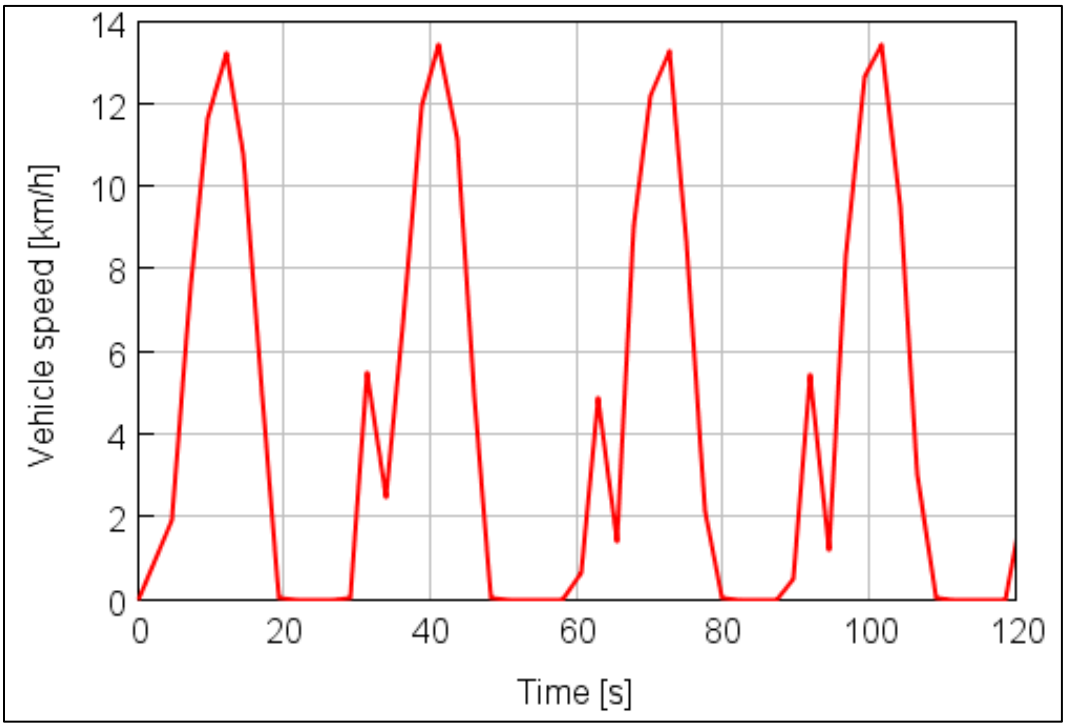

Figure 3.10: Vehicle speed profile for VDI cycle extracted from reference[10]

The vehicle speed is targeted to the drive cycle speed based on which vehicle torque loss and torque demand are determined by driver template in GT-Suite®. It should be noted that the driver model must be compatible with the chassis and wheel models as they all use vehicle dynamics equations. Driver profile is connected to the vehicle and determines the required traction power demand to follow the drive cycle. The VDI drive cycle speed profile shown in Figure 3.10 is utilized in driver template to evaluate the fuel consumption and performance of powertrain.

3.4.3. Engine and Generator

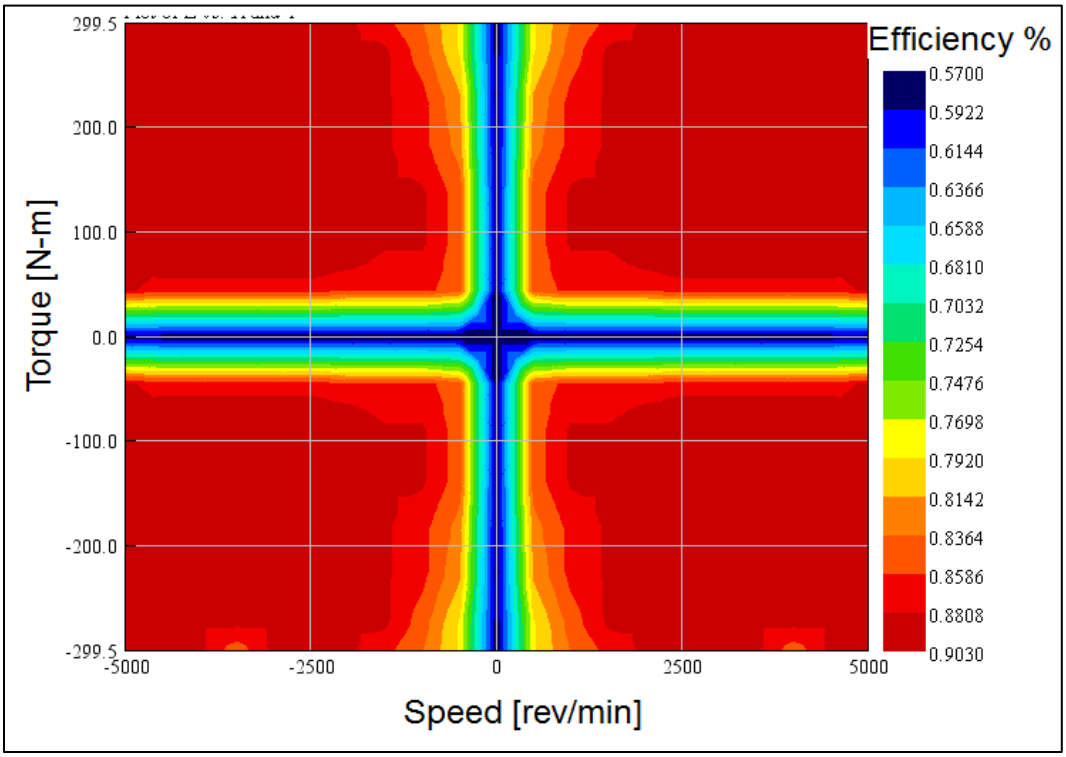

Figure 3.11: Generator efficiency map – Adapted from reference [80]

For the hybrid powertrain, engine speed and torque outputs are essential parameters as it determines the electrical power output of the generator. A map-based generator model is defined for an electric motor that uses engine speed and torque as input. The input speed and torque are converted electromechanically to electrical power by a generator. The engine is connected to the generator via a shaft and gear connection, and speed is matched for optimal efficiency. The generator also rotates crank train, so that engine speed suitable for fuel injection is reached during engine start. The characteristic curve of the motor in GT-Suite® is modified so that the generator operates at a better efficiency point. The efficiency curve of the generator is shown in Figure 3.11. Inverter efficiency is provided as 0.95 that would account for electromechanical conversion losses. The peak power chosen for the generator is 55 kW with a base speed of 1500 rpm so that the generator runs

at optimum efficiency point as continuous output power delivered by the engine is 35 kW at 2000 RPM.

3.4.4. Traction Motor

GT-Suite® provides both map-based and simplified electromechanical models for a motor/generator. In the map-based model, efficiency map and torque map are provided to meet the required performance. The motor is driven with an applied voltage, and a simple circuit is solved to compute power output in GT-Suite®. Traction motor uses the same map-based motor as a generator which is connected to drive shaft and propels the vehicle. Traction motor can be employed for regenerative braking and energy captured during regenerative braking is utilized for charging the battery. The traction motor is designed to meet power demand for maximum speed, maximum grade ability, and maximum acceleration is given by the Equations (3-5), (3-6) and (3-6), taken from the design of series hybrid drive train for off-road vehicle chapter of the reference [49]. These estimations will help to determine the capacity of the electric motor to achieve the required performance of powertrain.

1.Power requirement for maximum vehicle speed

$$P_1 = \frac{v}{\eta_{motor}}\left(mgf_R + \frac{1}{2}A\,C_A\,\rho_A v^2\right) \tag{3-5}$$

2.Power requirement for maximum road grade

$$P_2 = \frac{v}{\eta_{motor}}\left(mg\sin\emptyset + mgf_R\cos\emptyset + \frac{1}{2}A\,C_A\,\rho_A v^2\right) \tag{3-6}$$

3.Power requirement for the acceleration time

$$P_3 = \frac{m}{2t}\left(v_{rm}^2 + v_{rv}^2\right) \tag{3-7}$$

4.Final drive ratio

$$FDR = \frac{2r_{dyn}\,\pi\,RPM_{max}}{60\,v_{max}/3.6} \tag{3-8}$$

where,

r_{dyn} is vehicle dynamic wheel radius (m)

v_{max} is maximum vehicle speed (km/h)

RPM_{max} is maximum motor speed (rpm)

v is maximum vehicle speed (m/s)

n_{motor} is motor/controller assembly efficiency

m is vehicle mass + load (kg)

g is gravity constant (m/s^2)

f_R is rolling resistance coefficient

A is front area (m^2)

C_A is air drag coefficient

ρ_A is density of air (kg/m^3)

$\emptyset$ is maximum road grade (radian)

v_{rv} is vehicle rate speed (m/s)

v_{rm} is accelerating target speed (m/s)

t is acceleration time (s)

3.4.5. Battery

GT-Suite® has several battery models, including a lithium cell, calibrated against the experimental data from actual production cell. The model consists of all the required maps, including open circuit voltage (OCV), internal resistance maps for charging and discharging cases shown in Figure 3.12 that can accurately predict the performance of the battery. The lithium-ion battery is chosen as it offers better mass-energy density and efficiency for a longer lifetime, making it a popular power source for HEV application [81]. The electrical equivalent battery model is used in GT-Suite® and battery specification as a number of cells in series and parallel, cell capacity is provided. These battery specifications determine the performance of series hybrid powertrain so, they are carefully

modeled. Power capacity is determined using the Equation (3-9) taken from the reference [49].

$$P_{battery} = \frac{P_{motor}}{\eta_{motor}} - P_{e/g} \tag{3-9}$$

The GT-Suite® battery model uses Equations (3-10), (3-11), (3-12) and (3-13) to determine capacity, open circuit voltage, resistance, maximum available power, and capacity of the battery pack.

Capacity of battery pack

$$Cap_{Battery-pack} = N_p * Cap_{cell} \tag{3-10}$$

Open circuit voltage (V_{OC})

$$V_{OC,Battery-pack} = N_s * V_{OC,cell} \tag{3-11}$$

Resistance of battery pack

$$R_{Battery-pack} = \frac{N_s}{N_p} * R_{cell} \tag{3-12}$$

Maximum available power

$$P_{Max} = \frac{{V_{OC}}^2}{4 * R_o} * R_{cell} \tag{3-13}$$

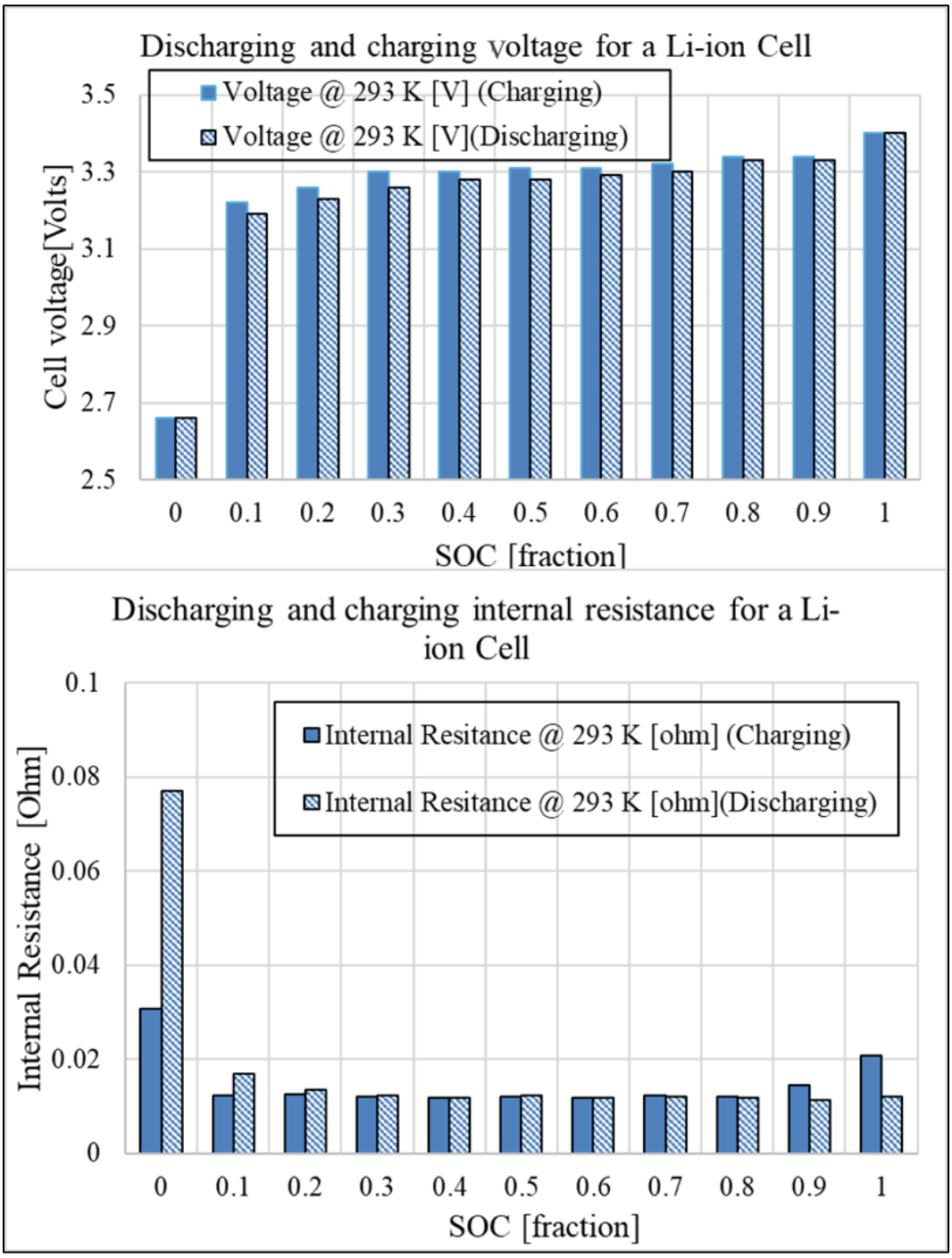

Figure 3.12: Li-ion cell voltage and internal resistance for charging and discharging – Data extracted from reference [82]

3.4.6. Battery Management System (BMS)

In GT-Suite®, battery power limiter is used in conjunction with the battery for BMS. BMS prevents from exceeding maximum discharge and charge power when the battery is connected to electrical and electromagnetic components [82]. In a real application, BMS plays a vital role in preventing damage of electrical parts, so battery power limiter is implemented in the model that limits electrical power depending on the maximum available discharge and charge battery power.

BMS also serves as inverter and power converter that determines if additional power is required from the battery or excessive power is present that can be used for charging the battery. The BMS calculates the charging and discharging limits of battery by generator and motor. If power demand is higher while the engine is running, additional power is provided by a battery, but when the engine is producing extra power than required for traction, the remaining energy is utilized in charging the battery. BMS automatically determines the situation and performs the necessary action.

3.4.7. Hydraulic Load

Hydraulic load profile for 5-ton forklift truck is adapted from the reference [10]. It is used to estimate fuel consumption and energy usage. Battery or engine/generator power will supply the power required to follow the drive cycle. A simple electric motor was used with base speed 1500 rpm and peak power of 50 kW for hydraulic motor. The hydraulic motor in the real application is connected to the hydraulic pump that forces liquid at high pressure to raise the lift jack. The forks raise load on a mast using chains and rollers, which can be tilted backward by tilt jacks to aid in the stability [83]. The load profile shown in Figure 3.13 is given to hydraulic motor, and it draws necessary power from the available energy sources to follow that load profile.

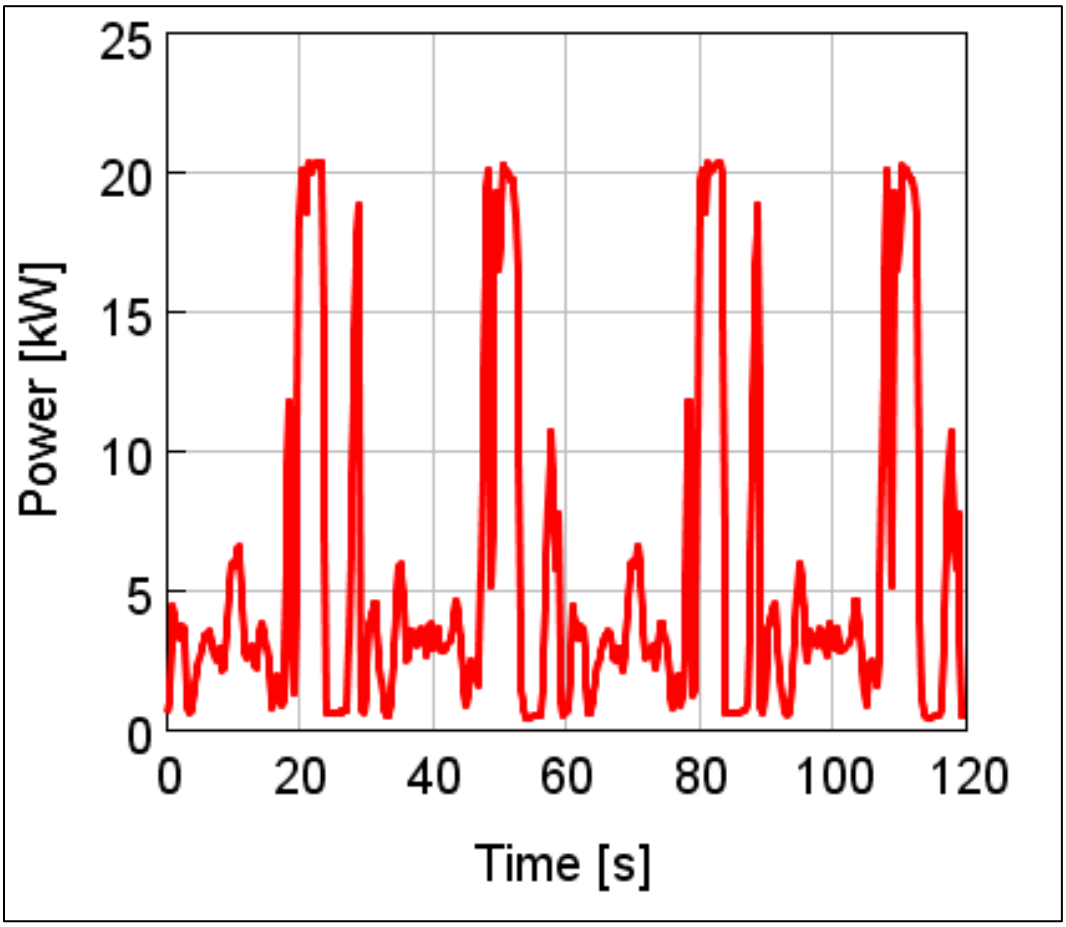

Figure 3.13:Hydraulic load profile of 5-ton forklift truck for VDI cycle; extracted from reference[10]

3.4.8. HEV Supervisory Controller

The HEV supervisory controller determines operating modes of the hybrid powertrain architect depending on the load, amount of braking, light-off temperature, and energy present in the battery. If-Then-Else blocks and event manager blocks are used in GT-power to model supervisory controller as shown in Figure 3.14. It can be further categorized into regenerative brake controller and charge state level controller. Inside regenerative brake controller block traction power demand, vehicle speed profile, regenerative braking limit,

and battery SOC determine the operating mode of the vehicle as well as split power between the regenerative brakes and friction brakes.

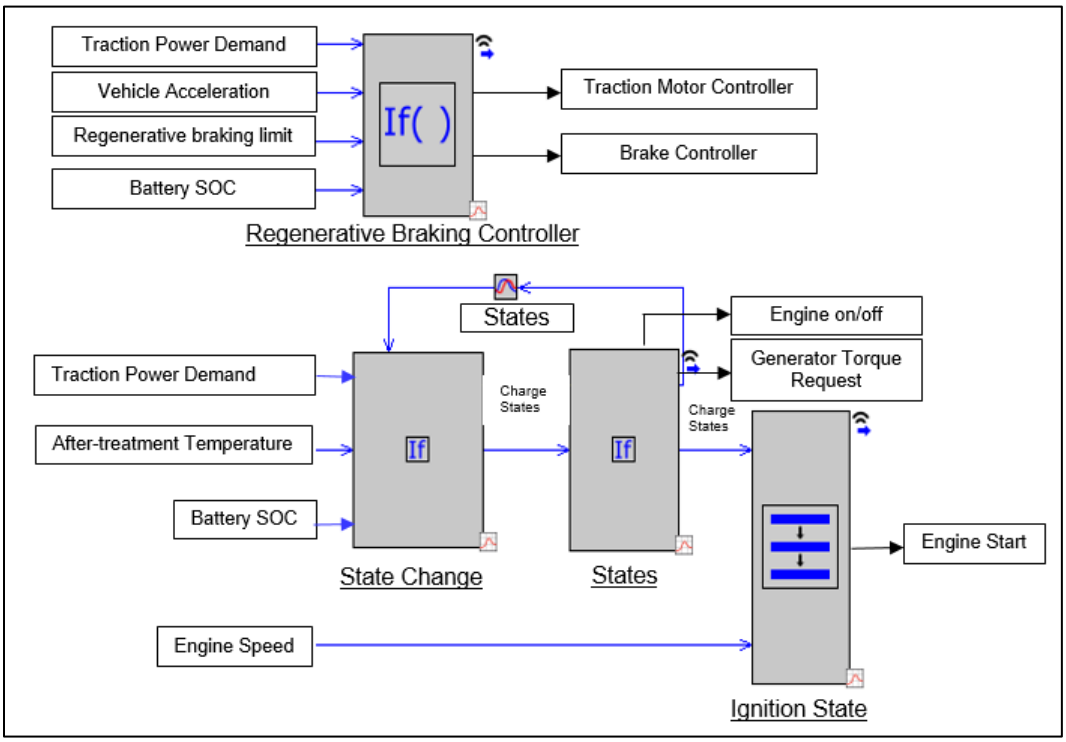

Figure 3.14: Supervisory control block in GT-Suite®

The flow chart in Figure 3.15 shows how operating modes are selected for a series hybrid powertrain. Different operating modes are defined using control blocks, including braking modes. First, traction power demand and braking power demand is determined. Three braking modes: friction braking, regenerative braking, and hybrid braking are incorporated in the model that are computed based on vehicle deceleration, maximum regeneration limit and SOC of the battery. Then power sources are determined that will deliver required traction demand depending on battery SOC, SCR temperature and engine power. The power is delivered either by battery or engine. When traction power demand is high, hybrid traction mode is used to meet the power demand, and the battery is charged by power produced from the engine-generator combination during the low load operation.

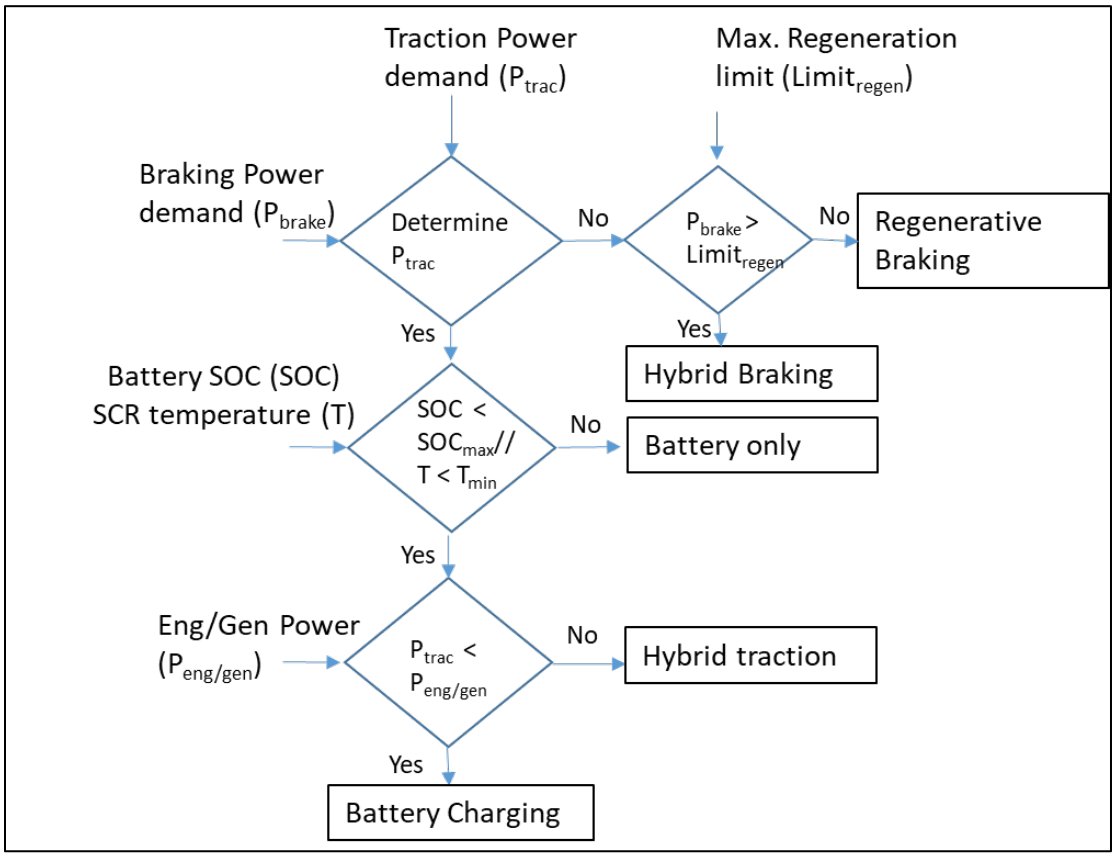

Figure 3.15: Control flow chart of the max. SOC of the battery control strategy

3.5. Summary

Table 3.13 provides a list of all the pre-validated sub-models that has been used for this study. These models are implemented to study the performance of the engine, after-treatment system, and powertrain components.

Table 3.13: List of pre-validated models used for the study

Models	Source	Remarks
Combustion model	IAV GmbH	Experimentally verified model
NOx emission model	IAV GmbH	Experimentally verified model

Injection model	GT-Suite® library	This model can predict mass flow rate and the amount of total mass injection with maximum standard deviation error of less than 6% [64].
Heat transfer and Friction model	GT-Suite® Library	The model can predict thermodynamic efficiency within 3% of the experiment results [70].
DOC model	GT-Suite® library	The model is validated using curves generated by laboratory reactor experiments during light-off condition and, further validated against the actual engine data for conventional and premixed compression ignition conditions.
DPF model	GT-Suite® library	The average error values in predicting pressure drop is 0.82 kPa with std. deviation of 0.97 kPa and the mean error in wall average temperature is 17.9 K with deviation of 21.5 K [90]
SCR model	GT-Suite® library	The mean errors in NOx conversion efficiency is 5.24% with standard deviation of 6.10% .
Wall thermal property model for after-treatment	IAV GmbH	Derived from geometrical data and recommend parameters are used that shows plausible results.
Vehicle model	IAV GmbH	Validated with data from the specification sheet of a forklift

Chapter 4: Engine and After-treatment Optimization

4.1. Introduction

The engine model is set up in the GT-Suite® simulation environment with all the necessary specifications. The model is first validated using the data from experimentally verified IAV engine model for a single operating point. The provided engine performance data are acquired from the 2 L diesel engine used for a similar application. The IAV engine model is validated from the experimental data, shown in Figure 4.1. The results show coefficients of determination for torque, AFR, peak cylinder pressure and NOx measurement as 0.999, 0.998, 0.986, and 0.805. These values indicate that the experimentally verified IAV engine model can accurately predict the engine performance and emission. Therefore, the results acquired from this model is utilized for validating the baseline engine developed for this study.

Parameters such as injection timing, boost pressure, cylinder overall convection multiplier were calibrated to match developed engine model with an experimentally verified IAV engine model. Temperature downstream of intercooler and EGR cooler depends on cooling efficiency of those two components. So, to reduce the task of calibrating efficiency of intercooler and EGR cooler, constant temperature is imposed for this study using heat exchanger connection model in GT-Suite®.

Table 4.1 shows the summary of engine performance at a single point for the baseline engine model developed for this study, and the experimentally verified IAV engine model used in a similar application. It can be noticed that brake specific fuel consumption (BSFC), peak cylinder pressure, air mass flow rate, and BSNOx differ by less than 5%. Boost pressure of 2 bar for the developed model would result in a higher amount of airflow, increasing AFR, and change all the performance parameters. So, the boost pressure of 1.75 bar was used for the baseline model that will reduce the difference in the air mass flow rate

and AFR. This limits how closely the model and experimental data can be since the assumption needed to be made. The pressure ratio is, however, kept constant as intake manifold pressure, and exhaust back-pressure differs slightly more than 12%. It should be noted that limited engine data specification data could be provided by IAV GmbH due to confidentiality.

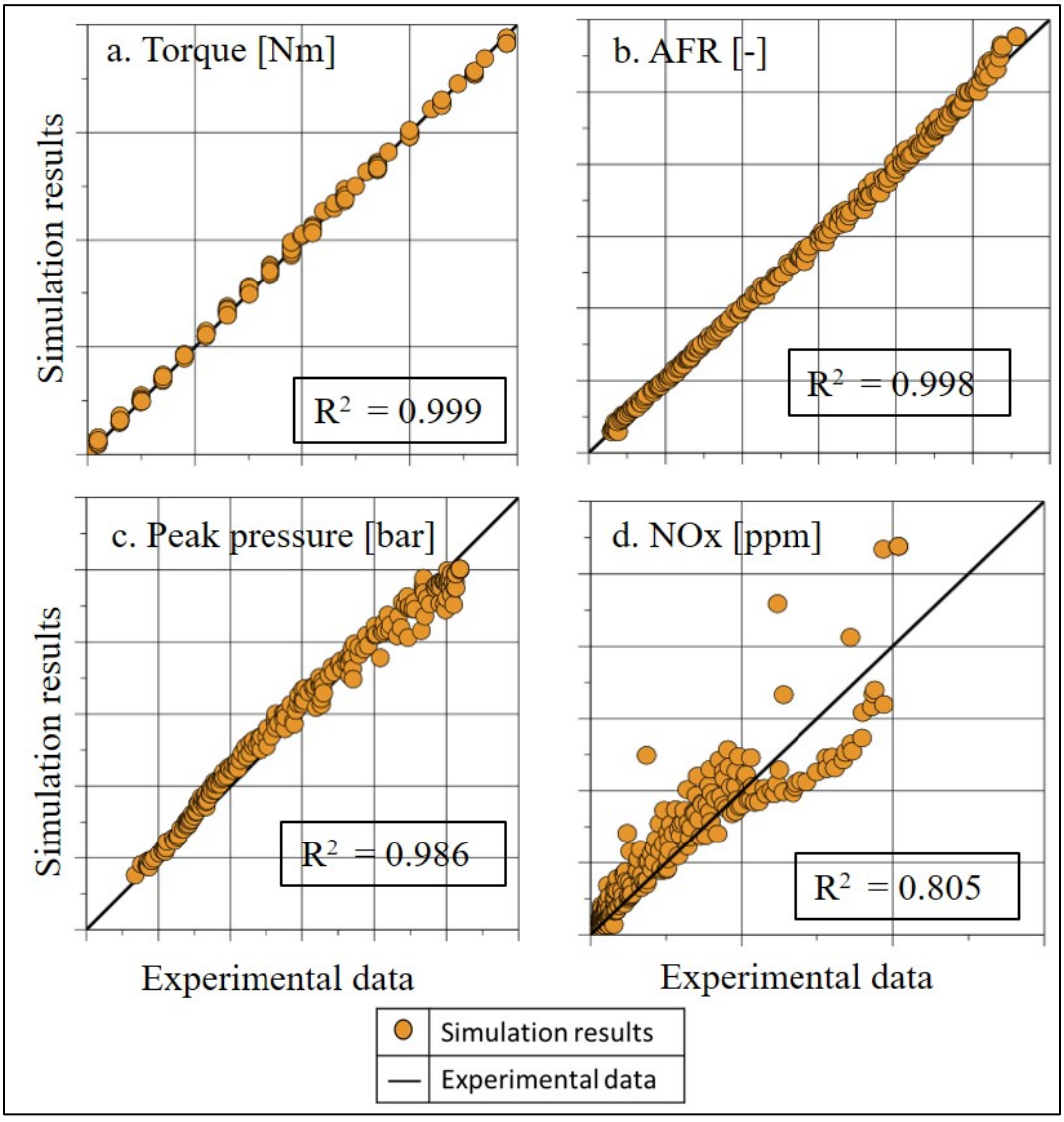

Figure 4.1: Validation of IAV engine model with experimental data: Data is provided by IAV GmbH

Table 4.1: Validation of the baseline engine model developed in GT-Suite®

Engine operating point: 35 kW @ 2000 RPM			
Specification	**Experimentally verified IAV engine model**	**Baseline engine model**	**Percentage difference**
BSFC [g/kW-hr]	211.1	211.8	0.3%
Peak in-cylinder pressure [bar]	127.0	120.8	4.9%
Air mass flow rate [kg/hr]	150.0	150.5	0.3%
AFR	20.3	20.4	0.4%
EGR [%]	22.8	24.3	6.5%
BSNOx [g/kW-hr]	3.32	3.38	1.81%
Intake manifold pressure [bar]	2.0	1.75	12.5%
Exhaust back pressure [bar]	2.14	1.87	12.62%
Pressure ratio	1.07	1.07	0%
Combustion start [CA deg. ATDC]	NA	0.49	-
50% burned crank angle [CA deg. ATDC]	NA	6.83	-
Start of injection [CA deg. ATDC]	NA	-2.0	-

Understanding of engine performance is essential to select the optimum engine operating point for given engine speed and load. Due to the development of advanced control, it is possible to run the engine at that sweet spot even in changing conditions. So, the study of this thesis is focused on the optimization of engine for optimal fuel efficiency and better conversion efficiency of the after-treatment system that will restrict emission to certain limits.

4.2. Engine Optimization

Engine optimization is carried out by performing parametric DOE study with the key parameters. A sensitivity analysis is conducted for performance metrics versus the key engine variable, and the multi-objective optimization features of GT-Suite® is also used for optimization.

The key parameters that are optimized for this study are

- Injection timing
- Injection pressure
- Air-fuel ratio (AFR)
- Compression ratio (CR)
- Boost pressure

Constraints are also defined for the model including the peak in-cylinder pressure as 150 bar and maximum pressure rise rate (MPRR) as 10 bar/deg, that will help to eliminate the set of parameters leading to unrealistic engine behavior.

Diesel engine performance is determined mainly by BSFC and BSNOx based on the scope of this thesis and considering upcoming NOx emission standards. The objective of the optimization is minimizing BSFC and BSNOx. However, there is always a trade-off between those two parameters. So, optimization of these two parameters is challenging.

For optimization procedure, the turbocharger is replaced by components that maintain intake boost pressure constant as turbocharger performance varies at each condition. The optimization process is breakdown into multiple steps as there are many decisive parameters.

4.2.1. The Effect of Sweeping AFR, Injection Pressure and Injection Timing at Different CR (Step-1)

Effect of the four key parameters is studied for optimization in Step 1 with constant boost pressure 1.75 bar for engine running at 2000 RPM with 35 kW load. AFR is controlled to the target value using a Proportional-Integral (PI) controller for the EGR throttle position. Gains for the PI controller is calibrated using simple analytic rules based on Skogestad method [84]. The target AFR value is attained by changing the EGR throttle position via the PI controller.

Multi-objective optimization is carried out using three design variables; AFR, injection timing, and injection pressure at compression ratios of 17 and 18. The range of design variables is defined according to Table 4.2.

Table 4.2: List of design variable for optimization

Design Variable	**Variable range**
Injection timing [CA deg. ATDC]	[-6,-5,....,9,10]
Injection pressure [bar]	[800,1000,...,1800,2000]
AFR [-]	[19,19.5,...,27.5, 28]
CR [-]	[17,18]

Estimated relative sensitivity of the design variable provided by GT-Suite® is utilized for the optimization study. Estimated relative sensitivity is computed assuming the relationship between the factors and response is linear, and the sensitivity values that are reported are based on standardized regression coefficients which ignore the variables of the scale unit. Each factor and each response are standardized by subtracting the mean and dividing by the sample standard deviation, and linear regression is performed on each response. A 3-factor standardized linear regression Equation defined in the GT-Suite® optimization manual [85] is given by:

$$Y' = b_1' x_1' + b_2' x_2' + b_3' x_3' + e' \quad (4\text{-}1)$$

where, $x_i' = (x_i * \hat{\mu}_{x_i})/s_i$ represent standardized factors and

$b_i' = b_i * \frac{s_{x_i}}{s_y}$ are standardized regression coefficients, and

$Y' = (Y * \hat{\mu}_Y)/s_y$ represents the standardized response (predicted value of Y in z scores)

e' is the error term

Sensitivity is determined by:

$$S_i = \frac{|b_i'|}{\sum b_i} \quad (4\text{-}2)$$

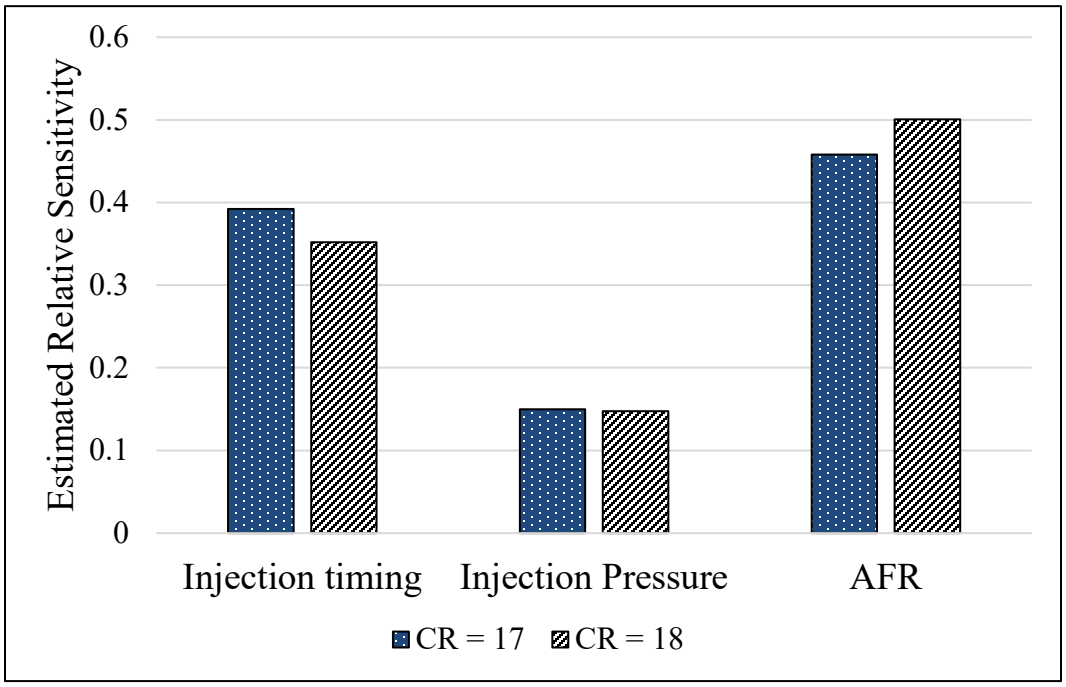

Figure 4.2: Sensitivity comparison of BSFC for injection timing, injection pressure and AFR at CR of 17 and 18

Estimated relative sensitivity of three factors at a compression ratio of 17 and 18 on BSFC and BSNOx is auto-generated by GT multi-objective optimizer tool using standardized linear regression method, presented in Figure 4.2 and Figure 4.3.

Figure 4.2 demonstrates the estimated sensitivity of the design variables on BSFC at compression ratios of 17 and 18. AFR has higher sensitivity for BSFC, injection timing lies in between the other two, and injection pressure has the least sensitivity value. However, as the compression ratio is raised, the AFR sensitivity value is increasing, and the injection timing sensitivity value is decreasing for BSFC. Injection pressure sensitivity is almost constant for the two different compression ratios.

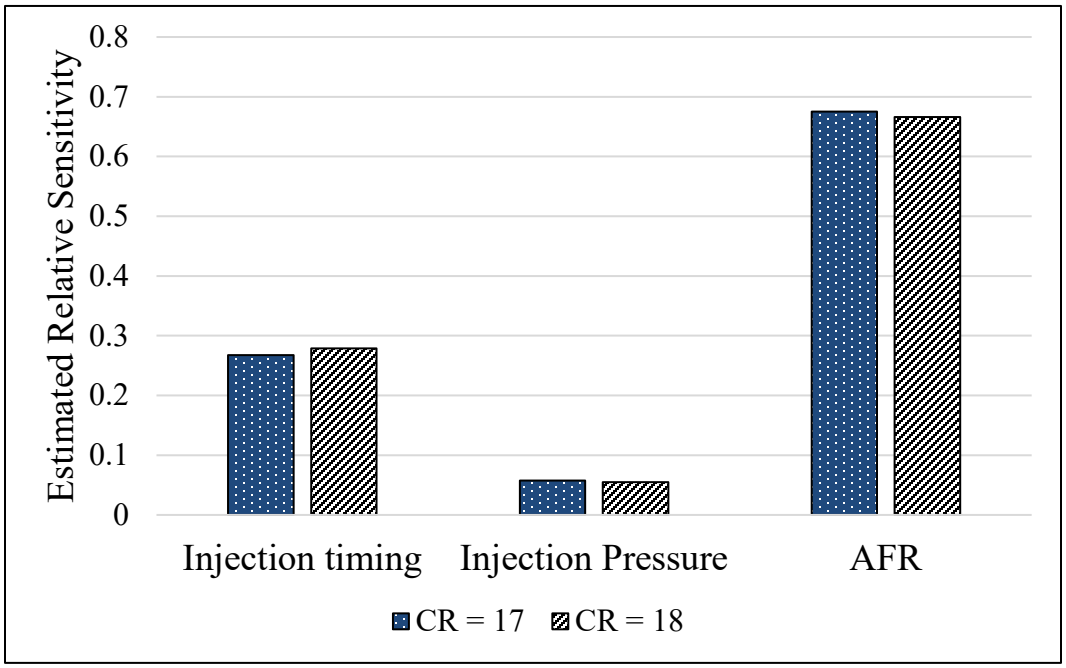

Figure 4.3: Sensitivity comparison of BSNOx

Air fuel ratio has a dominant effect on BSNOx with estimated sensitivity values of 0.7, and the injection pressure effect is the least with estimated sensitivity below 0.075, as seen in Figure 4.3. Injection timing has estimated sensitivity of 0.26 for BSNOx, and it can be noticed that sensitivity change is negligible at different compression ratios. From these

results, it can be concluded that injection pressure has the least effect on BSFC and BSNOx while AFR is having a significant impact. Individual design variables were swept, keeping other variables constant at compression ratios of 17 and 18 to understand the change in the magnitude of BSFC and BSNOx in detail for each parameter.

4.2.1.1. Effect of Changing Injection Timing

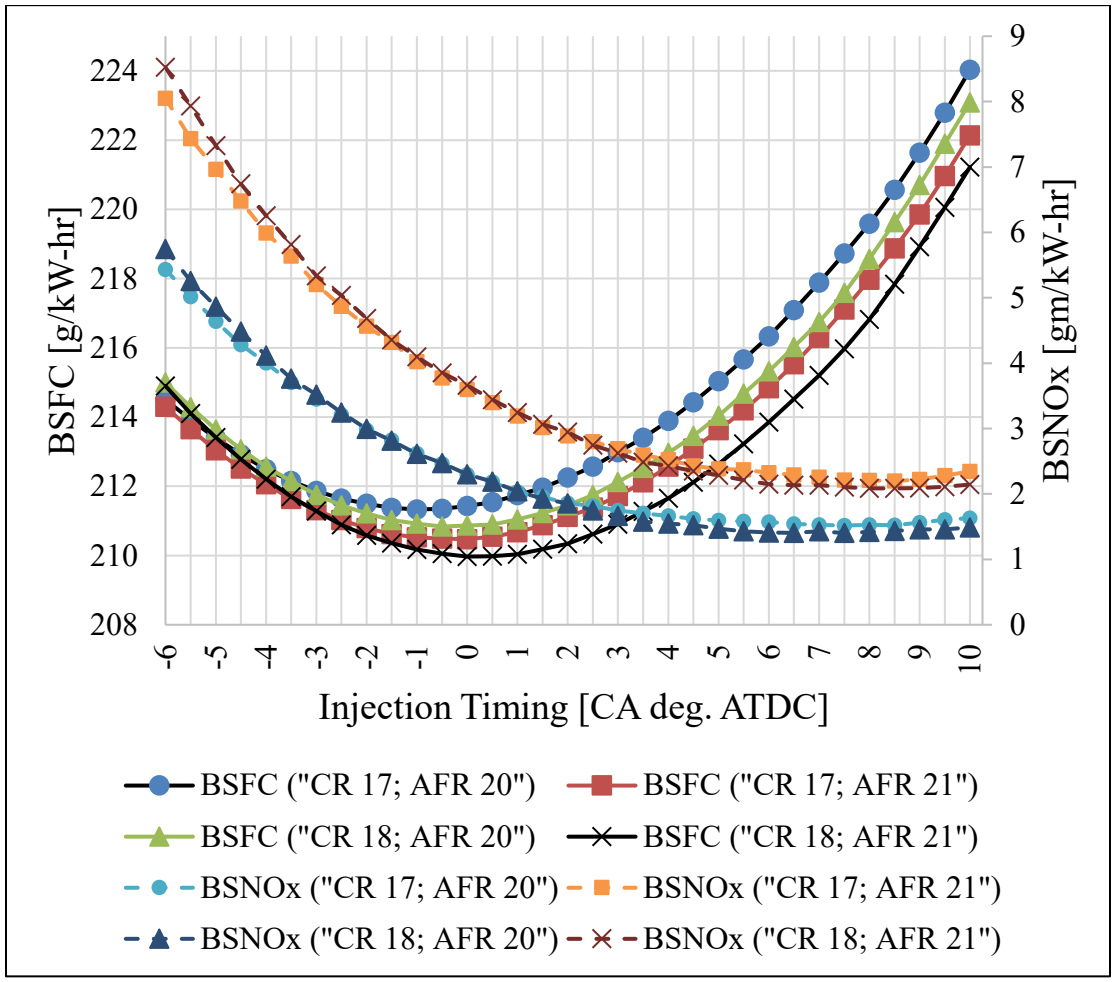

Figure 4.4: Effect of changing injection timing on BSFC and BSNOx

Injection timing is swept from -6 CA deg. ATDC to 10 CA deg. ATDC with a step size of 0.5 at a constant injection pressure of 1400 bar. Two sets of AFR and CR are utilized to

have a better understanding of injection timing change. Figure 4.4 shows the effect of changing injection timing at constant injection pressure, compression ratio, and AFR on BSFC and BSNOx. BSFC is optimum at a specific timing, and there is a penalty in BSFC for retarding or advancing injection timing from that optimum timing. BSNOx is declining as injection timing is retarded because of drop in peak cylinder pressure and temperature shown in Figure 4.5.

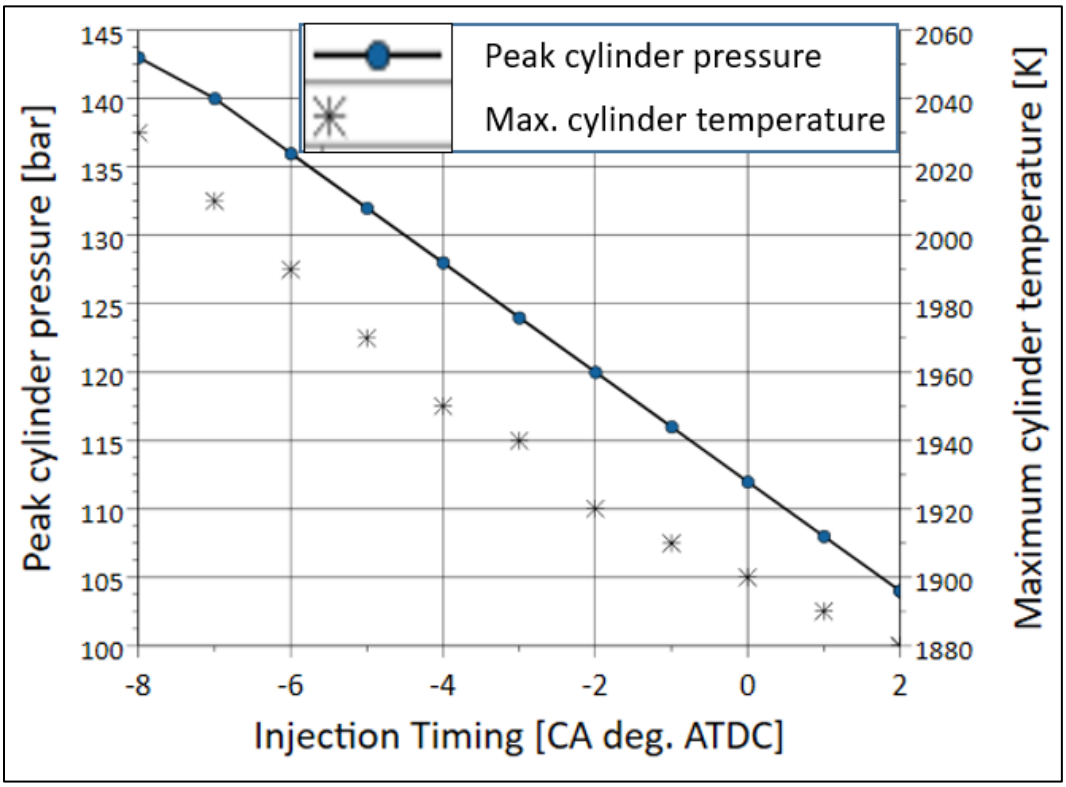

Figure 4.5: Effect of changing injection timing on peak cylinder temperature and pressure

4.2.1.2. Effect of Changing AFR

As seen from the estimated sensitivity chart, BSFC and BSNOx are highly sensitive to change in air-fuel ratio. Effect on BSFC and BSNOx can be seen in Figure 4.6. When AFR is swept from 19 to 28, keeping injection timing and injection pressure constant at 2 CA deg. ATDC and 1400 bar respectively for compression ratios of 17 and 18, BSFC declines

at a much higher rate as AFR is increasing while BSNOx is rising with increasing AFR. Increase in AFR elevates O_2 concentration for combustion that leads to rising in NOx formation. The effect of AFR is prominent on both BSFC and BSNOx as an increase in AFR drastically uplifts O_2 concentration in the air-charge mixture that boost the combustion rate leading to higher pressure and temperature inside the cylinder, a condition favorable for NOx formation.

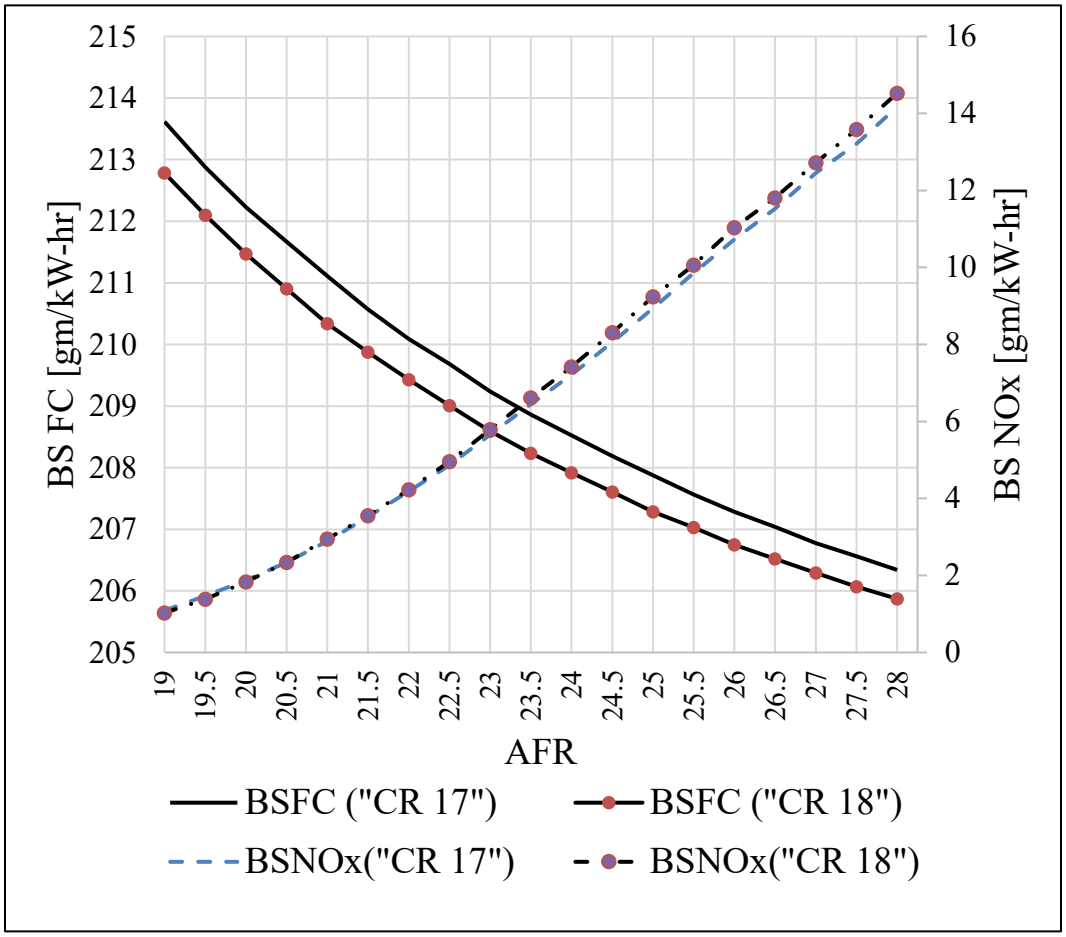

Figure 4.6: Effect of changing AFR on BSFC and BSNOx

4.2.1.3. Effect of Changing Injection Pressure

Effect of sweeping injection pressure on BSFC and BSNOx at constant injection timing and AFR can be observed in Figure 4.7 for compression ratios of 17 and 18. BSNOx increases and BSFC reduces as injection pressure rises because combustion duration is short, and most of the energy is released at the initial phase of injection, leading to higher pressure and temperature.

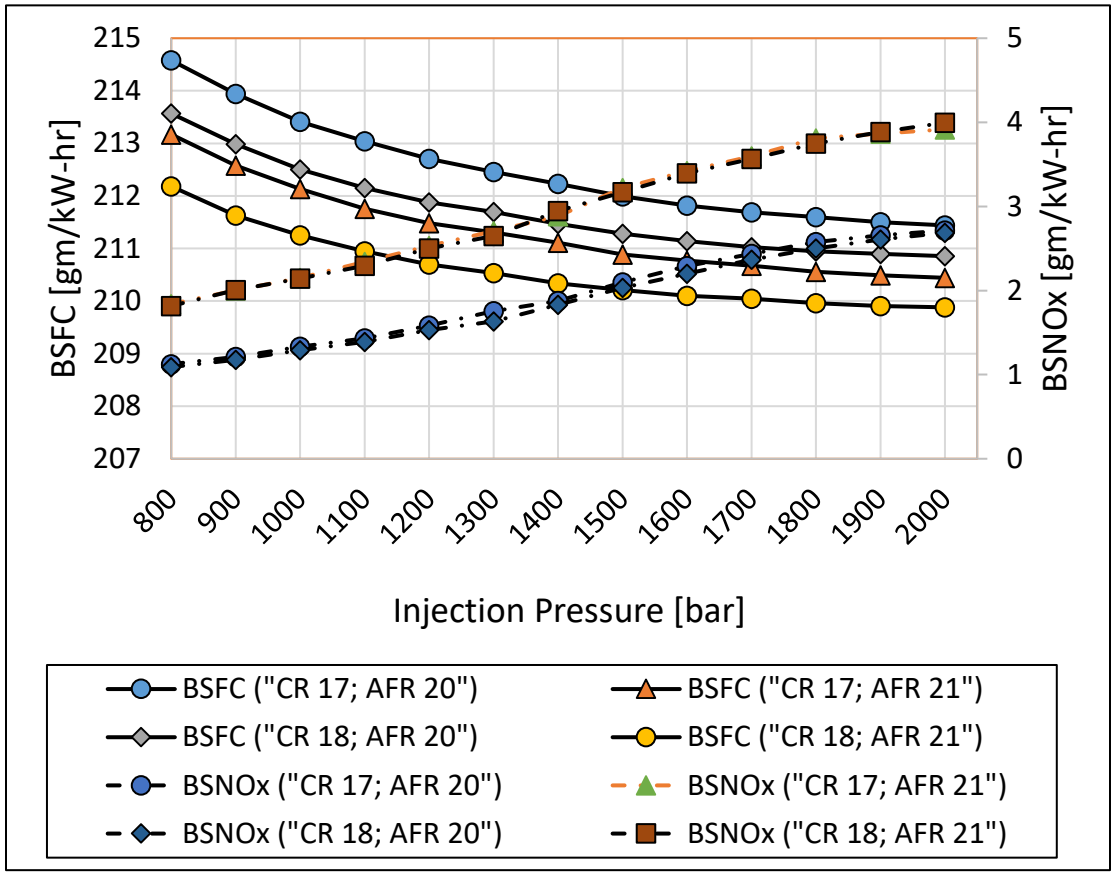

Figure 4.7: Effect of changing injection pressure on BSFC and BSNOx

Injection pressure has the least effect on BSFC and BSNOx however it has a significant impact on hydrocarbon and soot emission as well as the maximum pressure rise rate responsible for the increase in the coefficient of variation of indicated mean effective

pressure [86]. So, injection pressure must be chosen with respect to BSNOx emission and BS soot emission. It can be perceived from Figure 4.8 that brake specific soot emission is significantly higher for lower injection pressure and attains constant value after reaching injection pressure around 1400 bar. So, for further optimization, an injection pressure of 1400 bar is used which minimizes BS soot and HC emission penalizing BSNOx emission least.

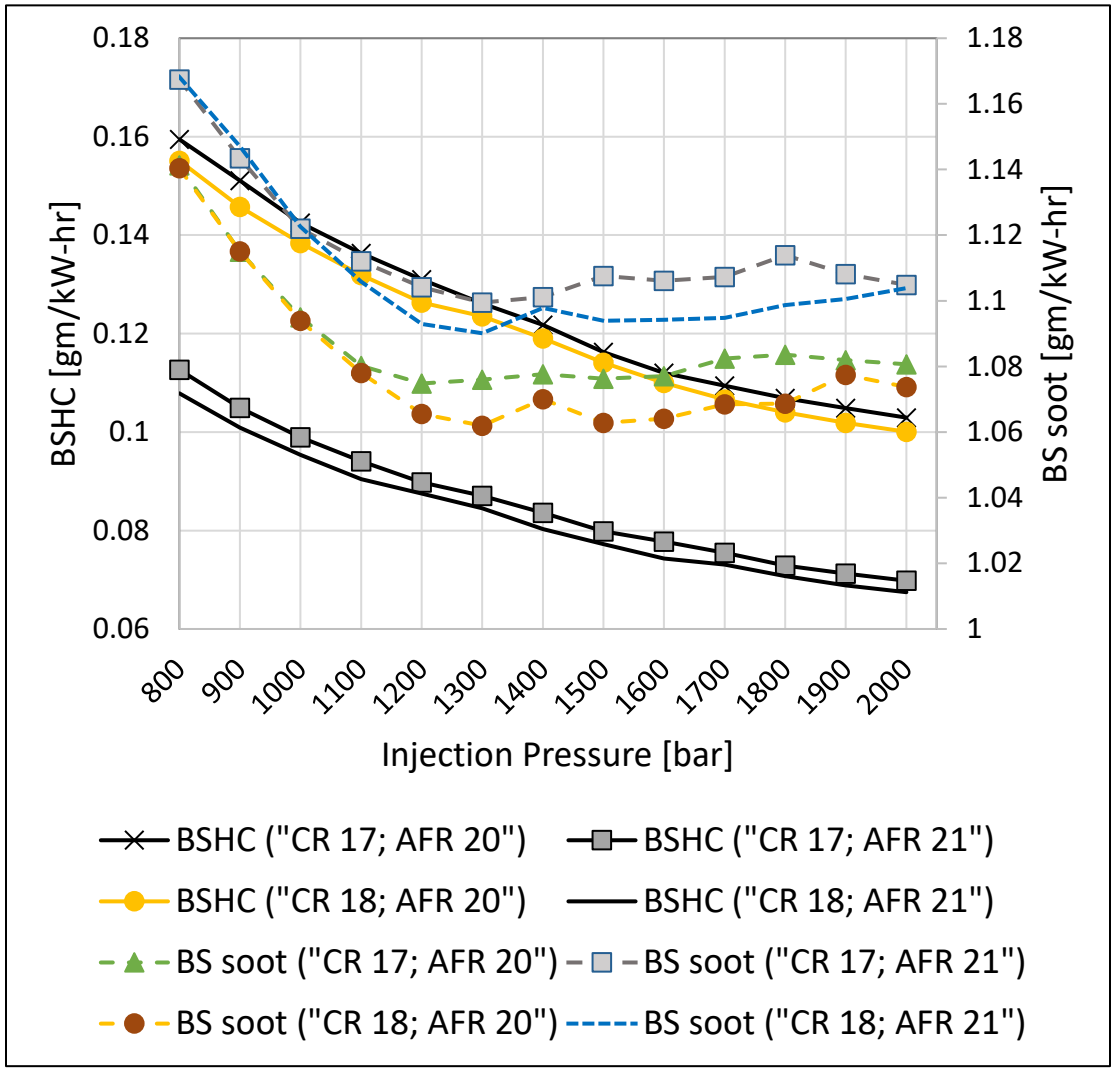

Figure 4.8: Effect of injection pressure change in soot and unburned hydrocarbon emissions

Injection pressure of 1400 bar is selected as the optimum injection pressure from Step 1. As AFR significantly affects BSFC and BSNOx, for further optimization steps, Iso-NOx optimization is used that targets BSNOx to a fixed value using a PI controller. The gain values of PI controllers are adjusted that will target BSNOx to the desired value. BSNOx of 4 gm/kW-hr and 3 gm/kW-hr are used for all operating point. The reason to choose these two values is based on the assumption that BSFC penalty is not high at those operating points and after-treatment conversion efficiency is generally about 90% after reaching catalyst light-off temperature that would meet NOx emission target of 0.4 gm/kW-hr.

4.2.2. Optimization of Injection Timing, Boost Pressure and CR (Step-2)

In the second step of optimization, the injection pressure is kept constant at 1400 bar, and design variables are injection timing, boost pressure and compression ratio are optimized for best BSFC at BSNOX of 4gm/kW-hr and 3 gm/kW-hr. Exhaust gas temperature (EGT) plays a vital role in determining the performance of after-treatment components. So, in this step, the design variables are optimized for optimum BSFC and EGT. Like BSFC and BSNOx trade-off, BSFC and EGT also show similar behavior, i.e., increasing in EGT has a negative effect on BSFC. Increase in exhaust temperature could be achieved by decreasing compression ratio, retarding injection timing, and decreasing boost pressure, but those changes impose a negative impact on BSFC. EGT must be maintained in the desired range between 300^0 C and 500^0 C while optimizing BSFC for better conversion efficiency and to meet emission regulation.

EGT has a significant impact on the conversion efficiency of the exhaust after-treatment component, so the turbine inlet temperature is also monitored while optimizing BSFC. Performance of after-treatment is mainly determined by DPF and SCR. Based on the literature review it is found that SCR with Fe-zeolite catalyst has better efficiency for temperature above 350^0 C. At these temperatures, passive regeneration in DPF is also regularly occurring that burns soot accumulated in the filter. So, in this step, BSFC is

optimized for an operating point that would result in exhaust gas temperature at the inlet of the after-treatment system around 400^0 C considering heat losses in after-treatment components.

Compression ratio and injection pressure are swept at three boost pressure 1.55 bar, 1.65 bar and 1.75 bar at constant injection pressure and targeting BSNOx to 4gm/kW-hr and 3gm/kW-hr for all cases.

Table 4.3: Design variable for optimization

Design variable	**Variable Range**
Compression ratio [-]	[16,17,...,22,23]
Injection timing [CA. deg ATDC]	[-6,-5,....,9,10]
Boost pressure [bar]	[1.55,1.65,1.75]

From the results in Figure 4.9, Figure 4.10, Figure 4.11, and Figure 4.12, it can be seen that increase in compression ratio and boost pressure improves BSFC but reduces exhaust gas temperature while injection timing has the optimum BSFC at a specific injection timing. EGT and BSFC significantly increase at retarded injection timing, which is mostly due to late combustion and incomplete combustion of fuel.

The effect of EGT has been realized from the literature review. If EGT is high, urea-SCR NOx conversion efficiency decreases due to oxidation of NH_3 on the catalyst surface, increasing urea consumption. For DPF soot regeneration, high temperature is favorable, but at low-temperature soot accumulation in the filter is very high that increases back pressure and affect the engine efficiency. This comparison has been made by considering the EGT downstream of the turbine and its corresponding after-treatment efficiency.

From the available results, the optimum engine operating point is chosen at injection timing 2 deg. CA ATDC, CR of 18 and boost pressure of 1.65 bar that results in BSFC of 210

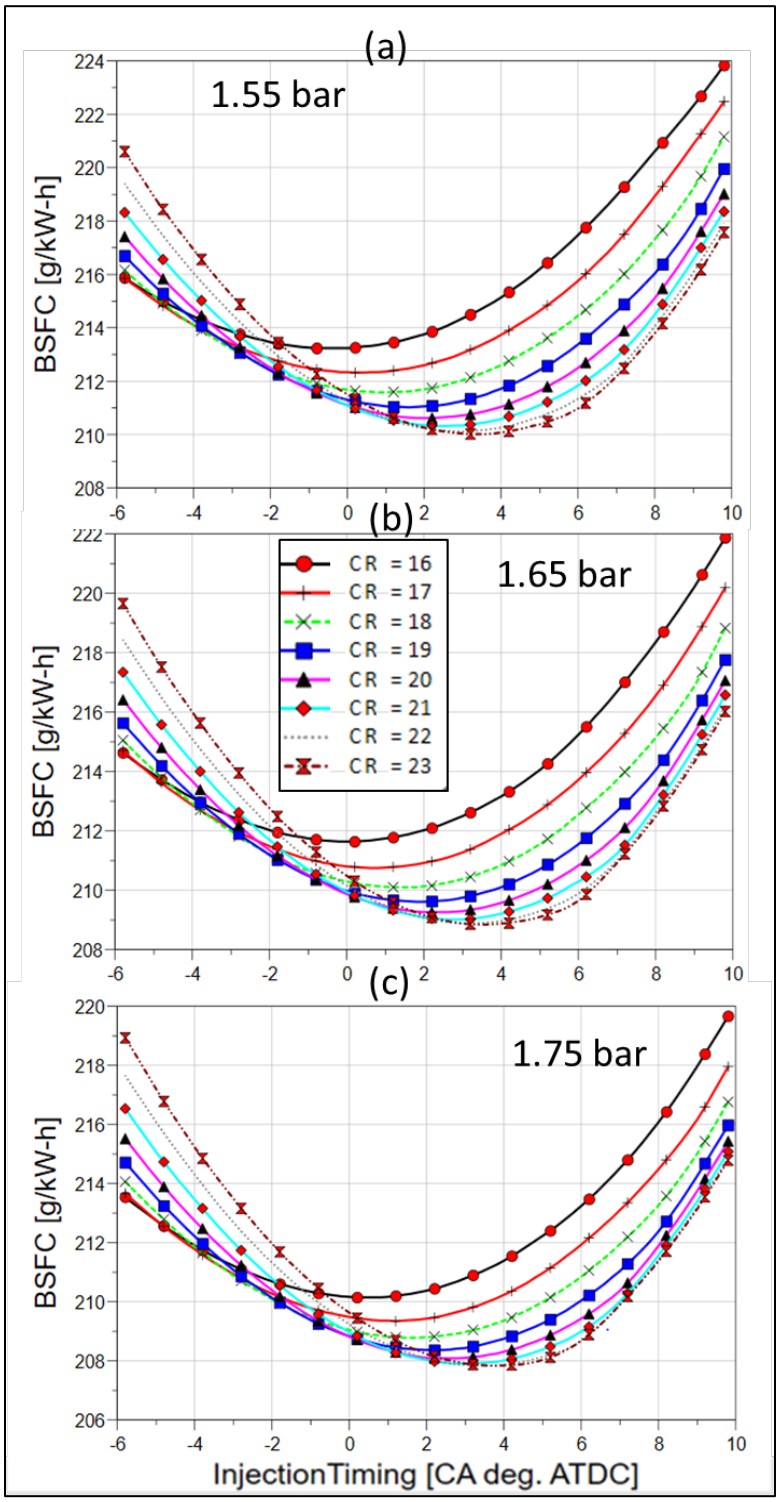

Figure 4.9: Comparison of BSFC at different boost pressures at BSNOx 4 gm/kW-hr

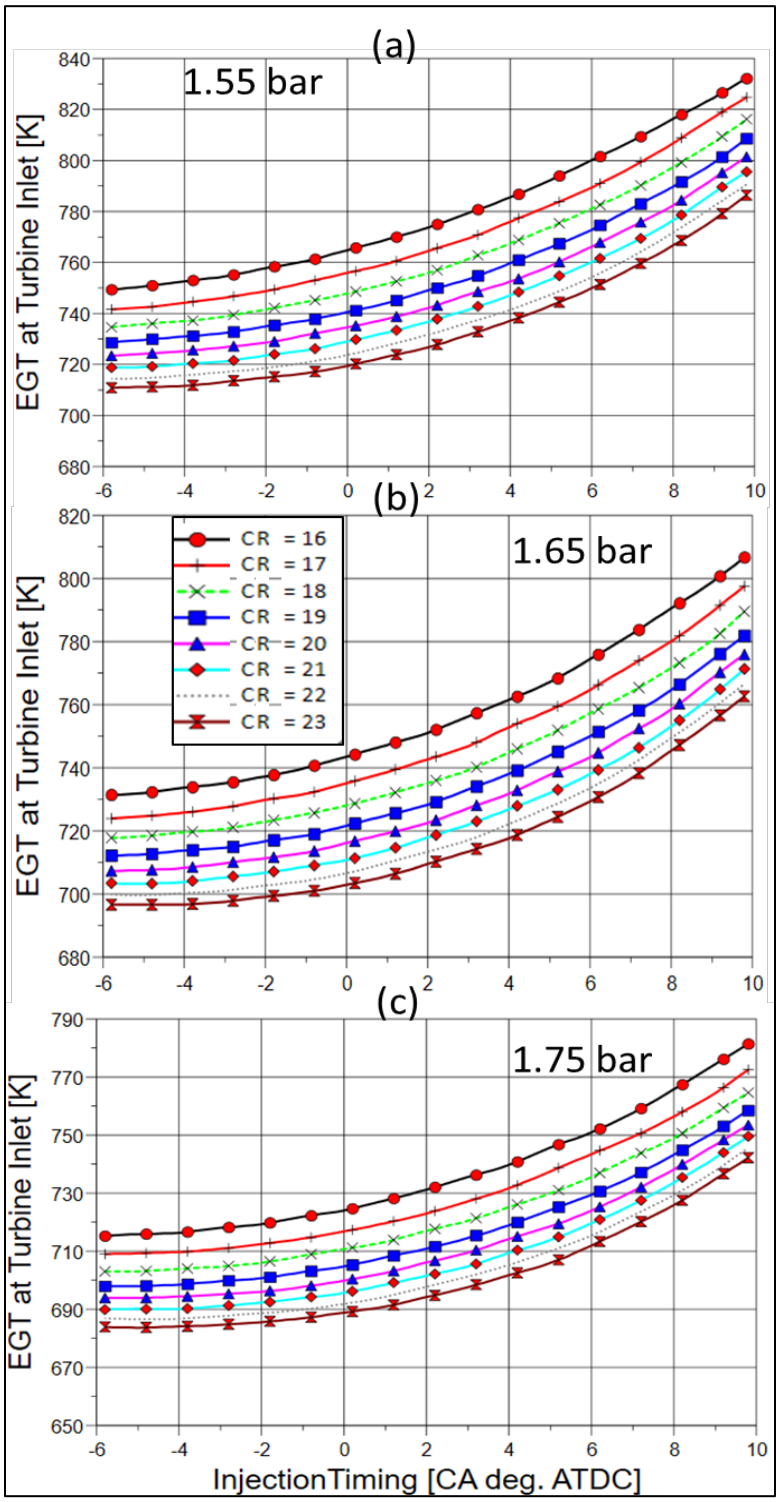

Figure 4.10: Comparison of EGT at different boost pressures at BSNOx 4gm/kW-hr

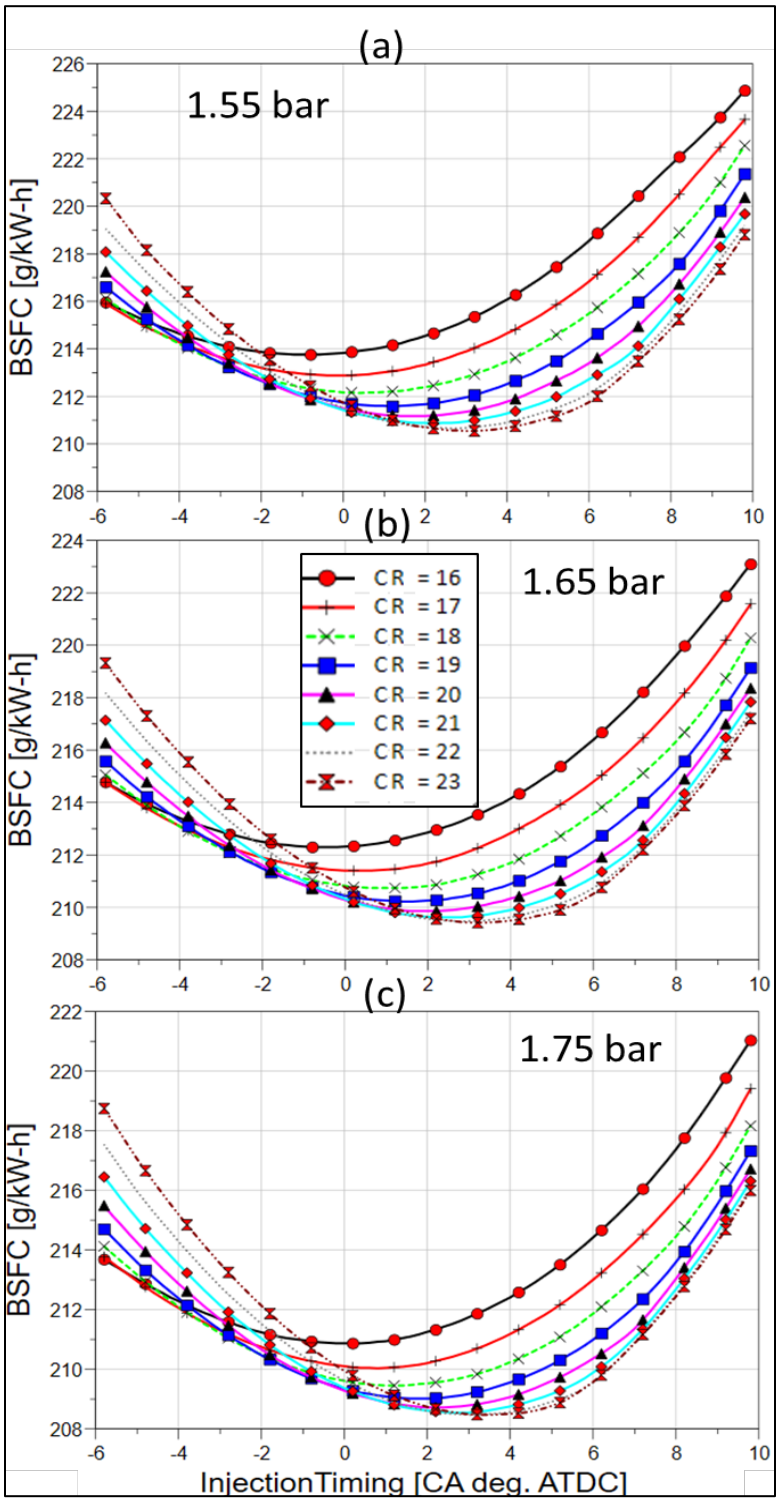

Figure 4.11: Comparison of BSFC at different boost pressures at BSNOx 3gm/kW-hr

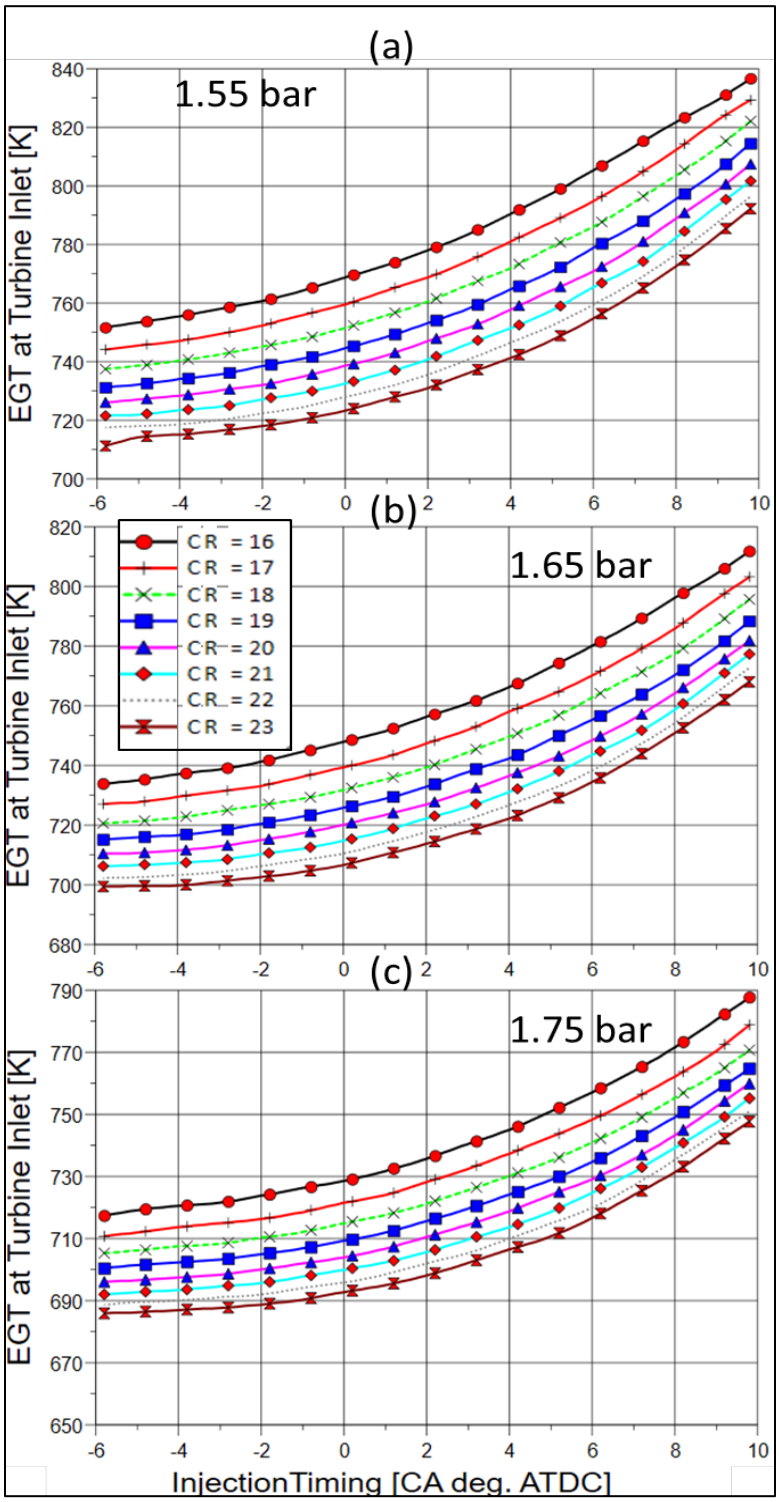

Figure 4.12: Comparison of EGT at different boost pressures at BSNOx 3gm/kW-hr

gm/kW-hr and EGT at turbine inlet 735 K (462^0 C) at BSNOx 4gm/kW-hr. There is not a significant penalty in BSFC for an increase in EGT at that point, which can be noticed in Figure 4.9. Similarly, for BSNOx 3gm/kW-hr case, the optimum operating point is chosen for the same CR and boost pressure at injection timing around 1.5 deg. CA ATDC that would result in BSFC of 211 gm/kW-hr and 738 K (465^0 C) EGT at the turbine inlet.

Since a bigger step size of design variables was utilized to acquire result, further optimization is done using the GT-power multi-objective optimizer to optimize the best engine operating point for a series hybrid forklift application. Genetic Algorithm is used in the multi-objective optimizer with a population size of 10 and number of generations 15 recommended in GT-Suite® manual for two variables. Injection timing and boost pressure were varied for optimization with constant pressure ratio, injection pressure, and BSNOx values. CR is fixed at 18 as EGT can be improved without much penalty in BSFC, which can be realized from Figure 4.9 and Figure 4.11. The design variables, objective function, and constraints defined for optimization are tabulated in Table 4.4.

Table 4.4: Optimization variable, constraints and objective function

<table>
<tr><th colspan="2">Design variables</th><th colspan="2">Constraints</th><th>Objective function</th></tr>
<tr><td>Boost pressure (bar)</td><td>[1.5,2.2]</td><td rowspan="2">EGT (^{0} C)</td><td rowspan="2">[457,497]</td><td>Minimize BSFC</td></tr>
<tr><td>Injection timing (CA deg. ATDC)</td><td>[-5, 10]</td><td>Maximize EGT</td></tr>
</table>

Summary of engine performance for an optimum result is tabulated in Table 4.5. The operating point at BSNOx 4gm/kW-hr provides slightly better fuel efficiency than the operating point at BSNOx 3gm/kW-hr without a significant change in EGT at the turbine inlet. Thus, BSNOx 4gm/kW-hr is chosen as the optimum operating point considering

emission requirements would be met. For that operating point, CA50 is 10.5 CA deg. ATDC, MPRR is 7.2 bar/deg, and in-cylinder maximum pressure is 113 bar, which is within the acceptable range for this lift truck application.

Table 4.5**:** Summary of optimal engine operating point

Case	**BSNOx 4 g/kW-hr**	**BSNOx 3 g/kW-hr**
Boost pressure (bar)	1.66	1.66
CR	18	18
Exhaust manifold pressure (bar)	1.76	1.77
Injection timing (deg. CA ATDC)	2.05	1.5
Injection pressure (bar)	1400	1400
Injected fuel mass (mg/cycle/cylinder)	30.6	30.66
EGR valve throttle angle (deg)	42.92	56.22
BSFC (g/kW-hr)	209.88	210.31
CA 50 (CA deg. ATDC)	10.49	10.05
EGR (%)	18.66	21.23
AFR (%)	20.65	19.77
MPRR (bar/deg)	7.24	7.09
Max in cylinder pressure (bar)	113.03	113.42
Turbine inlet temperature (^{0}C)	460	464

4.2.3. Calibration of Turbocharger (Step-3)

A turbocharger is added into the model, and calibrated to replicate the boost pressure and pressure ratio. Since the engine is only operated at a single point, a fixed geometry turbine is used. The compressor is connected to a turbine via a shaft that provides enough boost

using the power derived from the turbine. Turbine and compressor efficiency are calibrated to give the same boost pressure in intake components and maintain similar pressure ratio. The calibrated value for a fixed geometry turbocharger is provided in Table 4.6.

Table 4.6: Turbocharger calibration

Turbocharger parameter	**BSNOx 4 gm/kW-hr**	**BSNOx 3 gm/kW-hr**
Turbine orifice diameter [mm]	35	35
Mass flow multiplier [-]	0.182	0.177
Turbine efficiency [%]	70	70
Compressor efficiency [%]	65	65

4.3. Optimal Sizing of After-treatment Components

After-treatment components including DOC, DPF, and SCR are sized that will meet the future emission standards for a non-road diesel engine. For after-treatment components sizing, only length of catalyst is changed. The remaining geometry is kept constant so that the calibrated reaction rate available in GT-Suite® model can accurately predict the reaction mechanism inside the catalyst. BSNOx of 4gm/kW-hr provides a slight advantage in fuel consumption as seen from the optimization results in Table 4.5 compared to 3gm/kW-hr BSNOx, while EGT doesn't deviate much. Therefore, the operating point with BSNOx 4gm/kW-hr is chosen. The mass flow rate, EGT, and composition of exhaust gases acquired for the steady-state at that operating point are utilized for after-treatment sizing. The engine operating point with 3gm/kW-hr BSNOx could be used if the emission limits cannot be met. Performance of the after-treatment component varies with all these parameters, so constant feeding of exhaust gases is used for sizing components.

4.3.1. Performance of DOC

DOC efficiency is determined by the conversion of CO, HC, and NO. NO conversion is vital as this significantly affects passive soot regeneration by NO_2 in DPF and NOx conversion efficiency in SCR. The catalyst temperature can be directly correlated with EGT as increasing EGT increases the heat transfer rate from the exhaust gases to that catalyst substrate. Therefore, the effect of changing EGT for different length of DOC is studied, which is presented in Figure 4.13. CO conversion efficiency is almost 100% at steady-state for EGT more than 250^0 C and is not much affected by catalyst length. However, HC conversion and NO conversion efficiency are dependent on both catalyst length and EGT.

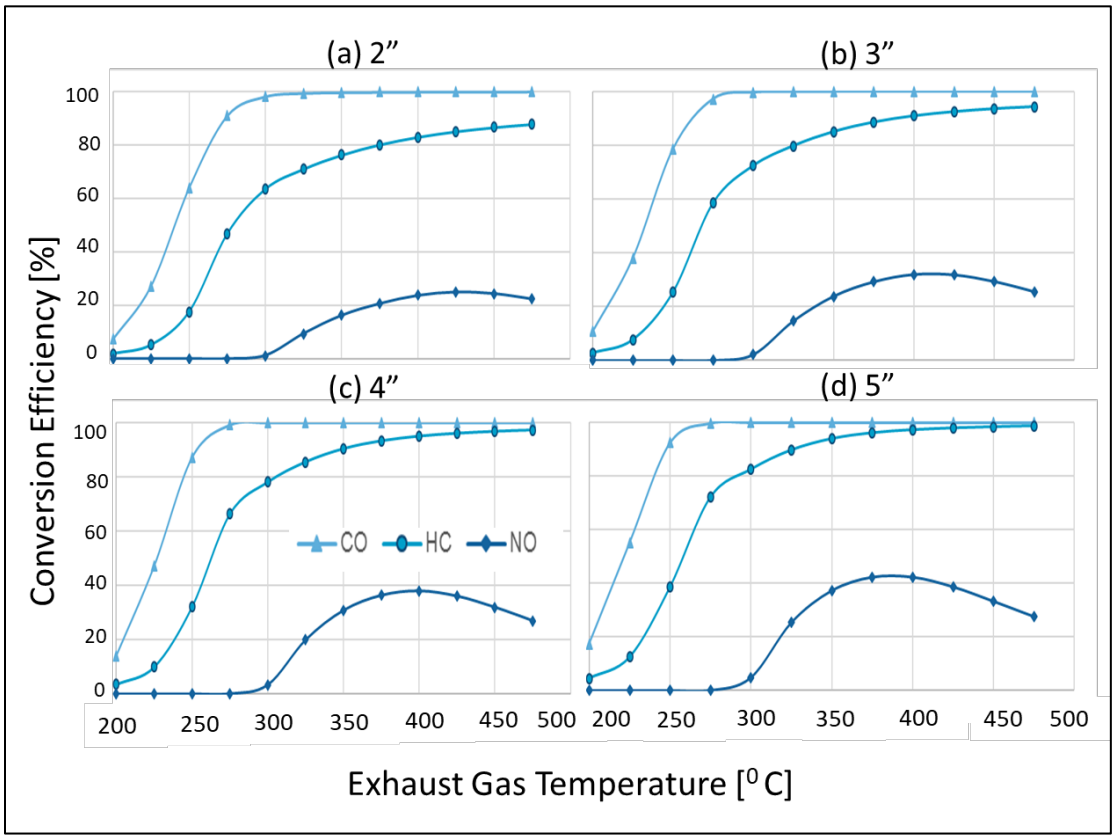

Figure 4.13: Effect of changing DOC catalyst length

NO conversion efficiency is higher at a specific temperature, and it decreases as temperature increases due to the decomposition of NO_2. HC conversion, on the other hand, rises as temperature and length of catalyst increases. From Figure 4.13, the effect of changing exhaust gas temperature for different DOC catalyst length is illustrated. It can be observed that conversion efficiency of around 90% can be achieved for HC and 30% for NO with the catalyst length of 3" .This is a reasonable NOx conversion efficiency value as catalyzed DPF is used downstream of DOC and DPF is sized to target NO_2/NOx ratio close to 0.5 for better NOx conversion in the SCR.

4.3.2. Catalyzed DPF Performance

In this study, only passive regeneration of soot is considered as active regeneration is not included for the non-road engine emission test. An extra amount of fuel is injected using late post injections or additional fuel injector before DOC for the active regeneration process so that unburned fuel enters DOC. This unburned fuel oxidized in DOC increases EGT due to the exothermic reactions before reaching DPF for soot regeneration. For passive soot regeneration, NO_2 plays a vital role in the oxidation of soot in DPF. NO_2 formed in DOC is utilized for passive soot regeneration, but DPF is also self-catalyzed with PGM which again oxidizes NO to NO_2. NO_2/NOx ratio at DPF downstream affects NOx conversion efficiency by Fe-zeolite catalyst, so the length of catalyzed DPF is chosen in a way such that NO_2/NOx is close to 0.5 at DPF downstream for better NOx conversion efficiency [44].

From Figure 4.14, it can be observed that extending catalyst length increases NO_2/NOx ratio as a catalyst active site for the oxidation of NO to NO_2 increases. The pressure drop across DPF reduced drastically when catalyst length increases from 4" to 6'' but significant changes are not observed thereafter. Pressure drop is caused by deposition of soot mass on wall and catalyst brick that blocks exhaust gas flow. Increase in NO_2 concentration also raises urea consumption [34], so DPF length is chosen to target NO_2/NOx concentration

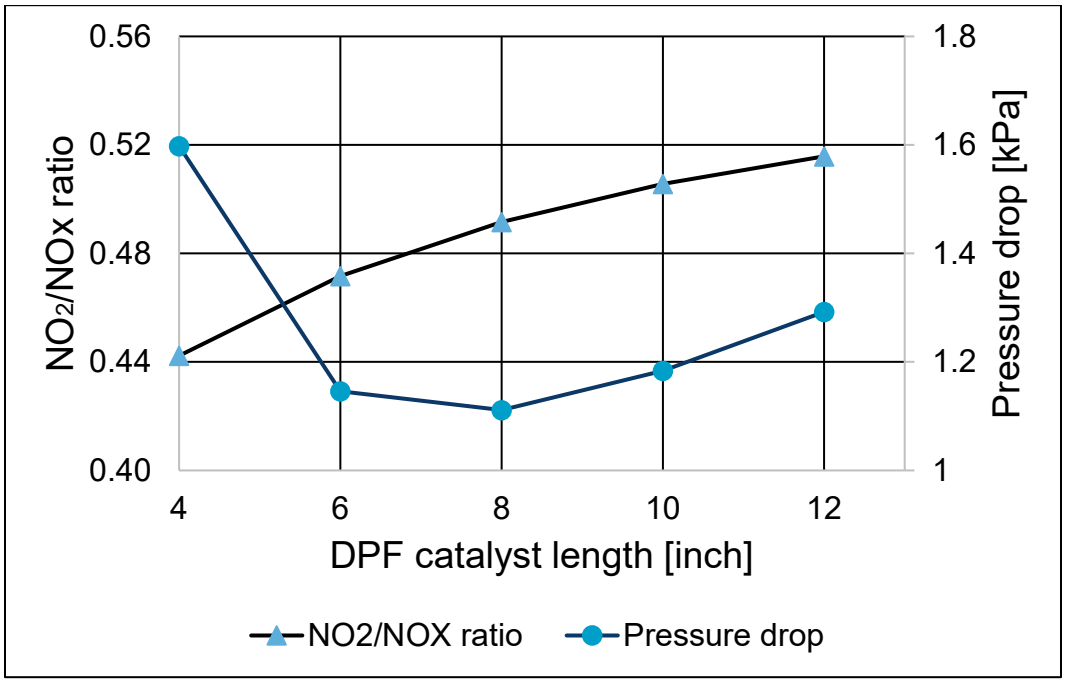

Figure 4.14: Effect of change in DPF catalyst for NO_2/NOx ratio and pressure drop

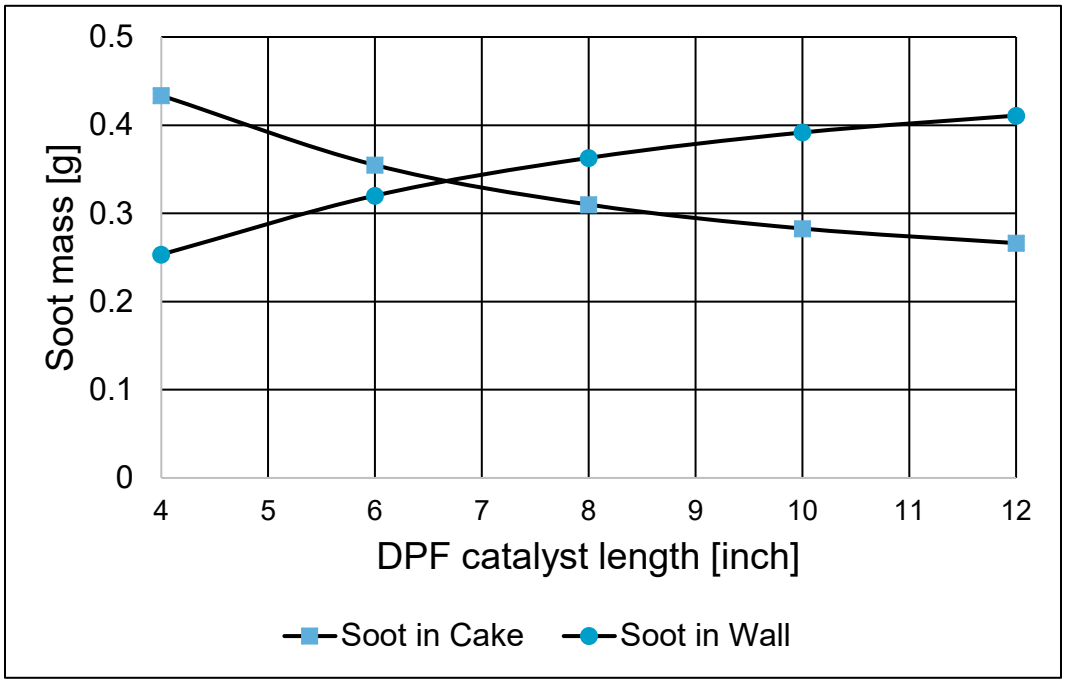

Figure 4.15: Effect of change in DPF catalyst length on the deposition of soot mass

ratio around 0.5. Soot deposition in the wall increases as the length of catalyst is increased, and soot in the cake decreases with increasing DPF catalyst length, as seen in Figure 4.15. This performance in DPF is determined by passive soot regeneration by NO_2.

Particle size distribution at different time instances auto-generated in GT-Suite® is shown in Figure 4.16. The model is defined by providing lower bound and upper bound particle diameter, median particle diameter, and geometric standard deviation that predicts the particle size distribution in the outlet channel. The default setting in GT-Suite® is used to attain particle size distribution at the inlet channel and outlet channel for DPF in the model. The particle size distribution is represented by dN/d(lnD) using a log-normal distribution that assumes soot particles are spherical with a density of 1000 kg/m^3 [71]. The total number of particle concentration can be computed using the following equation [71]:

$$N_0 = \sum_{i=1}^{nbins} f(\ln(D_{i+1}) + \ln(D_i) \quad (4\text{-}3)$$

where,

N_0 is the total particle number

f is y value of distribution plot

D_i is the diameter of the particle

Nbins is number of bins=50

From Equation (4-3) and the data acquired from GT-Suite®, particle number is calculated for different time instances at the inlet and outlet channels of DPF catalytic brick, as shown in Figure 4.17. The inlet particle number is constant, and the particle number at the outlet channel is decreasing as engine operation time increases. As the catalyst is not warmed up, the particle number is higher at 100 seconds, and the particle number count decreases as passive soot regeneration in the catalyst is initiated. The particle count is sufficiently low for this model. Therefore, Euro V emission standard for PN limit, $1*10^{12}$/kW-hr can be met using the catalyst length of 6". NO_2/NOx ratio is also close to 0.5 upstream of SCR for this catalyst, so 6" DPF length is used for further analysis.

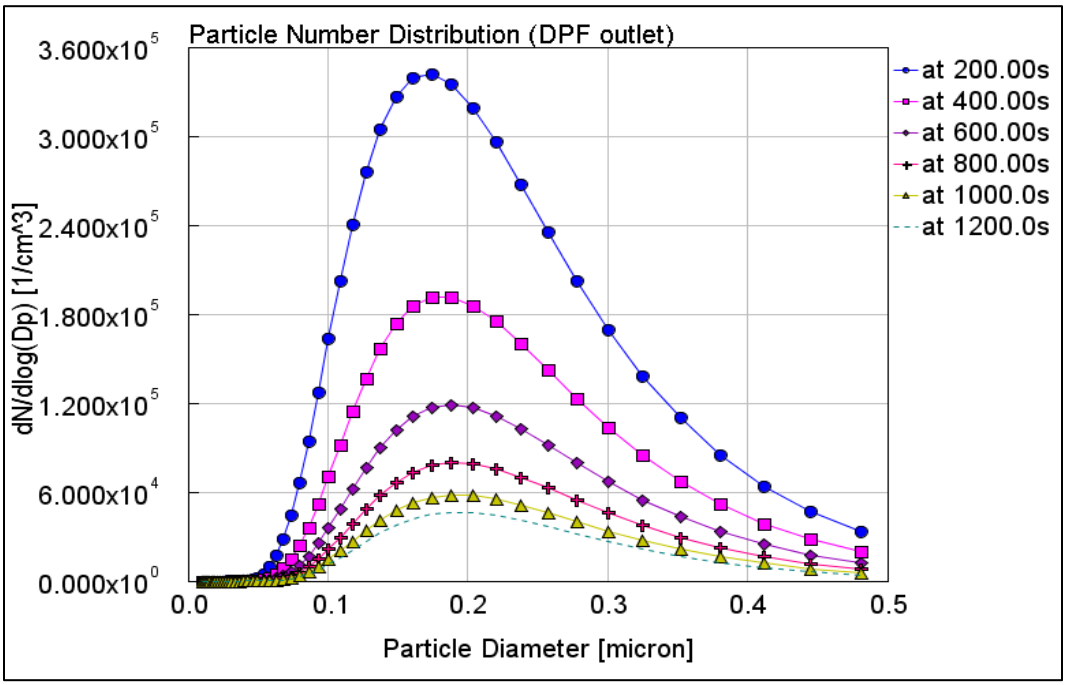

Figure 4.16: Particle size distribution for DPF catalyst length 6"

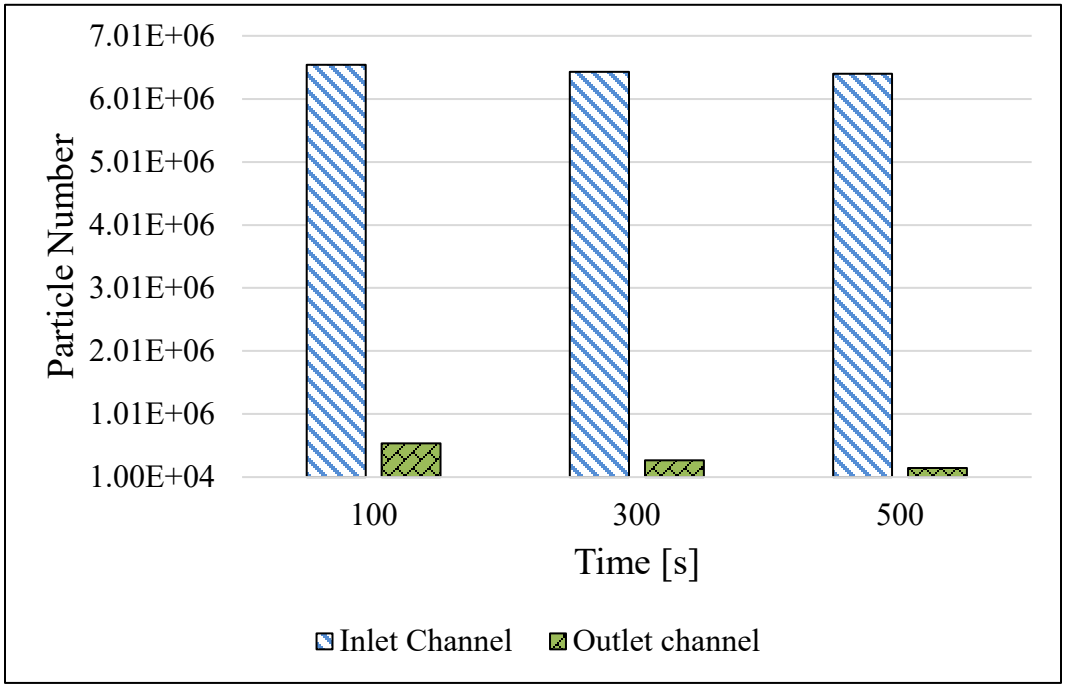

Figure 4.17: Particle Number at DPF inlet and outlet channel

4.3.3. SCR Performance

The urea-SCR model is developed in GT-Suite® with a urea controller that reduces NOx in the presence of a catalyst. Performance of Fe-zeolite is studied along with Cu-Chabazite and two catalysts arranged in series defined in the reference [44]. The performance of these catalysts is shown in Figure 4.18. The steady-state NOx conversion efficiency and the total amount of urea consumption in 300 seconds for three catalysts are plotted in Figure 4.18. NOx conversion for these three catalysts strongly depends on EGT. NOx conversion of Cu-CHA is better for temperature below 350^0 C while conversion efficiency of Fe-zeolite is optimum at a temperature above 350^0 C. In addition, these two catalysts arranged in series with length ratio 33% Fe and 67% Cu based catalyst provides better efficiency for wide temperature range. Since EGT for the optimized engine operating point is just below 400^0 C, Fe-zeolite catalyst will be the most suitable for this engine model. The conversion efficiency of this catalyst is optimum around NO_2:NOx ratio of 0.5. DOC and DPF lengths are chosen in such a way that NO_2/NOx ratio at SCR inlet is around 0.5 for better conversion efficiency. The catalyst performance is also determined by other factors as urea dosing, length of the catalyst which is being studied for optimization. Urea dosing is controlled by SCR catalyst temperature and NH_3 slip at downstream of SCR. The catalyst length is optimized to meet emission standards with minimum urea consumption to reduce operational cost.

Figure 4.18 shows NOx conversion efficiency and urea consumption for fixed-length (4.5”) of SCR catalysts at different EGT. EGT is varied from 200^0 C to 500^0 C for different catalysts. Conversion efficiency is 0% at 200^0 C because NH_3 dosing is initiated only at temperatures above 200^0 C. Conversion efficiency of Cu-zeolite decreases as EGT increases above 350^0 C, but urea consumption is almost constant at a higher temperature. Performance of Fe-zeolite and series arrangement of catalyst is nearly the same at a higher temperature, but urea consumption is slightly higher at a lower temperature for catalyst with the series arrangement. The catalyst with series arrangement would be suited best for

dynamic engine operation, and Cu-CHA catalyst would be suited for smaller engine operating at lower loads.

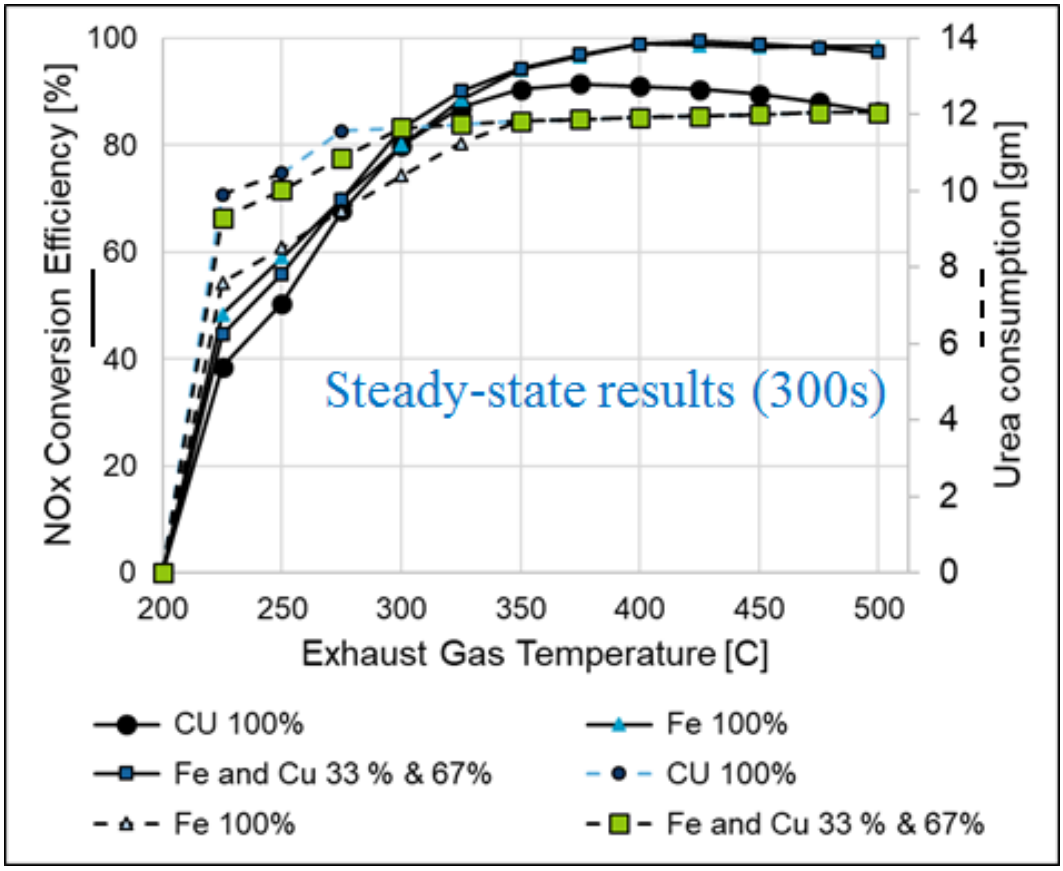

Figure 4.18: Performance of different SCR catalyst (catalyst length:4.5")

Effect of changing Fe-zeolite catalyst length is portrayed in Figure 4.19. It can be noticed that urea consumption and NOx conversion efficiency increase with increasing catalyst length. There is not a significant change in conversion efficiency and urea consumption for increasing catalyst length of more than 4". However, choosing length greater than 4" would result in higher urea consumption if the urea dosing strategy is not adopted. Urea dosing strategy stops dosing when excessive ammonia slips from SCR catalyst, and the dosing

ratio is lower for higher temperature as NH_3 oxidizes itself on catalyst surface without contributing to tail-pipe NOx reduction. As a result, SCR length is chosen as 3.25" that would achieve NOx conversion efficiency more than 90%.

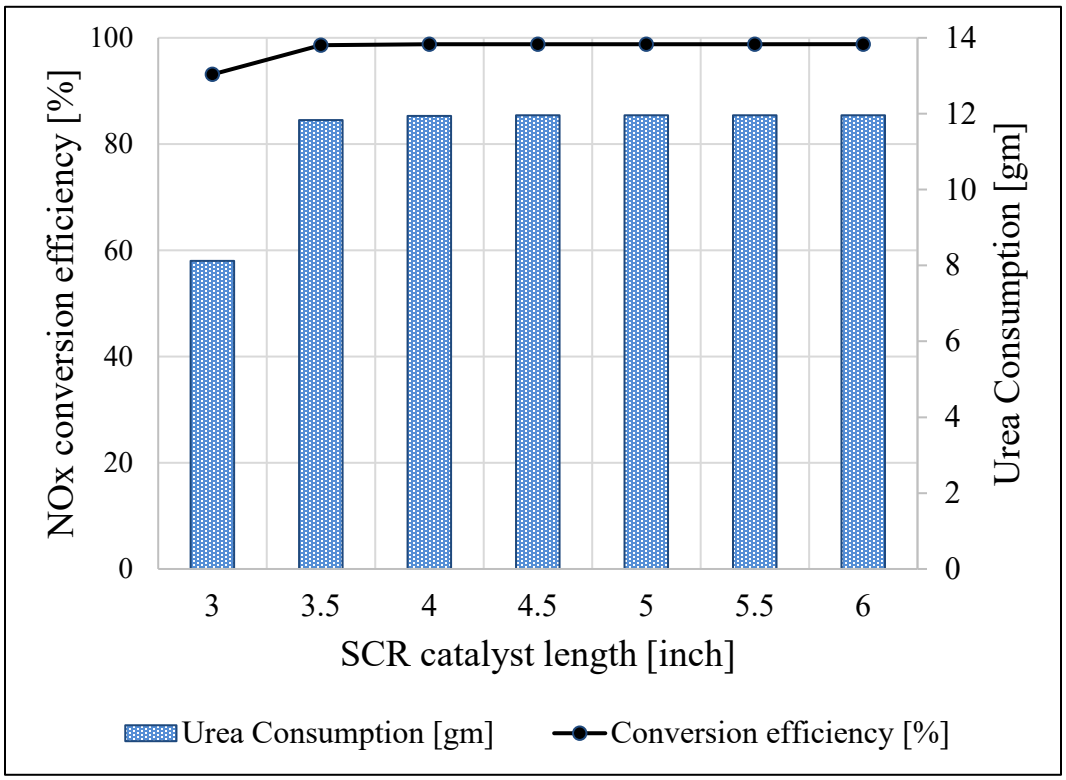

Figure 4.19: Effect of changing SCR catalyst length (Fe-Zeolite catalyst)

As it is clear from the above discussion that NOx conversion by ammonia in SCR is a complex phenomenon determined by many factors like catalyst length, exhaust gas temperature, the composition of exhaust gases, flow rate and nature of catalyst used. This is further affected mainly by the total ratio of NO_2:NOx entering the catalyst. Usually, NO_2 requires more amount of ammonia than NO for reduction and the conversion efficiency in the catalyst is affected by the amount of urea that has been supplied to SCR catalyst brick. The advanced dosing mechanism using a controller for optimum conversion efficiency of NOx with minimum urea consumption is overviewed in the reference [34]. Since the after-treatment system is used for engine operating at a single point, advanced dosing mechanism

is not required, and optimal conversion efficiency can be achieved by dosing ammonia in a certain proportion to NOx entering to SCR. In the Section 4.3.4, the effect of changing NH_3:NOx dosing ratio at different temperatures is studied.

4.3.4. Effect of Changing NH_3:NOx Dosing Ratio for SCR Catalyst

Figure 4.20 shows steady-state NOx conversion efficiency and total urea consumption for urea SCR with Fe-zeolite catalyst in 3600 seconds. The simulation was carried out at a constant feed rate and exhaust gas composition. The length of the catalyst for DOC and DPF used for the simulation are 3" and 6" respectively at an initial catalyst temperature of 25^0 C. EGT and NH_3:NOx dosing ratio is changed for the simulation. NH_3:NOx ratio is determined by sensing the total amount of NOx molar flow rate upstream of SCR catalyst brick, and generally, 1.05 molar ratio is considered sufficient for reduction of NH_3 [44].

NOx conversion is maximum at EGT around 375^0 C, and it decreases beyond that temperature, which is quite the opposite of how it should be for Fe-zeolite catalyst. The reason for reducing NOx efficiency might be the difference in NO and NO_2 fraction at SCR inlet for higher temperatures, as seen in Figure 4.22. These differences in NO and NO_2 fraction are due to NO_2 conversion efficiency characteristics of DOC and DPF. Figure 4.21 shows the effect of temperature on the conversion of NO_2 at DOC. As the temperature increases above 400^0 C, NO_2 conversion efficiency at DOC and DPF decreases. At lower temperature, NO_2 formation in DPF is dominant leading to increase in NO_2 ratio as enough oxygen is present, but as the exhaust temperature rises, active regeneration occurs that utilizes available oxygen for soot regeneration. Active regeneration of soot particles by oxygen decreases the availability of O_2 and increases decomposition of NO_2 at a higher

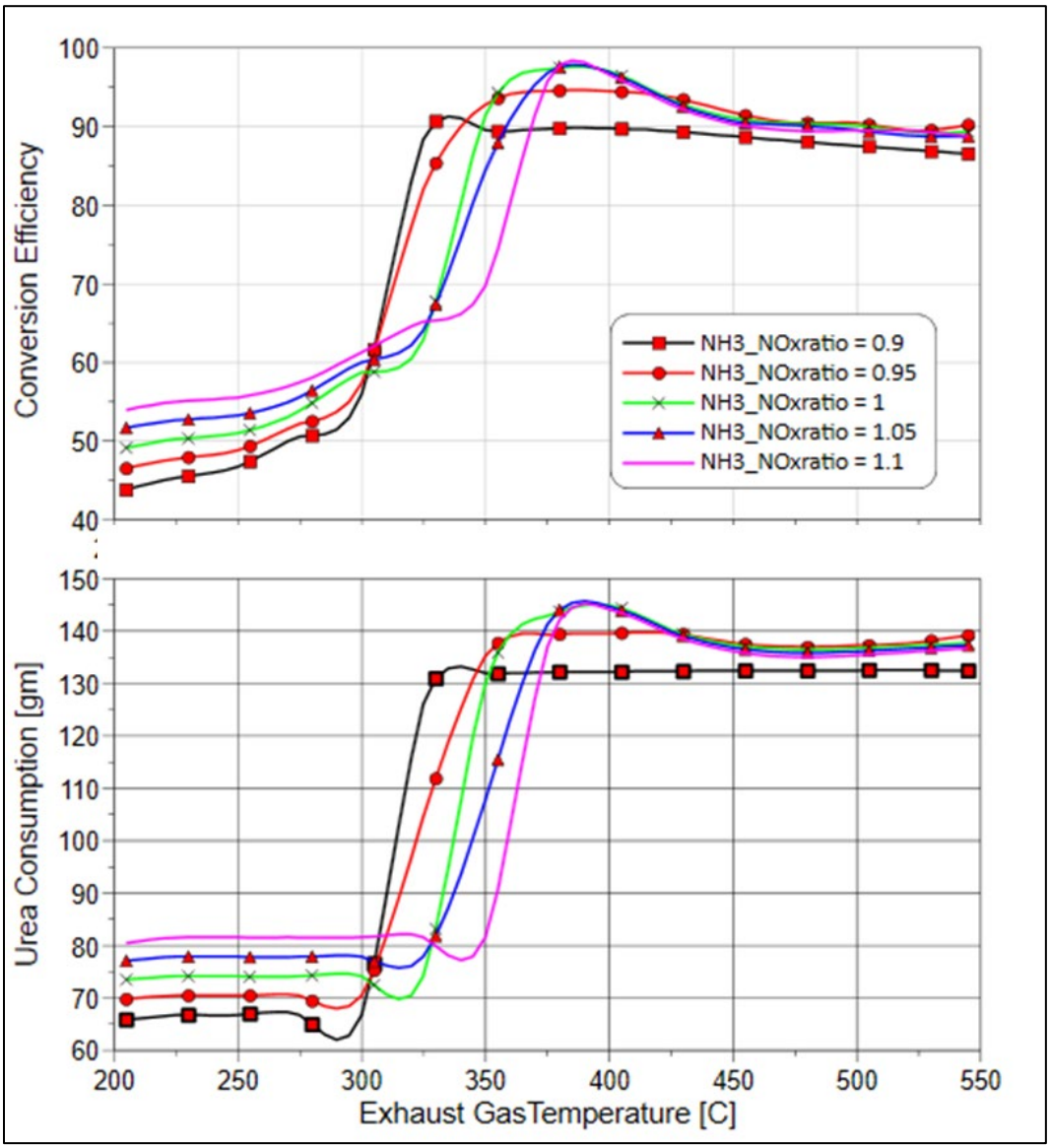

Figure 4.20: Effect of changing EGT for different NH_3: NOx ratio (Fe-Zeolite catalyst)

temperature. This is the primary cause for the decrease in the fraction of NO_2 in the total amount of NOx shown in Figure 4.22 that ultimately affects overall NOx conversion efficiency.

NOx conversion efficiency escalates with increasing NH_3:NOx ratio at a lower temperature. Although, urea consumption alleviates for higher NH_3:NOx ratio, this can be utilized to improve NOx conversion efficiency at a lower temperature. During a cold start, tail-pipe NOx emission is very high which can be reduced to a certain extent by dosing a slightly higher amount of urea at a lower temperature. Implementing this strategy could help to eliminate the cost of a feedback controller for urea dosing without having a detrimental impact on the conversion efficiency and urea consumption. However, in real applications, the urea-solution is dosed upstream of SCR inlet for NOx conversion, which might lead to incomplete thermal decomposition of urea to form NH_3 at a lower temperature. This could be a reasonable approach if urea heater is implemented in the system for the thermal decomposition that would improve NOx conversion efficiency at a lower temperature.

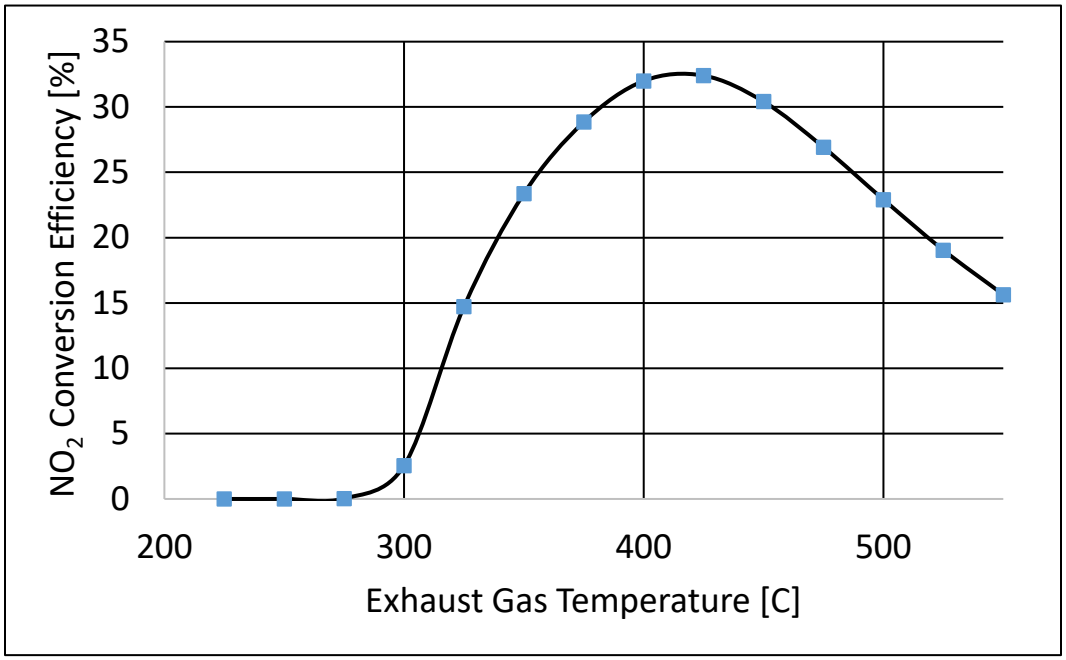

Figure 4.21: NO_2 conversion efficiency at DOC

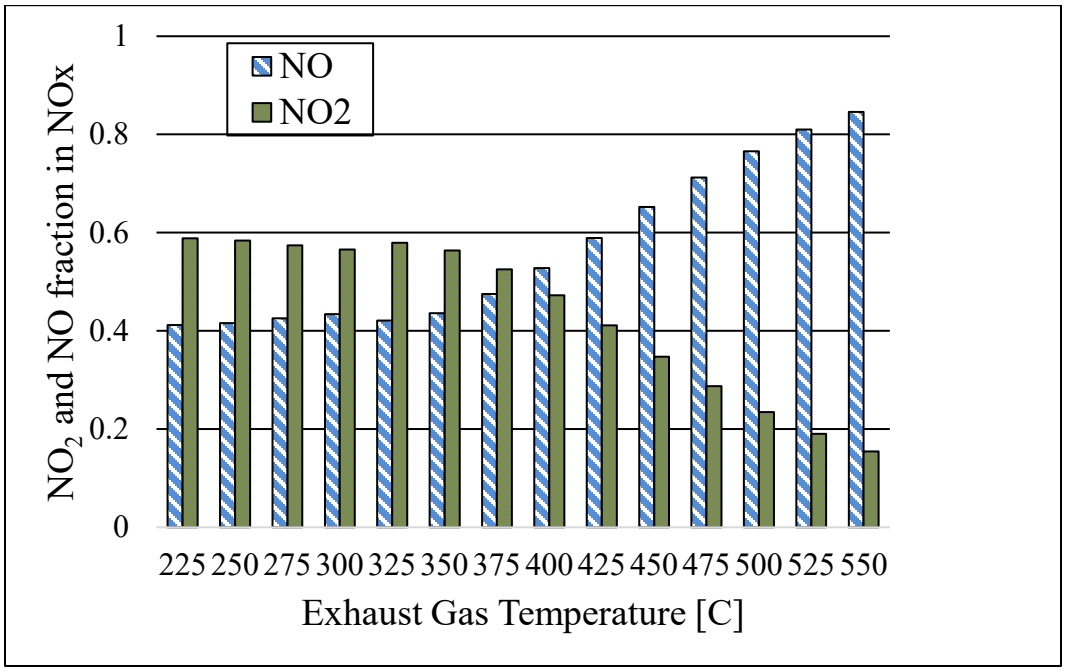

Figure 4.22: NO and NO_2 fraction at SCR inlet for different EGT

4.4. Cold Start Simulation

Table 4.7: Engine-out and tailpipe emission

Exhaust gas species	Engine emission [gm]	Tailpipe emission [gm]	Conversion efficiency
Unburned HC	0.41	0.09	78.71%
NOx	30.11	2.02	93.29%

The engine-out emissions and tailpipe emissions for NOx and unburned hydrocarbons are shown in Table 4.7. The measured emissions are obtained during 1200 seconds of engine operation at a fixed point. The exhaust gas quantity includes emission for cold-start, and the overall conversion efficiency of the after-treatment system for unburned hydrocarbons and NOx is evaluated as 78.71% and 93.29%, respectively. The unburned hydrocarbons emission is comparatively lower than NOx emission, so, the conversion efficiency of 78.71% is adequate for this application. However, the conversion efficiency of the after-

treatment components will increase if cold-start emissions are excluded from the analysis. The engine emissions during cold-start and some thermal management strategies to minimize emission during cold start is discussed following section.

Most of the tail-pipe NOx emission occurs during the cold start of an engine because the catalyst is ineffective until it reaches the catalyst light-off temperature. Cold start simulation was studied by coupling engine and after-treatment components in GT-Suite® simulation environment. The initial ambient temperature and the catalyst temperature are kept 25^0 C for simulation. The engine is operated at the optimum operating point and reaches steady-state after a few seconds of operation. In modern diesel engines, different EGT management strategies are implemented to decrease catalyst light-off time by splitting of the main injection, late post-injection, retarding injection timing, miller timing, early exhaust valve opening, controlling intake throttle and exhaust throttle. Engine cold start behavior was studied in this section. In addition, the effect of retarded injection timing and late post-injection to increase EGT for faster catalyst warmup are also overviewed.

Figure 4.23 demonstrates the higher unburned hydrocarbon emissions during the first five minutes engine operation as the temperature inside DOC catalyst is low in the beginning, but CO emission increases as the EGT is increased. This is due to the passive regeneration of soot in DPF. As the temperature in DOC catalyst increases, formation of NO_2 rises that supports passive regeneration in DPF. During passive regeneration process, NO_2 reacts with the soot particle forming CO and NO mentioned in Table 3.6 and Table 3.7. This causes increase in tailpipe CO emission. It can be seen from Figure 4.24 that tail-pipe NOx emission is significant during the first five minutes of engine operation because the catalyst takes time to heat up and reach the light-off temperature. After attaining light-off temperature, NOx conversion efficiency rises, decreasing tailpipe NOx emissions.

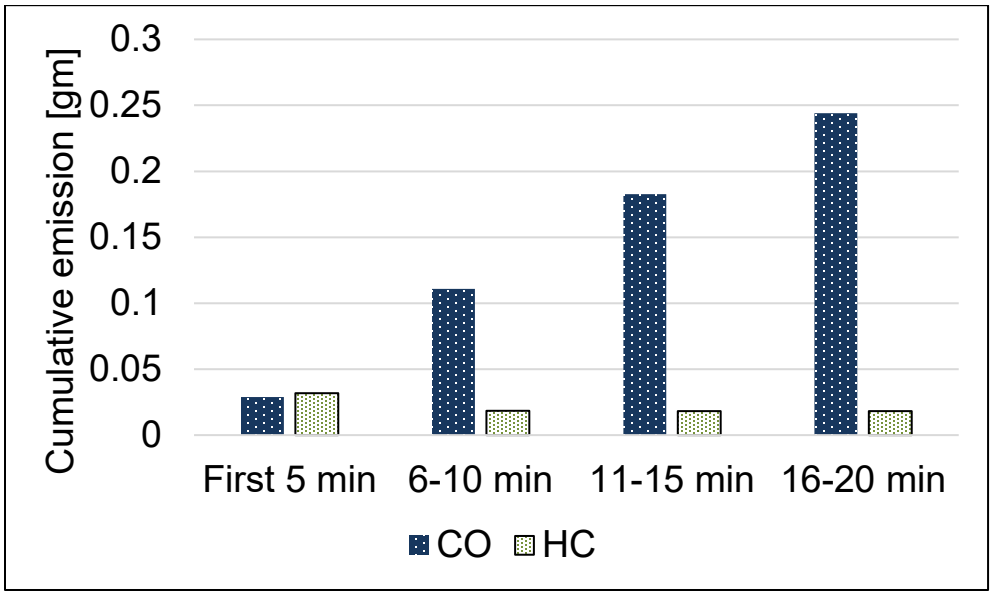

Figure 4.23: Cumulative HC and CO tailpipe emission during cold start for engine running at a constant load of 35 kW and 2000 rpm; $T_{ambinet} = 25^0$ C

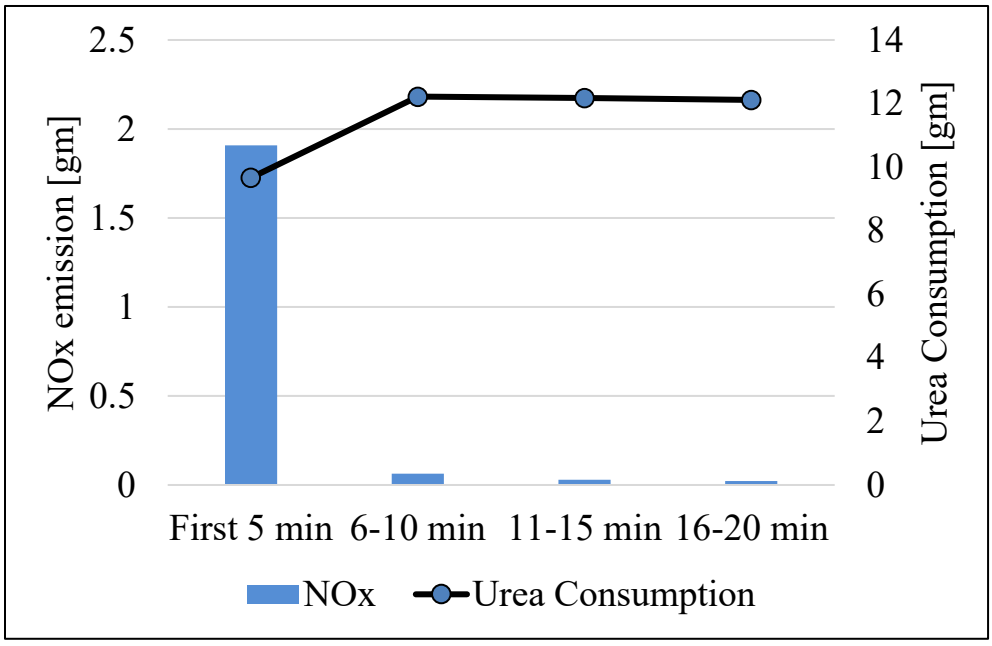

Figure 4.24: Cumulative tail-pipe NOx emission and urea consumption during cold start for engine operating at the constant load of 35 kW at 2000 RPM; $T_{ambient} = 25^0$ C

The effect of retarding injection timing from the main injection timing and late post-injection on emissions and urea consumption is studied. The suitable strategy can be implemented in the model to reduce tail-pipe NOx emission during cold start emission. For retarded injection timing, fuel injection is retarded from the main start of injection when DOC temperature reaches at 300^0 C and continues till SCR temperature reaches 350^0 C. For late post-injection, 2 mg of additional fuel was injected per cylinder per cycle later in expansion stroke in the same condition as defined for retarded injection timing. All the engine operating parameters used were the same as in the optimal operating point. In these two-strategies unburned hydrocarbons reach DOC thereby oxidize to release heat and raise the exhaust temperature downstream of DOC catalyst.

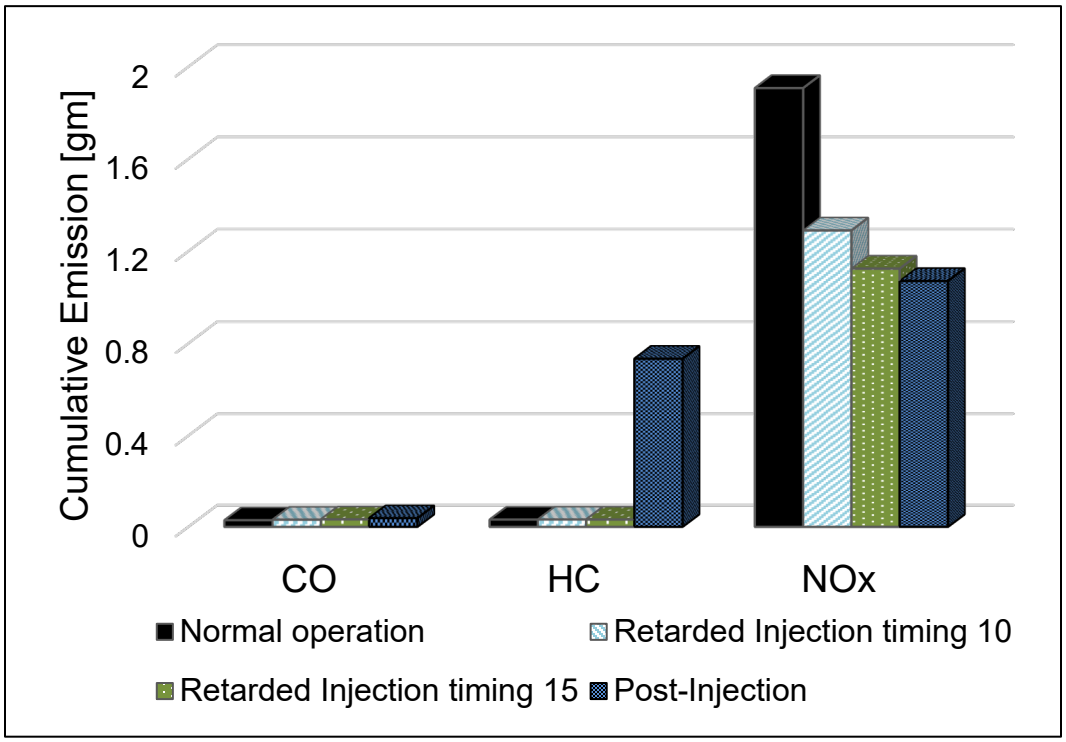

Figure 4.25: Cumulative tail-pipe emission for different thermal management strategies

Figure 4.25 shows tailpipe emissions during the cold start of an engine. The cumulative tailpipe emissions after five minutes are shown in the bar chart to represent the cold start

emissions. Retarding injection timing and post-injection can be used to minimize tail-pipe NOx emission. The late post-injection strategy highly decreases tail-pipe NOx emission, but unburned hydrocarbon emissions are also amplified as DOC fails to burn an additional amount of fuel completely. Retarding injection timing also cuts tail-pipe NOx emission without serious effect on unburned HC emissions. Therefore, for this engine model, retarding injection timing by 15 CA deg from the main injection timing during cold start is suitable that will reduce the tail-pipe NOx emissions by 40% during the cold start. Further retarding of injection would benefit in attaining catalyst light-off temperature at a faster rate, but overall engine performance degrades due to oil dilution and combustion instability.

Chapter 5: Powertrain Sizing and Complete Model Analysis

5.1. Introduction

The powertrain is sized for the VDI 2198 drive cycle. However, it is aimed to design the hybrid components that meet road grade of 20%, which closely resembles the available forklift specification data listed by the forklift manufacturers like Toyota and Hyundai [87].

For this study, only key hybrid drivetrain components like an electric motor, battery, and generator are sized, and a supervisory controller based on a heuristic approach is implemented so that hybrid forklift can meet the performance requirement at different driving conditions while other components are chosen using engineering judgments.

5.2. Electric Motor

Forklifts are designed to lift a heavy load and move them to the designated spot. So, the forklift traction motor is modeled to meet the power requirement for a maximum gradeability of 20% as the design for speed and acceleration are not essential criteria for forklift. The peak power requirement for the maximum speed, maximum acceleration, and the maximum grade is computed by using Equations (3-5), (3-6), and (3-7), assuming motor/controller assembly efficiency to be 0.9.

Table 5.1: Peak power demand for different performance criteria

Performance criteria	**Peak power (kW)**
Maximum speed (V_{max}=20 km/hr)	29.9
Maximum acceleration	40.6
Maximum grade (V_{max} = 10 km/hr)	86.3

The peak power for a maximum grade is observed to be 86.3 kW, as seen in Table 5.1. The vehicle mass and the rated load (5000kg) are added for calculation of peak power in all cases. Table 5.2 shows the traction power demand of the forklift at different vehicle speeds and grades. Increase in the road grade raises traction power demand. At higher road grades, an increase in the vehicle speed will lead to a drastic increase in traction power demand, as seen in the result for vehicle operating at 20% and variable speeds in Table 5.2.

Table 5.2: Traction power demand at different road grades

Road grade [%]	**Max. speed (m/s)**	**Traction power [kW]**
2	3	24
	4	32
5	3	36
	4	48
9	3	52
	4	70
11	3	60
	4	80
17	2	55.5
	3	83
20	2	63
	2.75	86

As a forklift is designed to operate at 20% gradeability with carrying rated load, the electric motor of peak power greater than 86 kW is required. Therefore, an interior permanent magnet (IPM) electric motor manufactured by Higen motor with the peak power of 90 kW and continuous power of 55kW, is chosen for this hybrid powertrain. The IPM motors can provide high torque at low speeds, which is suitable for the forklift applications. The

performance characteristic of the selected motor in Figure 5.1 is adapted from reference [88] and used as a torque map in the GT-Suite® motor model. Additionally, the traction motor controller is used that computes the maximum and minimum brake power limits based on current speed and torque. With the sizing of the motor, the final drive ratio (FDR) is determined as 31.66 from Equation (3-8). As this computed final drive ratio is too high for real application, a reasonable FDR of 23.5 is chosen on a trial-error basis that can meet the performance requirement of a hybrid powertrain. This FDR is capable of handling a maximum rated load to provide the required traction power demand.

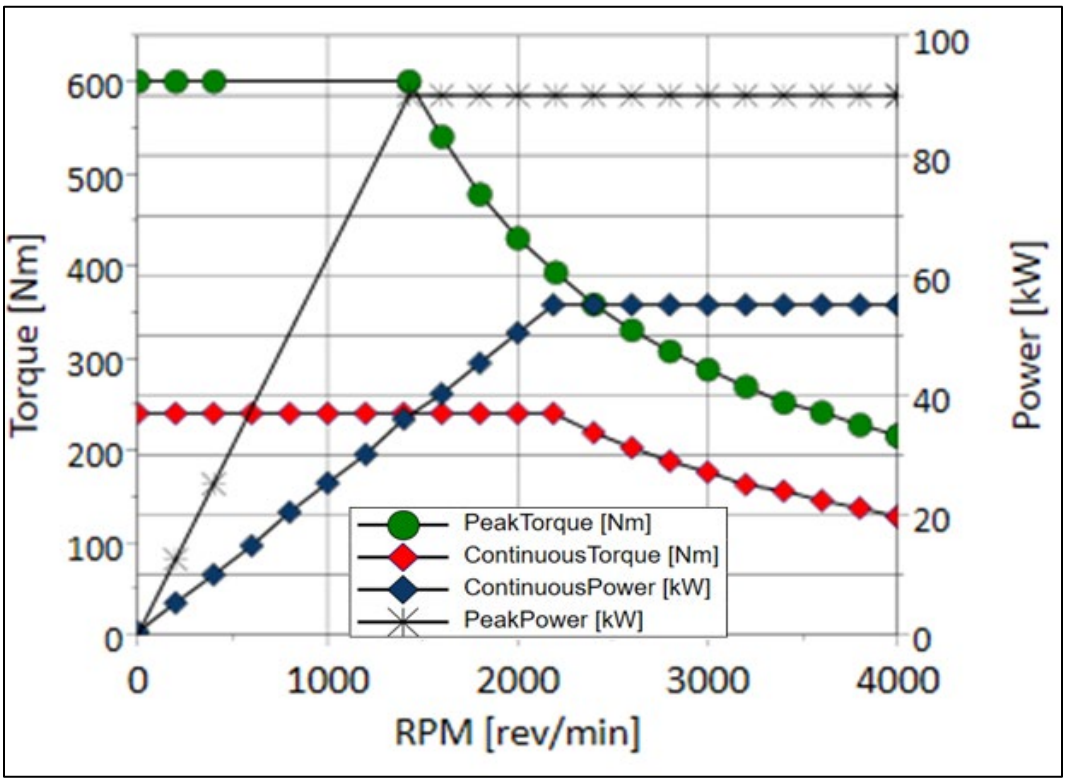

Figure 5.1: Performance map for the selected traction motor – Data is extracted from reference [88]

5.3. Battery Sizing

The capacity of battery required to meet powertrain performance is determined with the Equation (3-8), provided in the reference [49]. The power capacity of battery calculated is 65 kW, assuming motor efficiency to be 0.95 and the engine/generator efficiency as 0.9 [89] . Detail calculation of battery sizing is included in Appendix E.

The hydraulic power is not considered while calculating the power capacity of the battery as the lifting operation is carried out only when the vehicle is at rest. As the energy/power ratio of Li-ion battery is 0.1 provided in Table 16.4 of the reference [49], the required battery capacity is calculated as 6.5 kWh. The nominal voltage of a lithium-ion cell used in GT-Suite® power is 3.3 V, as seen in Figure 3.12. Therefore, to achieve a voltage of 320 V, the number of cells in series was chosen as 97, and the number of cells in parallel is calculated as 3 assuming the capacity of each cell as 7 Ah. The battery parameters are summarized in Table 5.3.

Table 5.3: Sizing of battery

Battery type	Li-ion
Number of cells in series	97
Number of cells in parallel	3
Cell capacity	7 Ah
Nominal cell voltage	3.3 V
Total battery capacity	6.72 kWh

5.4. Vehicle Supervisory Controller

The controller blocks are used in the GT-Suite® model to implement a control strategy for the different operating condition. The control strategies are based on a heuristic control strategy discussed in the supervisory control section of Chapter 2. The regenerative braking

controller is implemented to determine operating modes of the vehicle and splitting the power demand between regenerative braking and friction brakes. The operating modes defined in the regenerative braking controller is shown in Table 5.4.

Table 5.4: Regenerative braking modes

Operating Mode	**Condition**
No braking (Mode 1)	$P_{traction} > 0$
Friction braking (Mode 2)	SOC>0.9 OR $Acc_{vehicle} < -2m/s^2$
Regenerative braking (Mode 3)	$P_{traction}$<-$Limit_{regen}$
Hybrid braking (Mode 4)	$P_{traction}$>-$Limit_{regen}$

The friction braking is applied when SOC of battery is very high or substantial deceleration is required for instantaneous braking. The regeneration braking limit is determined by the battery management system, and if the amount of regenerative braking is over the regenerative limit, then the hybrid braking is applied to prevent the battery from damaging.

Engine start/stop control strategy is also defined inside the supervisory controller block to set the engine on/off criteria. Two operating modes implemented in the system are:

- Charge Depleting: Battery is used to provide energy for traction as well as a hydraulic lift that results in depletion of the battery SOC
- Charge Sustaining: Engine/Generator combination primarily provide energy for traction and hydraulic lift maintaining battery SOC to the specified range

The minimum and maximum battery SOC limits are defined that mainly determine the start and stop of the engine. The engine on/off criterion is an integral part of the control strategy and depends on the following conditions:

- Battery SOC is lower than a minimum specified threshold
- Traction power demand is higher than 55 kW
- After-treatment temperature associated with SCR is below the light-off temperature

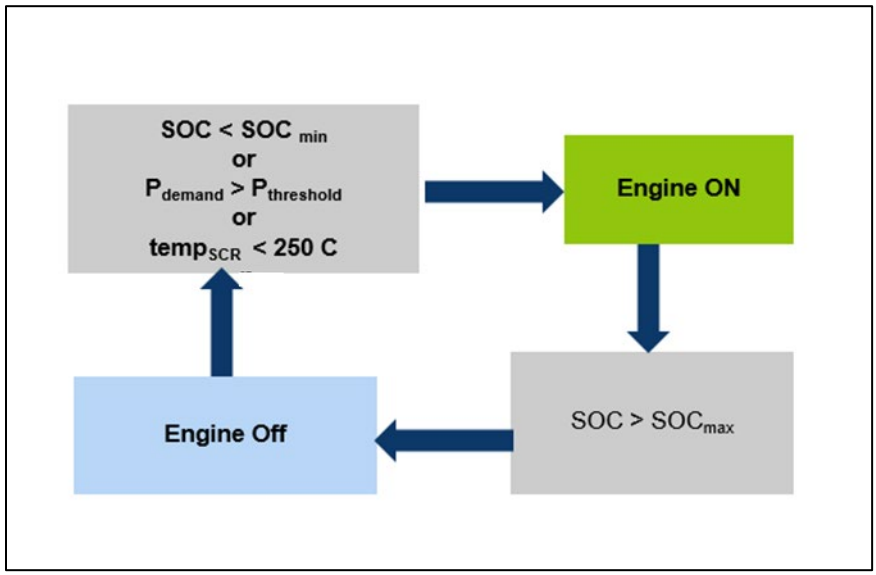

Figure 5.2: Engine on/off control strategy

The engine on/off logic is modeled for this study. The engine will start depending upon traction power demand, battery SOC level, and temperature of SCR catalyst, portrayed in Figure 5.2. The catalyst temperature is used as a control variable in the model because catalyst conversion efficiency drastically reduces if the temperature decreases below the light-off temperature. This would result in higher emissions when the engine is started again. So, to minimize emission, catalyst temperature is also considered while modeling engine on/off strategy.

5.5. Evaluation of Powertrain Performance

The powertrain performance is mainly determined by the engine size, motor size, battery size, and the control strategies for the operating modes and drive cycle. Assessment of those factors on the powertrain performance is discussed in the section below.

The engine is continuously producing 167 Nm torque at 2000 RPM so generator size is selected that would operate at an efficiency greater than 85% at those points. An electric motor is modeled with the equations stated in Section 3.4.4 and performance map of

permanent magnet with 90kW peak power is used for toque map for the motor in GT-Suite®. The battery is designed that would meet the maximum power requirement of 60 kW considering engine generator set would provide slightly over 30 kW when 90 kW peak power is required for traction.

5.5.1. Traction Motor and Hydraulic Motor Performance

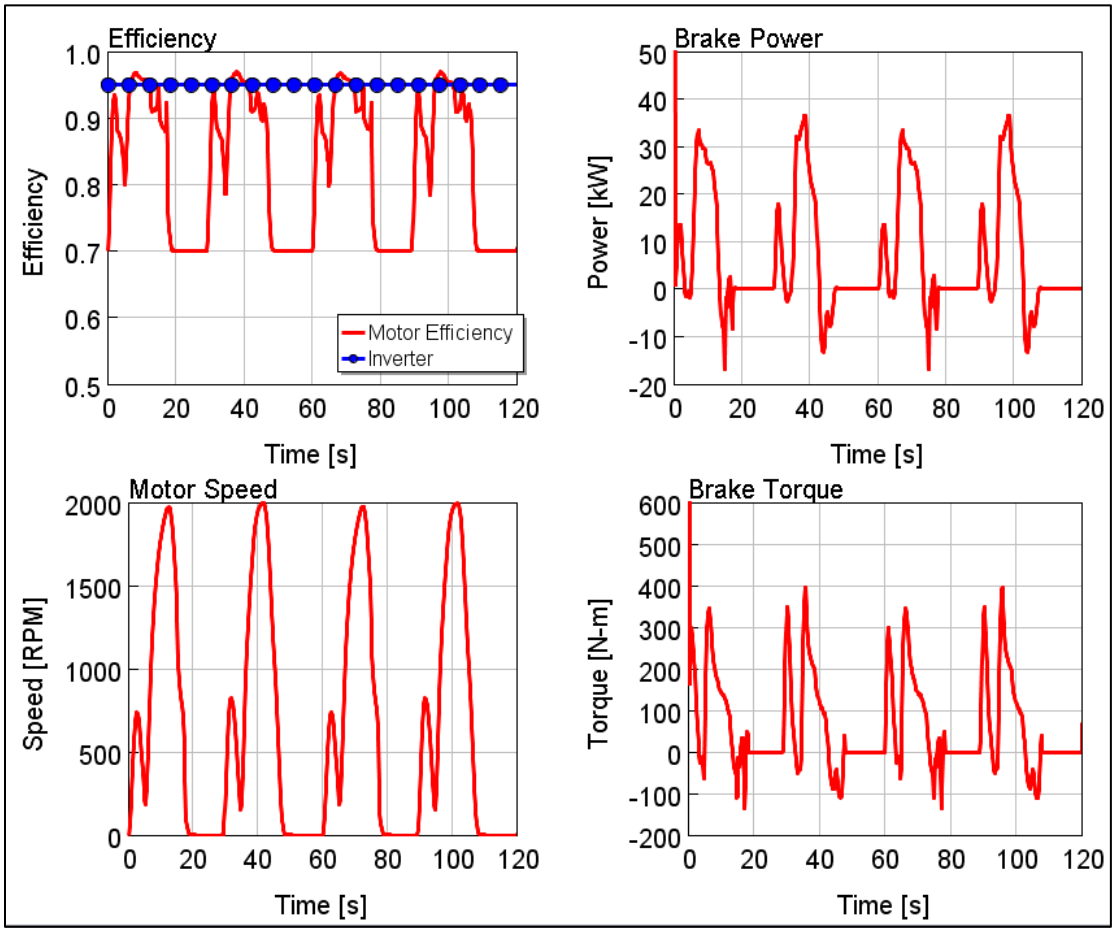

Figure 5.3: Traction motor performance (a) Efficiency, (b) Break Power, (c) Motor speed and (d) Speed

The traction motor performance for two consecutive VDI 2198 cycles is shown in Figure 5.3. VDI is a 60 seconds cycle that involves traveling of the forklift and lifting operation.

During lifting operation, traction motor remains idle as the vehicle completely stops during that instance. The peak power required for traction in a forklift is around 35 kW, and the negative region in the torque curve indicates that traction motor is utilized for regenerative braking. The constant inverter efficiency of 0.95 is applied to the motor model, and the motor efficiency is varying depending on the speed and load demand.

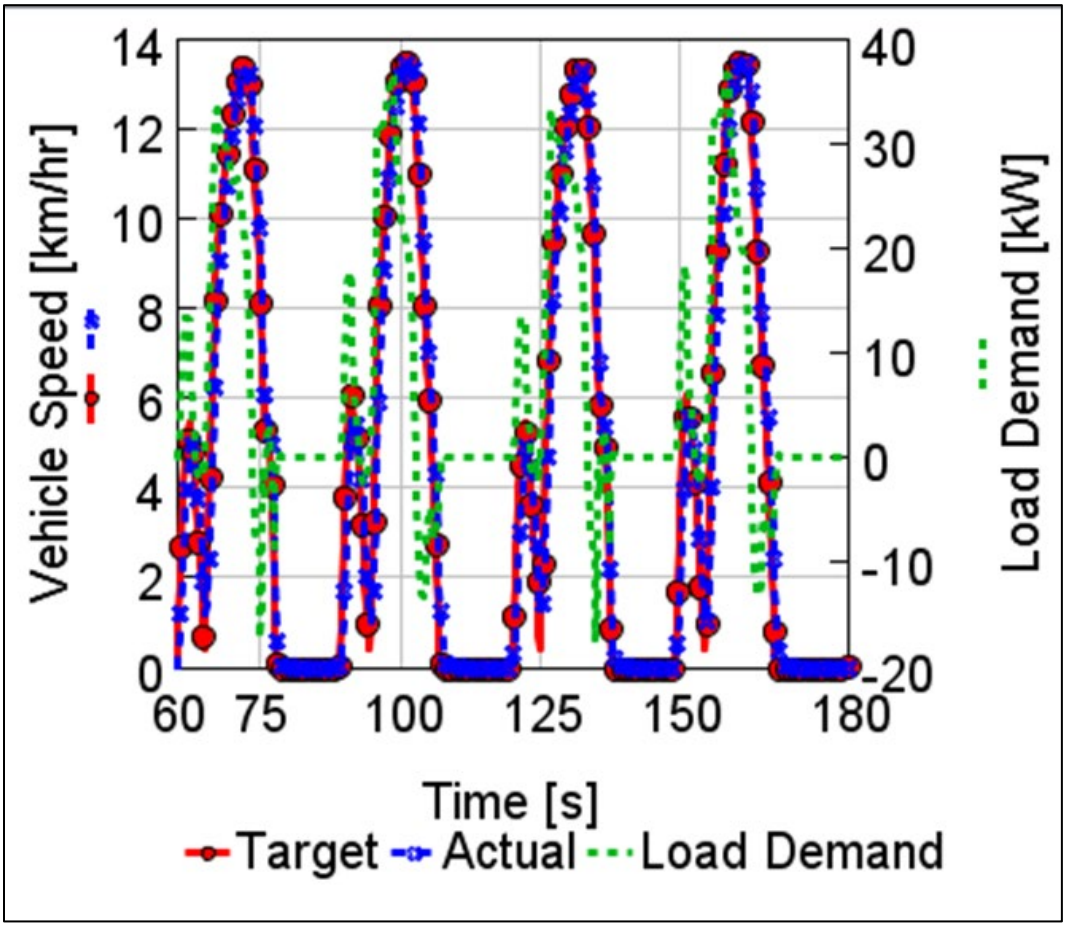

Figure 5.4: Vehicle speed and load demand curve in a VDI 2198 cycle

Figure 5.4 shows a comparison for the target vehicle speed profile and the actual speed attained by vehicle during the simulation. The actual vehicle speed profile from the simulation is following the target vehicle speed profile of VDI 2198 cycle. This indicates that the designed powertrain can meet the power demand requirement of the VDI cycle.

The load demand for a vehicle depends on the vehicle speed profile as seen in Figure 5.4, and load demands increase for high speeds. The peak traction power demand for the forklift during VDI cycles is less than 40 kW.

The peak load for a hydraulic motor is around 20 kW for the VDI cycle. It is assumed that the power requirement for the accessory load, including steering and braking, is also provided by a hydraulic motor that leads to energy consumption during driving too. The motor chosen can deliver the necessary power for lifting operation, and it is following the load curve, which can be noticed in Figure 5.5.

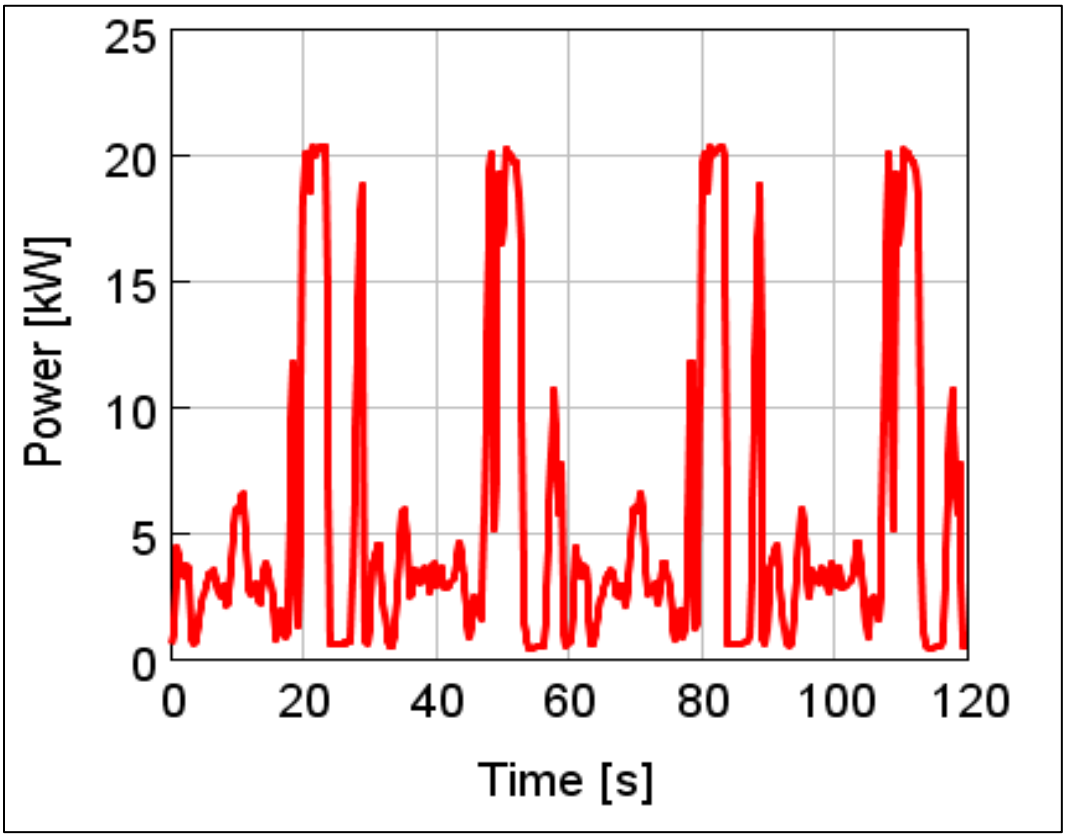

Figure 5.5: Hydraulic motor load for a VDI 2198 cycle

5.5.2. Battery Performance

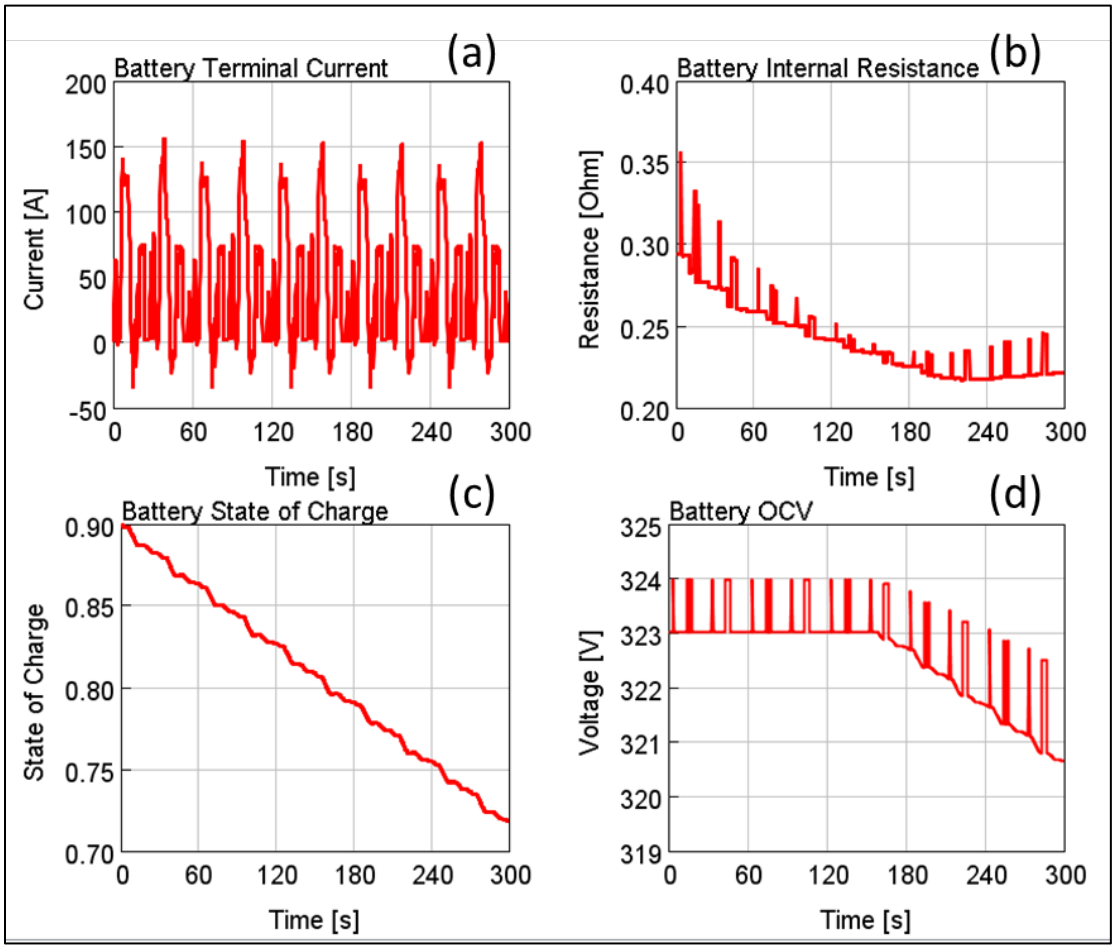

Figure 5.6: Battery performance curve (a) Battery terminal current; (b) Battery internal resistance; (c) Battery stage of charge; (c) Battery open circuit voltage

The battery performance for 300 seconds of repeated VDI 2198 cycles is shown in Figure 5.6. The open circuit voltage (OCV) of battery is varying from 320 V to 324 V, and internal resistance is ranging between 0.22 Ω to 0.36 Ω. OCV of battery slightly varies for the change in the state of charge (SOC) of battery, which we can be clearly seen from Figure 5.6(d). The battery terminal current is the current drawn (positive) from or current provided (negative) to the battery during the VDI cycle. The current drawn from the battery is low when the engine is on because the battery only acts as peaking power source during

that instance. A huge amount of current is drawn from the battery during charge depletion mode as the battery is the only energy providing source. Battery minimum SOC is assumed as 0.5, and the maximum SOC threshold is assumed as 0.9, considering the catalyst temperature doesn't decrease below the temperature where conversion efficiency is worse for longer engine shut-off duration. The battery OCV drastically drops below 0.4, and the high-power demand required for the longer period cannot be met by the battery when the battery SOC is low. This is another reason for choosing a minimum SOC of 0.5.

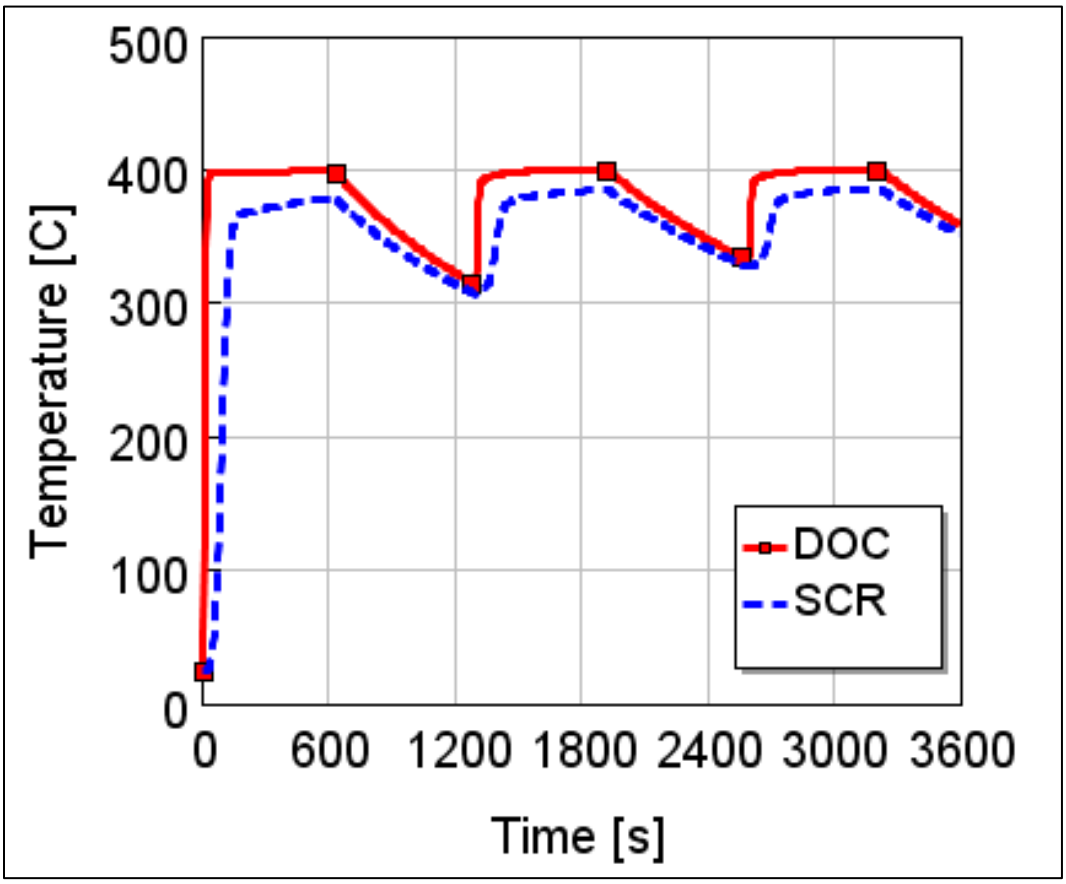

Figure 5.7: SCR and DOC catalyst temperature during VDI 2198 cycle

The temperature at the center of the SCR catalyst and DOC catalyst is shown in Figure 5.7. The catalyst temperature is at room temperature (25^0 C) at the beginning of the cycle. SOC of battery is 0.5 at the beginning, so the engine is started immediately, which leads to an

increase in temperature of the catalyst. The DOC catalyst temperature quickly rises and reaches steady state as it is close to the exhaust system, but SCR catalyst being located comparatively farther takes little more time to reach to light-off temperature. The engine is switched off after SOC reaches 0.9, and the catalyst temperature starts to drop. It takes around 650 seconds for a battery to reach SOC level 0.5 and the engine is switched on again. For 650 seconds, SCR temperature only drops to 300^0 C and quickly reaches a steady-state temperature after the engine is restarted.

5.5.3. Battery Performance at Constant Load

VDI drive cycle is predictive and straightforward with road grade of 0% that requires the peak power demand less than 40 kW. While designing a motor, the peak power demand for the vehicle with a rated load at 20% grade is computed around 86 kW. During the peak power demand, both engine/generator assembly and battery will be delivering power for traction. So, it is assumed that 30 kW power will be delivered by the engine/generator assembly and the remaining 56 kW by the battery during the peak power demand. In order to evaluate the performance of a battery during those peak powers, the battery is tested separately with a constant load of 60 kW, 45 kW and 30 kW. Battery initial SOC for all these cases was kept constant at 0.9, and continuous power is drawn from the battery using load source. It can be noticed from Figure 5.8 that the battery takes around 300, 200, and 140 seconds to reach a SOC level of 0.5 for drawing the constant power of 30 kW, 45 kW, and 60 kW respectively.

The OCV of the battery decreases as energy is depleting, and the current drawn from the battery increases for 60 kW power demand. The power drawn from the battery is directly proportional to the current, as observed in Figure 5.8. When battery SOC declines below 0.4, current drawn from battery increases to provide the required power as battery OCV drops. The battery heats up rapidly if a higher amount of current is drawn, so the existing battery design will be able to handle peak load for only 120 seconds. This

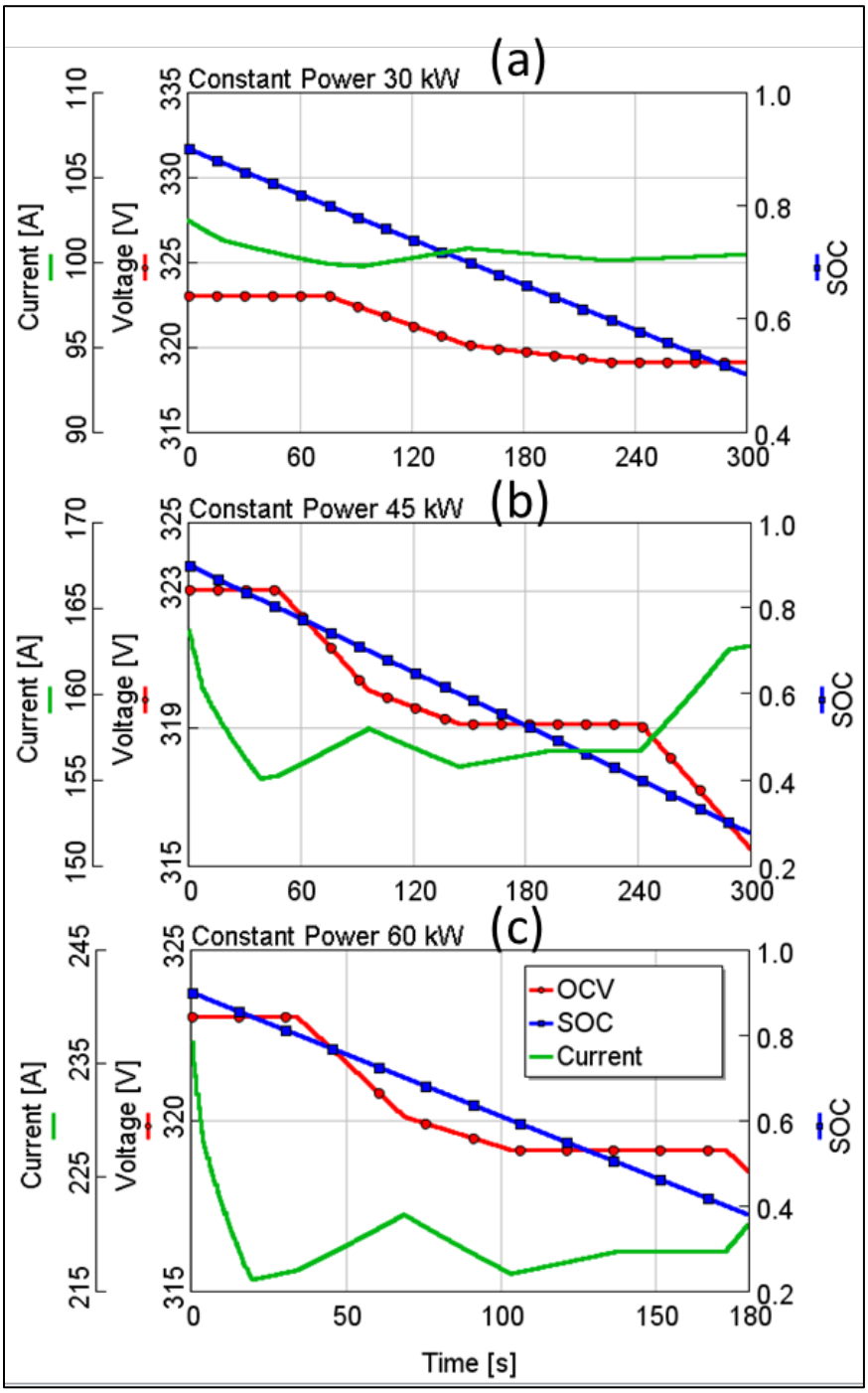

Figure 5.8: Battery performance at constant load; (a) 30 kW; (b) 45 kW; (c) 60 kW

indicates that forklift should not be operated at continuous peak load for more than two minutes that would cause excessive heating of the electrical components leading to permanent failure. However, this kind of scenario is only possible in the worst case and won't be seen in real practice. In real driving cycle, power demand is constantly changing, but this battery performance analysis helps to estimate the extreme capability of the battery system.

5.5.4. Engine Operating Modes in the VDI cycle

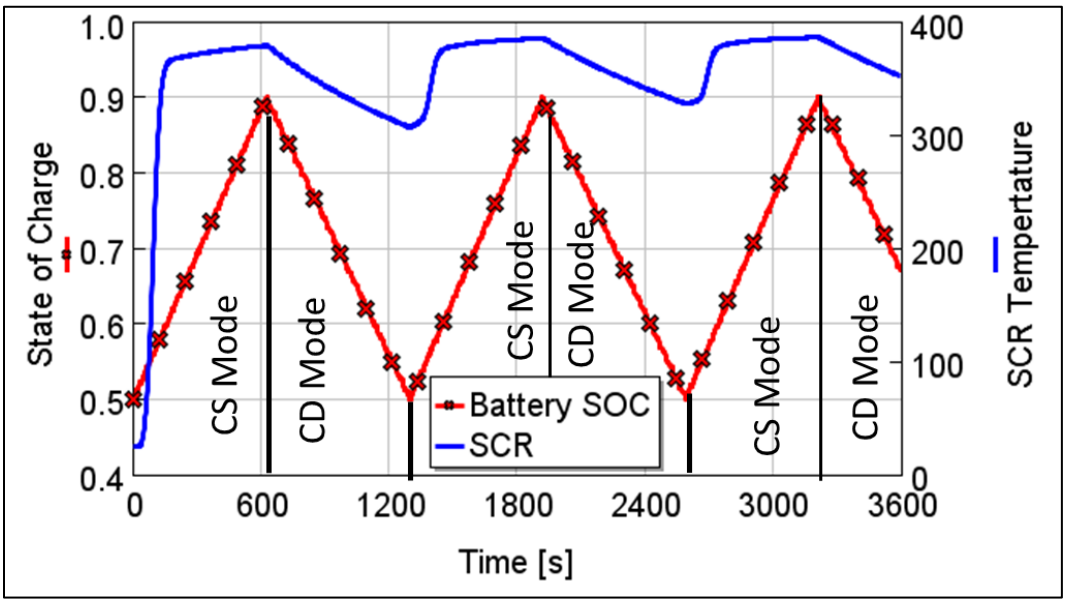

Figure 5.9: Charge sustaining (CS) and charge depleting (CD) modes in the 60 VDI cycles

The engine on/off criterion defined in the HEV supervisory controller depends on the traction power demand, the temperature of the SCR catalyst, and battery SOC. Figure 5.9 shows the switching of operating modes in the VDI cycle. The engine starts at the beginning of the VDI cycle as the battery SOC is 0.5 at the initial stage. The engine/generator assembly primarily provides the necessary power for the lifting and traction. During charge sustaining mode, the battery is charged when the power demand is

less than the power produced by the engine/generator assembly. In addition, the battery is also charged by regenerative braking from the traction motor. The battery acts as a peaking power source if the power demand is higher than the power produced by engine/generator assembly. It can be seen from Figure 5.10 that the power demand during the VDI cycle is generally low, met by the engine/generator power. Therefore, the battery is charged faster in CS mode and reaches SOC 0.9 in almost 600 seconds.

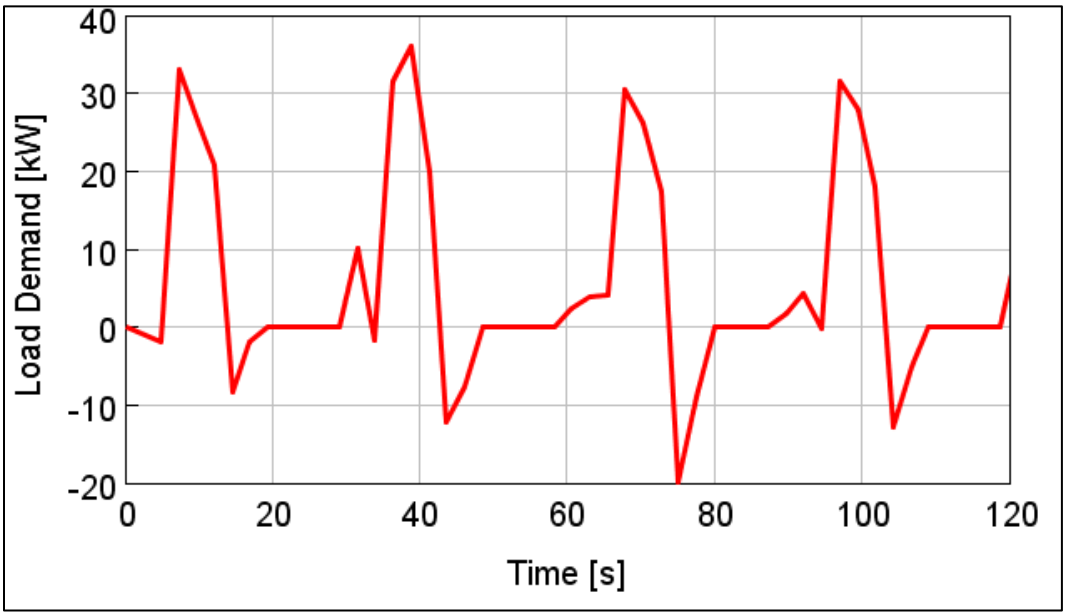

Figure 5.10: The traction power demand during VDI cycle

The SCR catalyst temperature also reaches around 370^0 C exceeding the catalyst light-off temperature during 600 seconds of the engine operation as seen in Figure 5.9. So, the engine is switched off, and the operating mode is now switched to the charge depletion mode. The battery solely provides the necessary power for the traction and lifting operation during CD mode and the battery is charged only by the regenerative braking from the traction motor. As the traction and the hydraulic power demand is less than 55 kW in the VDI cycle, and the SCR temperature also doesn't drop below 300^0 C, starting of the engine

is not required until the battery SOC reaches 0.5. The engine is restarted at this point, and the charge sustaining and depleting modes are repeated in a similar fashion throughout the cycle.

Therefore, the engine on/off criterion defined for the series-hybrid powertrain is adequate for the VDI cycle as it is predictive and straight forward without any irregularities. However, during a real forklift operation, the traction power demand can be higher than 55 kW, the limit defined in the controller. In that situation, the engine is instantly switched on to meet the necessary traction power demand, and it stops after reaching SOC 0.9. The controller strategies are defined to avoid intermittent starting and stopping of the engine. The frequent starting and stopping of an engine decrease the temperature of after-treatment components that increase NOx emission. Also, additional energy is required for the cranking to reach engine rpm at a suitable speed for fuel injection.

5.5.5. Regenerative Braking Modes in the VDI cycle

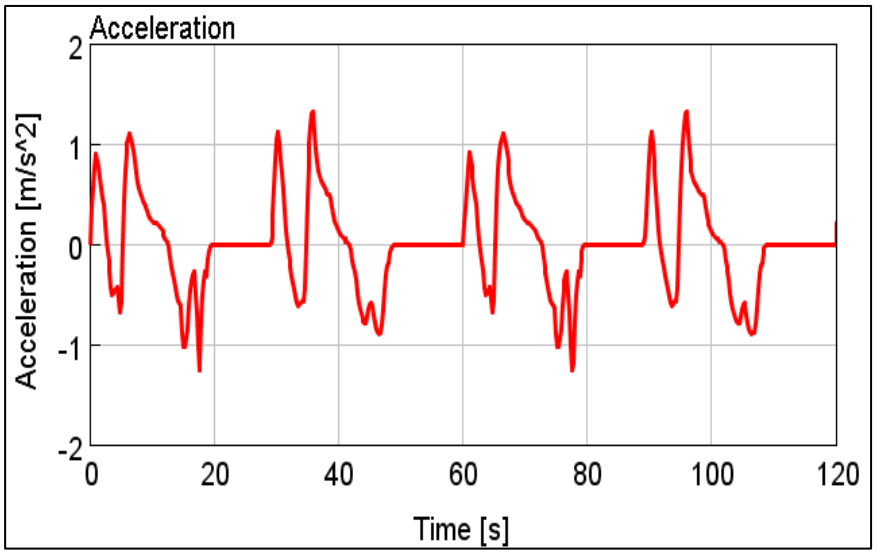

Figure 5.11: The lift truck acceleration profile for the VDI cycle

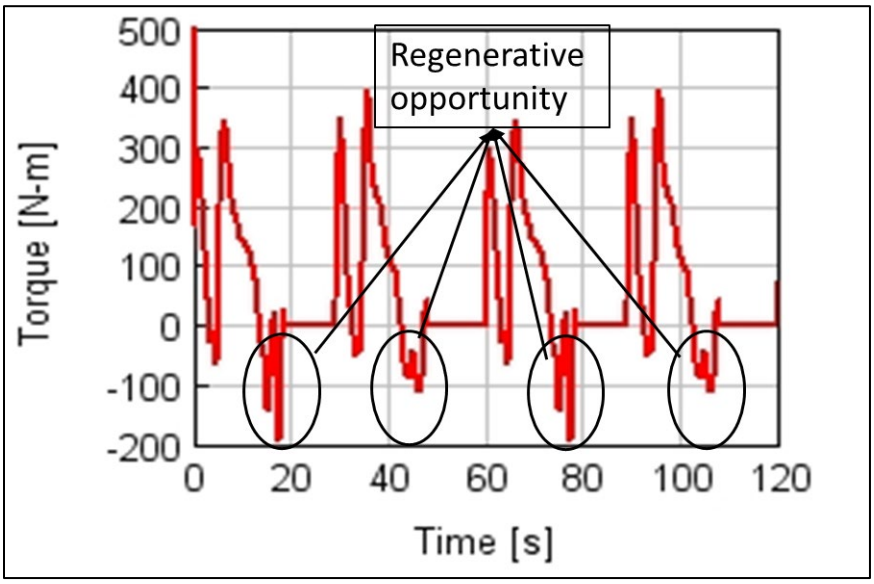

Figure 5.12: Regenerative opportunity in a VDI cycle

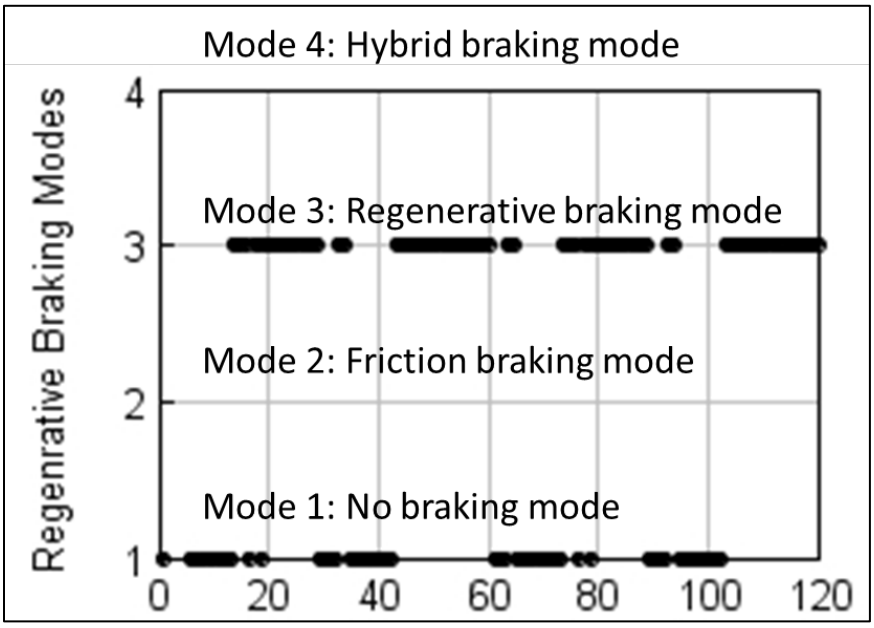

Figure 5.13: Regenerative braking modes of the powertrain in a VDI cycle

VDI 2198 cycle has intermittent peak loads with many decelerations, as seen in Figure 5.11. This provides lots of opportunities for energy recuperation during braking. The

possible regenerative opportunity in the VDI cycle is highlighted in Figure 5.12. The forklift vehicles are operated at low speeds in the VDI cycle, and the deceleration is also less than 1.5 m/s^2. This limits the necessity of friction braking in the cycle to a great extent.

Figure 5.13 shows the regenerative braking modes for the VDI cycle. As the cycle is repetitive and the traction power demand is not higher, it is assumed that the operating modes will be the same throughout the cycle. There are four braking modes defined in the controller for the series hybrid powertrain. However, only two modes are active, i.e. no braking mode, and regenerative braking mode as the VDI cycle has deceleration less than -2 m/s^2, and the corresponding torque required during braking is also less than 200 Nm. This shows that HEV is a good option for this application since all deceleration energy can be captured by regenerative braking in the VDI cycle.

The regenerative braking modes defined in the controller is also dependent of the battery SOC. In conditions where battery SOC is above 0.9 or deceleration is greater than 2 m/s^2, mode 2 will be active and friction braking will be applied without any regenerative braking. Hybrid braking mode will be active when the braking demand is higher than the regenerative limit of the traction motor. This kind of mode is rare for forklift application as the vehicle speed is low. However, this mode can be active when the electric motor is not functioning properly and cannot do regeneration.

5.6. Cost Estimation of After-treatments Components

The size of the after-treatment components is calculated as a function of the engine displacement. Sweep volume ratio (SVR) is an important design parameter that determines the required volume of the catalyst for the given engine size. The relationship among these parameters are shown in the following equation [20]:

$$\text{The volume of catalyst} = \text{SVR} * \text{Engine displacement} \qquad (5\text{-}1)$$

The detail cost analysis for DOC, DPF, and SCR have been carried out in the cost report in the reference [20] for the non-road diesel engine size ranging from 1.7 to 10.8 L. The typical range of SVR mentioned in the literature for DOC, catalyzed DPF and Euro V SCR is 0.5 - 0.8, 1.6 -2.4 and 1.4 - 2.0, respectively. SVR is chosen as 0.7, 2, and 2 for DOC, DPF, and SCR, respectively to compute the cost of the catalyst [20]. The catalyst volume and their respective cost for 1.7 L, 2.6 L, 4.9 L, and 10.8 L diesel engines are computed using an empirical formula provided in the reference [20]. Therefore, these empirical formulas are used to compare the cost of after-treatment components for the conventional 2 L diesel engine and the selected after-treatment components for a series hybrid powertrain in this thesis.

The estimated catalyst volumes in the reference [20] are for the conventional diesel engines that operate at multiple speeds and load points. As the diesel engine model for the study is only running at a single point, the reduced catalyst size can be used in our case. The catalyst volume that has been used to meet the emission requirement is mentioned in Table 5.5. Based on the calculation procedure specified in the reference [20], the cost of an after-treatment component depends on precious metals, storage capabilities, the substrate, and housing for mechanical support. The similar approach defined in reference [20] is used to estimate the cost of after-treatment components without upgrading the cost of accessories, manufacturing cost, and miscellaneous cost. As the empirical formula for the cost of accessories materials is not provided, accessories and urea system cost of 1.7 L diesel engine is used for the evaluation of total cost.

The catalyst length reduction will cut off the use of costly PGM like Platinum and Palladium for DOC and DPF decreasing the catalyst cost. The detail calculation of the after-treatment component is included in Appendix F, and the summary of the cost estimation is tabulated in Table 5.5. The reduction in catalyzed DPF and DOC provides cost benefits of 28% and 27%, respectively. Reducing the size of the SCR catalyst has a comparatively less cost-benefit percentage as precious metals are not used in SCR catalyst.

However, the actual reduction price is higher compared to the other two catalysts. Furthermore, a reduction in SCR catalyst volume will decrease urea consumption benefits, which will save operational cost. Overall cost benefit due to the reduction of catalyst size of the after-treatment components is evaluated as 19.8% equivalent to $235.

Table 5.5: Cost estimation of the after-treatment components – Adapted from reference [14]

After-treatment component	**DOC**	**DPF**	**SCR**
Swept volume ratio (SVR)	0.7	2	2
Catalyst volume [L]	1.4	4	4
Total cost of catalyst	$103	$267	$817
Reduced catalyst volume for the hybrid powertrain [L]	1	2.3	0.95
Reduced cost	$74	$193	$685
Cost benefit in dollars	$29	$74	$131
Cost benefit* [%]	28	27	16

*cost-benefit percentage is calculated comparing with the base after-treatment model provided in the reference [20]

5.7. Energy Recuperated from Regenerative Braking

The regenerative braking is computed in the model using the negative battery current and open circuit voltage signal from the battery during charge depletion mode. This provides instantaneous power, integrated to convert into energy. This approach is suitable for computing energy recuperated during regenerative braking as the battery is discharging all the times except for regeneration. Moreover, from battery performance, we can observe that the battery OCV is not varying a lot, which makes it a suitable approach.

The energy recuperated during five VDI cycles is evaluated by running simulation with battery SOC at 0.90, 0.85, 0.80, 0.75 and 0.70. The parameters used for calculating the amount of regeneration are included in Appendix G and the results for different cases are presented in Table 5.6. The result shows 0.05 kW-hr energy is recovered for these cases with a margin of error $1.15*10^{-5}$ kW-hr as there is negligible difference in energy recuperated in 5 VDI cycles. The average energy recuperated for 60 cycles is calculated as 0.60 kW-hr, assuming the total energy recovered for each cycle is constant. The average fuel equivalent is computed as 0.18 L for 60 VDI cycle considering BSFC of the engine as 209.9 gm/kW-hr and the efficiency of generator and inverter as 0.9 and 0.95, respectively.

Table 5.6: Energy recuperated in the VDI cycle

Initial SOC	**Energy Recuperated in 5 VDI cycles (kW-hr)**	**Total energy recovered in 60 VDI cycles (kW-hr)**	**Fuel equivalent energy recovered (L)**
0.90	0.05	0.60	0.18
0.85	0.05	0.60	0.18
0.80	0.05	0.60	0.18
0.75	0.05	0.60	0.18
0.70	0.05	0.60	0.18
Average			**0.18**

5.8. Evaluation of Fuel and Urea Consumption

Fuel consumption of a series hybrid is computed based on the total energy consumption instead of fuel consumption, and the total energy consumption is compared with the equivalent diesel fuel amount for comparative study. Fuel consumption for the conventional diesel forklifts and a series hybrid forklift are compared based on available resources. Fuel consumption for the traditional diesel engine forklift with a similar vehicle

mass and rated load capacity provided in datasheet by the manufacturer is utilized for fuel consumption comparison. Fuel consumption for the forklift is calculated in terms of L/hr rather than L/100 km, which is used for passenger cars or commercial vehicles. The vehicle is operated at a standard test cycle for an hour to evaluate fuel consumption. A similar approach used for determining fuel consumption of the developed series hybrid forklift is included in Appendix H, and the procedure is elaborated below.

To determine the fuel consumption for 60 VDI 2198 cycles, different attributes as battery initial and final SOC, the duration for which engine is on are taken into account from the simulation results. Since the engine operates at a fixed point, fuel consumption is the same throughout the cycle. SOC change at the initial and final time during 60 VDI cycles is noted. Fuel equivalent of energy is calculated based on the variation of battery SOC. For this calculation, the energy equivalent for 1 L of diesel is computed using BSFC of 209.9 gm/kW-hr acquired for optimum engine operating point. The efficiency of the generator is assumed as 0.9, and inverter efficiency of 0.95 for calculation. 1 L of diesel is equivalent of 3.4 kW-hr electrical energy considering loses accounted by the efficiency. The density of diesel engine used is 0.835 kg/L for calculation [77].

Table 5.7: Battery energy calculation for VDI cycle

Case No	**Battery SOC**		**SOC change**	**The energy provided by the battery**	**Fuel Equivalent**
	Initial SOC	Final SOC	Δ SOC	kW-hr	L
1	0.50	0.67	-0.17	-1.14	-0.34
2	0.55	0.72	-0.17	-1.16	-0.34
3	0.60	0.76	-0.16	-1.07	-0.31
4	0.65	0.81	-0.16	-1.10	-0.32
5	0.70	0.87	-0.17	-1.11	-0.33

6	0.75	0.88	-0.13	-0.86	-0.25
7	0.80	0.84	-0.04	-0.27	-0.08
8	0.85	0.78	0.07	0.44	0.13
9	0.90	0.73	0.17	1.17	0.34

Depending on SOC change, fuel equivalent energy is computed, which is shown in Table 5.7. A negative value of SOC change signifies that fuel is used for charging the battery, and the positive SOC change means battery energy is utilized to provide the necessary power.

Table 5.8: Fuel consumption for 60 VDI cycles

Case No	**Engine state duration**		**Fuel Consumption**		**Total equivalent fuel**
	ON	OFF	[kg/hr]	[L/hr]	[L/hr]
1	1864.0	1736.0	3806.29	4.56	4.22
2	1886.1	1713.9	3851.42	4.61	4.27
3	1865.3	1734.7	3808.90	4.56	4.25
4	1867.3	1732.7	3813.04	4.57	4.24
5	1865.0	1735.0	3808.33	4.56	4.23
6	1834.0	1766.0	3745.03	4.49	4.23
7	1763.0	1837.0	3600.05	4.31	4.23
8	1689.0	1911.0	3448.94	4.13	4.26
9	1592.7	2007.3	3252.23	3.89	4.24
Average					**4.24 L/hr**

The engine operating duration for 60 VDI cycles is determined from the simulation results, shown in Table 5.8, and the fuel consumption is directly proportional to the engine running duration for the cycle. The standard basis of forklift fuel consumption is determined by converting fuel consumption from kg/hr to L/hr for three simulation cases. Equivalent fuel

consumption for the cycle is computed by adding fuel utilized and fuel equivalent energy from the battery. The average value of fuel consumption for 60 VDI cycles is calculated as 4.24 L/hr with a standard deviation of 0.016 L/hr and 0.50 L/hr margin of error.

The total amount of urea consumption also depends on the engine running time, and calculation for the average urea consumption is included in Table H.3 of Appendix H. The consumption of urea-solution is generally compared based on fuel consumption, which is typically 2% of the total fuel utilized [90]. Urea consumption percentage is computed based on fuel consumption and urea consumption during the cycle. The average urea solution consumption is 0.76% of diesel fuel consumption. For this study, NH_3 is directly injected to utilize the available model instead of a urea solution that must go through thermal decomposition and hydrolysis. Urea solution for the calculation is computed from the amount of NH_3 injected for NOx reduction and considering both reactions elaborated in Appendix H. For calculation purposes, it has been assumed that urea solution is converted entirely to NH_3 and H_2O without any intermediate compound. So, 0.76% of urea consumption can be considered reasonable.

5.9. Energy Utilization in VDI 2198 cycle

The energy utilization in VDI 2198 cycle for the developed series hybrid powertrain is evaluated in this section. The total energy generated from the fuel, battery, and regenerative braking is mainly utilized by traction motor and hydraulic motor. The traction motor provides the necessary power for vehicle drag and rolling resistance while hydraulic motor provides necessary power for lifting load, steering, and braking. There are different losses associated with battery, electromechanical conversion in electric motor and generator, efficiency of an engine, and transmission efficiency that accounts for energy utilization.

The summary of energy utilization in VDI 2198 cycle is presented in Table 5.9 and Figure 5.14. The total energy required for 60 VDI 2198 cycle after accounting for losses due to

engine deficiency and electromechanical deficiency of generator is equivalent to 14.43 kW-hr. The portion of total energy utilized by rolling resistance is 5.90 kW-hr while energy usage for vehicle drag is only 0.01 kW-hr. The energy utilized for vehicle rolling resistance is about 40.9% as the total mass, including vehicle mass, and the rated load is large. The energy utilization for the drag is minimal due to low vehicle speed in the VDI cycle.

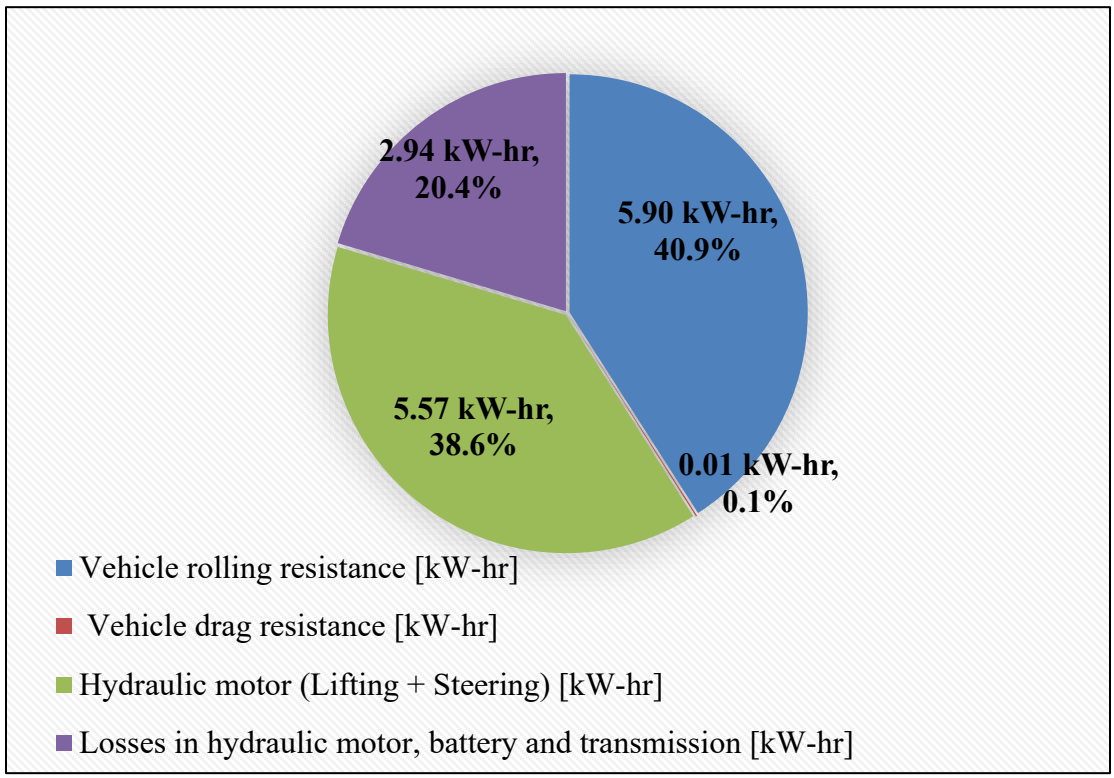

Figure 5.14: Pie-chart showing energy consumption in the VDI cycle for the designed series hybrid forklift

The energy utilization for lifting load and steering is equivalent to 5.57 kW-hr. This energy is about 38.6% of the total energy that is consumed by the hydraulic motor. The additional losses in the hydraulic motor, battery, inverter/converter, and transmission are 3.55 kW-hr equivalent to 20.4% of the total energy. Therefore, the total energy consumption for the cycle can be further reduced by using the more efficient electrical components, including the battery, inverter/converter, and electric motor.

Table 5.9: Energy utilization in 60 VDI 2198 cycles for a series hybrid forklift

Parameters	**Energy utilization [kW-hr]**	**Energy utilization percentage**
Vehicle rolling resistance	5.90	40.9%
Vehicle drag resistance	0.01	0.1%
Hydraulic motor (Lifting + Steering)	5.57	38.6%
Losses in hydraulic motor, battery, inverter/converter and transmission	2.94	20.4%
Total energy (battery + eng/gen + regenerative raking)	**11.43**	**100%**

5.10. Comparison of Fuel Consumption and Energy Utilization for Different Vehicles

The fuel consumption of conventional forklifts provided in the manufacturer datasheets is utilized to compare fuel consumption for 60 VDI 2198 cycles. The service weight and rated load of vehicles are taken into consideration for simulation, and other engines, after-treatment, and powertrain parameters are kept the same. Since the rated load profile of 5000 kg was only available for the hydraulic load, the scale factor of 0.9 is used to simulate for 4500 kg rated load. For both the rated load similar engine was used [91], so the vehicle performance for 4500 kg rated load is also evaluated. There might be many differences in the design of vehicles, which is not considered for this comparison. Fuel consumption available for three vehicles is compared with the simulation result and the data provided by the manufacturer's datasheet. The fuel consumption for the series hybrid powertrain is computed in a similar manner discussed in Section 5.8.

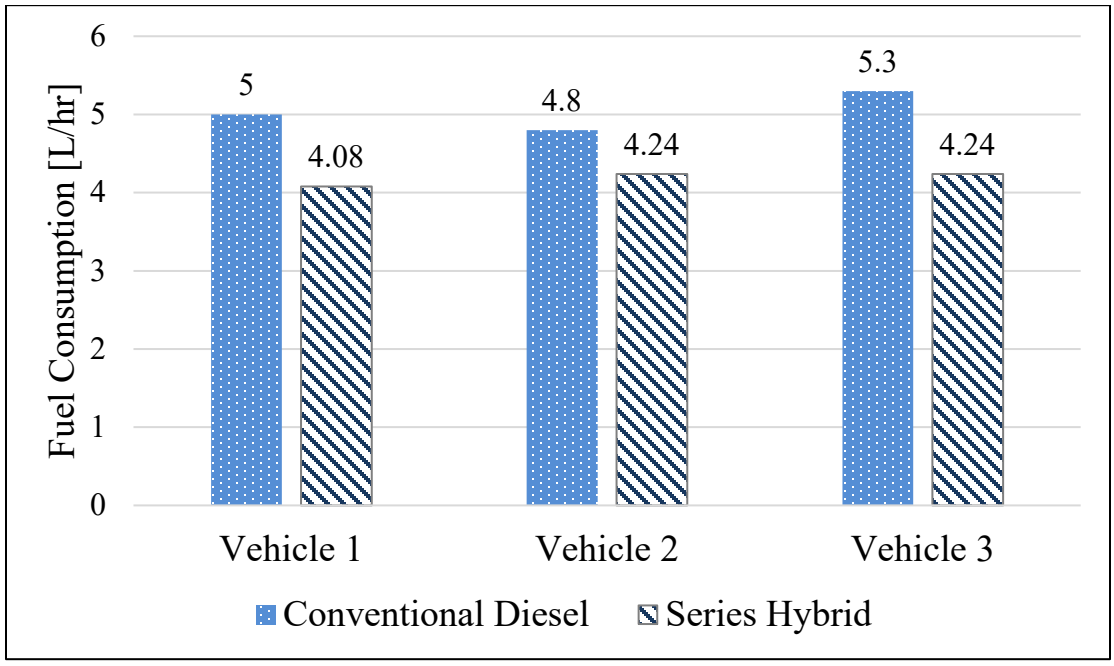

Figure 5.15: Comparison of fuel consumption for conventional and series hybrid forklift in VDI cycle

Figure 5.15 shows the result of fuel comparison for three vehicles using the conventional diesel engine and a series hybrid powertrain in the VDI 2198 cycle. The results in Table 5.10 shows 18.4% fuel consumption benefits for vehicle 1 and 20% for vehicle 3, while only 11.7% fuel consumption benefits for vehicle 2. The reason behind fuel consumption difference is vehicle 1, and vehicle 3 is manufactured by the same OEM, while vehicle 2 is made by different OEM. Each vehicle uses different engines with different performances. Furthermore, the control strategies for traction and hydraulic lift energy management could also be different, resulting in fuel consumption discrepancy.

The energy utilization for the different vehicles using a series hybrid powertrain is evaluated for the VDI 2198 cycle following the similar procedure mentioned in Section 5.9. The calculated results for energy utilization are included in Table 5.11. The rolling resistance for vehicle 3 has maximum value as the vehicle mass is high; thus, the rolling resistance is larger than the other two, and the drag for all forklifts are almost similar. The

energy utilization for the hydraulic motor is identical for vehicle 2 and vehicle 3 as both use the same hydraulic load profile. The rated load of vehicle 1 is only 4500 kg, so the energy utilization by the hydraulic motor is also comparatively less. The total losses in the battery, inverter/converter, and transmission for vehicle 1 is equivalent to 25.03%, which is relatively higher than the total losses in vehicle 2 and vehicle 3.

Table 5.10: Comparison of fuel consumption with available vehicle data

Vehicle specification	**Vehicle weight [kg]**	**Rated load [kg]**	**Fuel consumption VDI 60 cycle [L/h]**		**Fuel consumption difference [%]**
			Conventional diesel	Series hybrid	
Vehicle 1 [92]	6690	4500	5.0	4.1	18.4
Vehicle 2 [91]	7174	5000	4.8	4.2	11.7
Vehicle 3 [92]	7220	5000	5.3	4.2	20.0

Table 5.11: Energy utilization for the different vehicles using a series hybrid powertrain

Parameters	**Vehicle 1**		**Vehicle 2**		**Vehicle 3**	
	[kW-hr]	[%]	[kW-hr]	[%]	[kW-hr]	[%]
Rolling resistance	5.37	38.74	5.84	40.50	5.87	40.63
Drag resistance	0.01	0.09	0.01	0.09	0.01	0.09
Hydraulic motor (Lifting + Steering)	5.01	36.14	5.57	38.58	5.57	38.56
Losses hydraulic motor, battery, inverter/converter and transmission	3.47	25.03	3.01	20.84	2.99	20.72
Total energy	13.86	100	14.43	100.00	14.44	100

5.11. Cost Comparison for the Conventional Diesel and a Series Hybrid Forklift in VDI 2198 Cycle

Table 5.12: Cost saving for the forklift in a year using a series hybrid powertrain

Vehicle specification	Fuel saving in an hour [L/h]	Fuel saving in a year [L]	Total cost saving [$]
Vehicle 1	0.92	1148.16	3548
Vehicle 2	0.56	698.88	2160
Vehicle 3	1.06	1322.88	4088

*Cost of diesel = $ 3.09/L [93]

Table 5.12 shows the cost benefits from fuel-saving that can be achieved using a series hybrid powertrain forklifts over the conventional diesel engine forklifts. Some assumption accounted for the cost calculation are mentioned below:

- forklift normal operation cycle is similar to VDI 2198 cycle,
- forklift operates for 60% of the 8-hours shift in a day for 260 days in a year [94].

The total cost saving from the fuel consumption is evaluated for these three vehicles when a series hybrid powertrain is implemented. The cost benefits is evaluated as $3548, $2160 and $4088 for vehicle 1, vehicle 2, and vehicle 3, respectively in a year. So, it can be concluded that a diesel series hybrid with an engine operating at a single point is a suitable approach that would reduce fuel consumption and operation cost compared to the conventional diesel engine forklifts.

Chapter 6: Conclusion and Future Works

6.1. Conclusion

This thesis aimed to investigate into optimal engine and after-treatment for a series hybrid forklift. This work is entirely done in GT-power simulation environment. In this research project, GT-Suite® holistic engine model is developed, which is coupled with the after-treatment system for diesel series hybrid forklift Application. The results and summary of the finding from this work are described in the following points:

- The diesel engine is validated against the available experimental data with an error of 0.3% and 1.81% for BSFC and BSNOx, respectively. The validated engine model is then optimized for a single point at 2000 RPM and 35 kW load with the critical operating parameters including AFR, EGR, injection timing, boost pressure, injection pressure, and compression ratio.
- AFR relative sensitivity is comparatively higher for both engine performance parameters as BSFC and BSNOx. So, iso-BSNOx optimization is carried out that would target BSNOx emission to a desired value for every case, keeping injection pressure constant at 1400 bar. Moreover, exhaust gas temperature also has a vital role in the conversion efficiency of the after-treatment components. Therefore, engine optimization is carried out for Iso-BSNOx emission of 3gm/kW-hr and 4gm/kW-hr that would lead to exhaust gas temperature around 470^0 C at the turbine inlet.
- $BSNO_x$ 4gm/kW-hr provided better fuel economy without much difference in exhaust gas temperature. So, it was chosen as an operating point considering the required emission target.
- After-treatment model available in GT power is studied, and the best model suitable for the current application is designed. Along with that urea controller strategy is

modeled for optimal NOx conversion and urea consumption. Effect of changing DOC and DPF length for different exhaust gas temperature is analyzed, and the optimal length was chosen so that HC conversion efficiency is greater than 90% and NO_2/NOx ratio at SCR inlet is around 0.5. Along with that, PN count in the DPF must be as low as $1*10^{12}$ /kW-hr.

- Performance of different SCR catalysts such as Cu-Chabazite, Fe-zeolite, and their combination in series is analyzed for different exhaust gas temperatures. Fe-zeolite catalyst is found to be a better choice for this operating point since it provides better efficiency at a temperature above 350^0 C. Furthermore, the effect of changing Fe-zeolite catalyst length and exhaust gas temperature on NOx conversion efficiency and urea consumption was studied to determine optimal length of the catalyst that would provide conversion efficiency more than 90% at steady-state operating conditions.
- Cold start of an engine operating at a single point is studied coupling the engine and after-treatment systems. The tail-pipe NOx emission is especially higher during cold start as the SCR catalyst takes a certain duration to attain light-off temperature. So, to achieve the catalyst light-off temperature faster, the effect of retarding injection timing and late post-injection is studied. The tail-pipe NOx emission is cut-off by 40% with negligible increase in soot emission for retarding main injection timing by 15 deg. CA, while the rise in hydrocarbons emission is observed for late post-injection even though NOx emission benefit is higher compared to retarding injection timing.
- Performance of a series hybrid forklift is analyzed modeling the key electric power-train components like the battery, traction motor, and generator with appropriate controller strategies. The vehicle model for a forklift that could handle 5000 kg load is provided by IAV GmbH, and VDI 2198 cycle is used to evaluate fuel consumption and urea consumption of the developed powertrain.

- Energy recuperated during regenerative braking in a VDI cycle and performance of the battery is also assessed for the constant peak load. The forklifts acceleration profile in VDI cycle shows a lot of regenerative opportunities, and it is possible to recapture almost all energy via regenerative braking as deceleration is less than -2 m/s^2. The total energy recovered during 60 VDI cycles is equivalent to 0.18 L of diesel fuel using a series hybrid powertrain.
- Energy utilization and losses for the series hybrid forklifts is evaluated and the results show 40.9% of the total available energy is used for the vehicle rolling resistance, and the hydraulic motor utilizes 38.6% for lifting load and steering. The losses in the hydraulic motor, battery, and transmission is equivalent to 20.4%, while the vehicle drag resistance is negligible as the vehicle velocity is low in VDI cycle.
- Cost benefits due to the reduction of catalyst size for single point operating engine is evaluated. The cost benefits percentage of DOC and DPF is more than 10% higher compared to SCR. However, the overall cost reduction in SCR is $131 as SCR is the most expensive among the three components. The cost of urea-SCR components is determined mainly by the cost of urea dosing and controller mechanism than the cost of catalyst.
- Fuel consumption of the conventional forklift is compared to the designed forklift operating with a series hybrid architect, which shows fuel consumption reduction up to 20% and cost-saving up to $4088 in a year.

6.2. Future Works

The following can be considered for continuation of this research

- Modeling of the hydraulic lift component to accurately predict the energy required during lifting and study the opportunity of regenerative energy from the lift motor as well.

- Implementation of an optimum control strategy for the hybrid power train and compare benefits in fuel consumption for the different strategies.
- Design and implementation of the iterative learning control/optimization for developing an optimal control strategy since the lift-truck might operate on different cycle, and not necessarily running on the VDI 2198 cycle studied in this thesis.
- Implementation of variable valve timing can be considered as design parameters for engine optimization.
- Defining an additional operating point for active regeneration in DPF which will be required after an engine is operated for the longer duration.
- Implementation of the thermal heating model of electrical components to define a control strategy more precisely
- Implementation of separate operating points can be considered for cold start and for certain lift-truck maneuvering with special power demand

References

[1] Heidari, B., and Marr, L. C., (2015), "Real-Time Emissions from Construction Equipment Compared with Model Predictions," *Journal of the Air & Waste Management Association*, **65**(2), 115-125.

[2] Variant Market Research., 2016. Construction Equipment Market Overview https://www.variantmarketresearch.com/report-categories/energy-mining/construction-equipment-market/. Accessed on July 10, 2019 [Online].

[3] Faust, B., 2015. Forklift Conversion: The Key to Eco-Efficiency, https://www.manufacturing.net/article/2015/01/forklift-conversion-key-eco-efficiency/. Accessed on July 12, 2019 [Online].

[4] Markets and Markets., 2017, Forklift Market by Application. https://www.marketsandmarkets.com/Market-Reports/forklift-market-2439790.html Accessed on July 12, 2019 [Online].

[5] DieselNet., 2017, EU: Nonroad Engines https://www.dieselnet.com/standards/eu/nonroad.php. Accessed on May 12, 2019 [Online].

[6] Technical Committee CEN/TC 150, 2013, " Energy Efficiency of Industrial Trucks — Test Methods — Part 1," TC 150 WI: 2013.

[7] Jonasson, K., 2005, "Control of Hybrid Electric Vehicles with Diesel Engines," PhD Thesis, Lunds University, Department of Industrial Electrical Engineering and Automation.

[8] Retail Logistics International, 2019, Are you ready for Euro-Stage V https://www.sustainablelogisticsinternational.com/are-you-ready-for-euro-stage-v/. Accessed on July 23, 2019 [Online].

[9] Ogawa, K., Futahashi, K., Teshima, T., and Akahane, F., 2010, "Development of the World's First Engine/Battery Hybrid Forklift Truck," *Mitsubishi Heavy Industries Technical Review*, **47**(1), p.46

[10] Kim, S., Choi, S., Lee, J., Hong, S., and Yoon, J., 2013, "A Study of Hybrid Propulsion System on Forklift Trucks," *World Electric Vehicle Symposium and Exhibition*, pp. 1-8.

[11] Conte, M., Genovese, A., Ortenzi, F. and Vellucci, F., 2014, "Hybrid Battery-Supercapacitor Storage for an Electric Forklift: A Life-cycle Cost Assessment," *Journal of Applied Electrochemistry,* **44**(4), pp. 523-532.

[12] Keränen, T.M., Karimäki, H., Viitakangas, J., Vallet, J., Ihonen, J., Hyötylä, P., Uusalo, H. and Tingelöf, T., 2011, "Development of Integrated Fuel Cell Hybrid Power Source for Electric Forklift," *Journal of Power Sources,* **196**(21), pp. 9058-9068.

[13] Hosseinzadeh, E., Rokni, M., Advani, S.G. and Prasad, A.K., 2013, "Performance simulation and analysis of a fuel cell/battery hybrid forklift truck," *International Journal of Hydrogen Energy,* **38**(11), pp. 4241-4249.

[14] The International Council on Clean Transportation, 2012, "Estimated Cost of Emission Reduction Technologies for Light-Duty Vehicles," Washington DC (USA)

[15] Mallamo, F., Badami, M., and Millo, F., 2002,"Analysis of Multiple Injection Strategies for The Reduction Of Emissions, Noise and BSFC of a DI CR Small Displacement Non-Road Diesel Engine," *SAE Transactions,* pp. 1119-1130.

[16] Agarwal, A.K., Srivastava, D.K., Dhar, A., Maurya, R.K., Shukla, P.C., and Singh, A.P., 2013, "Effect of Fuel Injection Timing and Pressure on Combustion, Emissions and Performance Characteristics of a Single Cylinder Diesel Engine," *Fuel,* **111**, pp. 374-383.

[17] Nakagome, K., Shimazaki, N., Niimura, K., and Kobayashi, S., 1997, "Combustion and Emission Characteristics of Premixed Lean Diesel Combustion Engine," *SAE transactions*, pp.1528-1536

[18] DieselNet., 2017. Fuel Injection for Clean Diesel Engines*,* Available: https://www.dieselnet.com/tech/engine_fi.php/. Accessed on May 5, 2019 [Online]

[19] Wattrus, M., 2013, "Fuel Property Effects on Oil Dilution in Diesel Engines", *SAE International Journal of Fuels and Lubricants*, **6**(3), pp.794-806.

[20] Dallmann, T., Posada, F., and Bandivadekar., 2018, "Costs of Emission Reduction Technologies for Diesel Engines Used in Non-Road Vehicles and Equipment," *The International Council on clean Transportation*, Working Paper 2018-10.

[21] Reifarth, S., 2010, "EGR-systems for Diesel Dngines," PhD thesis, KTH Industrial Engineering and Management.

[22] Yokomura, H., Kohketsu, S., and Mori, K., 2003. "EGR System in a Turbocharged and Intercooled Heavy-Duty Diesel Engine–Expansion af EGR Area with Venturi EGR System," *Technical Review*, **15**, pp.14-20.

[23] Barman, J., Ghodke, P., and Joseph, J., 2011, “Evaluation of Intercooler Efficiency as a Technique for Reducing Diesel Engine Emissions,” SAE Technical Paper 2011-01-1133.

[24] Tanin, K.V., Wickman, D.D., Montgomery, D.T., Das, S., and Reitz, R.D., 1999, “The Influence of Boost Pressure on Emissions and Fuel Consumption of a Heavy-Duty Single-Cylinder DI Diesel Engine,” *SAE transactions,* pp. 1198-1219.

[25] DieselNet., 2016. Turbocharging Challenges*,* https://www.dieselnet.com/tech/air_turbo_challenge.php/. Accessed on May 5, 2019 [Online]

[26] Summit Handling Systems Inc., 2015, Toyota’s New 1ZS Diesel Engine https://www.summithandling.com/toyotas-1zs-diesel-engine/. Accessed on June 12, 2019 [Online]

[27] Kurre, S.K., Pandey, S., and Saxena, M., 2013. “Effect of Compression Ratio on Diesel Engine Performance and Emission with Diesel-Ethanol Blends,” *International Journal of Scientific & Engineering Research*, **4**(10), pp.775-779.

[28] Millington, B.W., and Hartles, E.R., 1968. “Frictional Losses in Diesel Engines,” *SAE Transactions*, pp.2390-2410.

[29] Valentino, G., Corcione, F.E., Iannuzzi, S.E., and Serra, S., 2012, "Experimental Study on Performance And Emissions of a High Speed Diesel Engine Fuelled with N-Butanol Diesel Blends under Premixed Low Temperature Combustion," *Fuel,* **92**(1), pp. 295-307.

[30] Man, X.J., Cheung, C.S., Ning, Z., Wei, L., and Huang, Z.H., 2016, “Influence of Engine Load and Speed on Regulated and Unregulated Emissions of a Diesel Engine Fueled with Diesel Fuel Blended with Waste Cooking Oil Biodiesel,” *Fuel*, **180**, pp.41-49.

[31] DieselNet., 2017, United States: Nonroad Diesel Engines https://www.dieselnet.com/standards/us/nonroad.php/. Accessed on April 10, 2019 [Online].

[32] DieselNet., 2017, ISO 8178 https://www.dieselnet.com/standards/cycles/iso8178.php/. Accessed on April 10, 2019 [Online].

[33] Posada, F., Bandivadekar, A., and German, J., 2013, “Estimated Cost of Emission Control Technologies for Light-Duty Vehicles Part 2-Diesel,” SAE Technical Paper 2013-01-0539.

[34] Girard, J., Cavataio, G., Snow, R. and Lambert, C., 2009, “Combined Fe-Cu SCR Systems with Optimized Ammonia to NOx Ratio for Diesel Nox Control,” *SAE International Journal of Fuels and Lubricants*, **1**(1), pp.603-610.

[35] Zhang, Z., Yang, S.L., and Johnson, J.H., 2002, “Modeling and Numerical Simulation of Diesel Particulate Trap Performance during Loading and Regeneration,” *SAE Transactions*, pp.471-483..

[36] Watanabe, T., Kawashima, K., Tagawa, Y., Tashiro, K., Anoda, H., Ichioka, K., Sumiya, S., and Zhang, G., 2007, "New DOC for Light Duty Diesel DPF System," SAE Technical Paper 2007-01-1920.

[37] International Council on Clean Transportation, 2016, "European Stage V Non-Road Emission Standards," Policy Update

[38] DieselNet., 2019, Diesel Particulate Filters, https://www.dieselnet.com/tech/dpf.php. Accessed on April 10, 2019 [Online].

[39] Tandon, P., Heibel, A., Whitmore, J., Kekre, N., and Chithapragada, K., 2010, "Measurement and Prediction of Filtration Efficiency Evolution of Soot Loaded Diesel Particulate Filters," *Chemical Engineering Science*, **65**(16), pp.4751-4760.

[40] Jiao, P., Li, Z., Shen, B., Zhang, W., Kong, X., and Jiang, R., 2017, "Research of DPF Regeneration with NOx-PM Coupled Chemical Reaction," *Applied Thermal Engineering*, **110**, pp.737-745.

[41] Dou, D., 2012. "Application Of Diesel Oxidation Catalyst and Diesel Particulate Filter for Diesel Engine Powered Non-Road Machines," *Platinum Metals Review*, **56**(3), pp.144-154.

[42] Thill. K., 2013, Tier 4 Emissions: What is that?, https://www.toyotaequipment.com/tier-4/. Accessed on July 7, 2019 [Online].

[43] Krocher, O., and Elsener, M., 2008, "Combination of V_2O_5/WO_3-Tio_2, Fe− ZSM5, and Cu− ZSM5 Catalysts for The Selective Catalytic Reduction of Nitric Oxide with Ammonia," *Industrial & Engineering Chemistry Research*, **47**(22), pp. 8588-8593.

[44] Metkar, P.S., Harold, M.P., and Balakotaiah, V., 2013. "Experimental and Kinetic Modeling Study of NH_3-SCR Of NOx on Fe-ZSM-5, Cu-Chabazite and Combined

Fe-And Cu-Zeolite Monolithic Catalyst,". *Chemical Engineering Science*, **87**, pp.51-66.

[45] Song, X., 2013. "A SCR Model Based on Reactor and Engine Experimental Studies for a Copper-Zeolite Catalyst," PhD Thesis, Michigan Technological University.

[46] Herman, A., Wu, M.C., Cabush, D., and Shost, M., 2009, "Model Based Control of SCR Dosing and OBD Strategies with Feedback from NH_3 Sensors," *SAE International Journal of Fuels and Lubricants*, **2**(1), pp.375-385.

[47] Willems, F., Cloudt, R., Van Den Eijnden, E., Van Genderen, M., Verbeek, R., de Jager, B., Boomsma, W., and van den Heuvel, I., 2007, "Is Closed-Loop SCR Control Required to meet Future Emission Targets?," SAE Technical Paper, 2007-01-1574.

[48] Agarwal, S., Olson, M., Meehan, T., and Wadwankar, N., 2015, "Fuel Economy Comparison Studies of Forklift Transmission Architecture," SAE Technical Paper 2015-01-2830.

[49] Ehsani, M., Gao, Y., Longo, S., and Ebrahimi, K., 2018. *Modern Electric, Hybrid Electric, and Fuel Cell Vehicles, Chapter 5*, CRC Press.

[50] Kumar, L., and Jain, S., 2014, "Electric Propulsion System for Electric Vehicular Technology: A Review," *Renewable and Sustainable Energy Reviews*, **29**, pp.924-940.

[51] European Comission, 2018, "Li-Ion Batteries for Mobility and Stationary Storage Applications," JRC Science for Policy Report.

[52] epec Engineering Technologies, 2019, Battery Cell Comparison https://www.epectec.com/batteries/cell-comparison.html/. Accessed on May 05, 2019 [Online]

[53] Dezza, F.C., Musolino, V., Piegari, L., and Rizzo, R., 2018. "Hybrid Battery–Supercapacitor System for Full Electric Forklifts," *IET Electrical Systems in Transportation*, **9**(1), pp.16-23

[54] Alahmer, A., Yamin, J., Sakhrieh, A., and Hamdan, M.A., 2010, "Engine Performance Using Emulsified Diesel Fuel," *Energy Conversion and Management*, **51**(8), pp.1708-1713.

[55] Volcano Eclectric., 2019. Electric Forklift http://www.volcanomotor.com/solutions/electric-forklift-en.html/ Accessed on July 16, 2019 [Online].

[56] Ryan, J.L., and Ryan, L.D., 2006, *The Forklift Manual, Chapter 2*, Donegal Bay Inc. Publishing.

[57] Nitin Subramonium, A.K., Shetty, P., Saravanan, G., and Vivekanandan, S., "Technology and Key Strategy of IE4 Permanent Magnet Brushless DC Motor Drive for Electric Vehicle Application," *Int. Journal of Engineering Research and Application,* **7**(2), pp. 25-31.

[58] Irwin, J.D., 1997, *The industrial electronics handbook, Chapter 13*, CRC Press.

[59] Cerofolini, A., 2014, "Optimal Supervisory Control of Hybrid Vehicles," Dissertation thesis, Alma

[60] Kessels, J.T.B.A., Willems, F.P.T., Schoot, W.J., and Van Den Bosch, P.P.J., 2010, "Integrated Energy & Emission Management for Hybrid Electric Truck with SCR Aftertreatment," *2010 IEEE Vehicle Power and Propulsion Conference*, Lille, France.

[61] Geering, H.P., 2007, *Optimal control with engineering applications*, Springer.

[62] Wang, H., Huang, Y., Lv, C., and Khajepour, A., 2017, "A Global Optimal Energy Management System for Hybrid Electric Off-road Vehicles," *SAE International Journal of Commercial Vehicles,* **10**, pp. 524-531.

[63] Zajac, P., and Kwasniowski, S., 2017, "Modeling Forklift Truck Movement in The VDI Cycle and The Possibility Of Energy Recovery," *23rd International Conference on Engineering Mechanics*, Svratka, Czech Republic.

[64] Payri, R., F. J. Salvador, P. Martí-Aldaraví., and J. Martínez-López, "Using One-Dimensional Modeling to Analyse The Influence of The Use of Biodiesels on The Dynamic Behavior of Solenoid-Operated Injectors in Common Rail Systems: Detailed Injection System Model." *Energy Conversion and Management,* **54**(1), pp. 90-99.

[65] GT-SUITE®, 2019, *Engine Performance Application Manual*, Gamma Technologies LLC, Westmont, IL.

[66] Vijayakrishnan Venkateshmohan, M. K., 2015, "Predictive Diesel Combustion using DI-Pulse in GT-Power," CHALMERS UNIVERSITY OF TECHNOLOGY, Gothenburg, Sweden.

[67] Heywood, J. B., 1988, *Internal Combustion Engine Fundamentals, Chapter 11*, McGraw-Hill, New York.

[68] Morel, T., and Keribar, R., 1986 "Heat Radiation In DI Diesel Engines," *SAE International,* **95**, pp. 1141-1157.

[69] Morel, T., and Wahiduzzman, S., 1996, "Modeling of Diesel Combustion and Emissions," XXVI FISITA Congress, Praha.

[70] Lavoie, G.A., Ortiz-Soto, E., Babajimopoulos, A., Martz, J.B., and Assanis, D.N., 2013, "Thermodynamic Sweet Spot for High-Efficiency, Dilute, Boosted Gasoline Engines," *International Journal of Engine Research*, **14**(3), pp.260-278.

[71] GT-SUITE®, 2019, *Exhaust Aftertreatment Application Manual*, Gamma Technologies LLC, Westmont, IL.

[72] GT-SUITE®, 2019, *Catalyst Brick Template* (*GTISE Help*), Gamma Technologies LLC, Westmont, IL.

[73] Sampara, C.S., Bissett, E.J., and Chmielewski, M., 2008, "Global Kinetics For A Commercial Diesel Oxidation Catalyst with Two Exhaust Hydrocarbons," *Industrial & Engineering Chemistry Research*, **47**(2), pp.311-322.

[74] Lee, S.J., Jeong, S.J., Kim, W.S., and Lee, C.B., 2008, "Computational Study On The Effects of Volume Ratio of DOC/DPF and Catalyst Loading on The PM and Nox Emission Control for Heavy-Duty Diesel Engines," *International Journal of Automotive Technology*, **9**(6), pp.659-670.

[75] GT-SUITE®, 2019, *Reaction Mechanism* (*GTISE Help*)., Gamma Technologies LLC, Westmont, IL.

[76] Premchand, K.C., Johnson, J.H., and Yang, S.L., 2013, "Development of A 1-D Catalyzed Diesel Particulate Filter Model for Simulation of The Oxidation ff Particulate Matter and Gaseous Species during Passive Oxidation and Active Regeneration," SAE Technical Paper 2013-01-1574.

[77] GT-SUITE®, 2019, *Aftertreatment Tutorials*, Gamma Technologies LLC, Westmont, IL.

[78] GT-SUITE®, 2019, *Particulate Filter Template* (*GTISE Help*), Gamma Technologies LLC, Westmont, IL.

[79] GT-SUITE®, 2019, *Vehicle Driveline and HEV Application Manual*, Gamma Technologies LLC, Westmont, IL.

[80] GT-SUITE®, 2019, *Motor Generator Template (GTISE Help).* Gamma Technologies LLC, Westmont, IL.

[81] Zhou, M., Zhao, L., Zhang, Y., Gao, Z., and Pei, R., 2015. "Pure Electric Vehicle Power-Train Parameters Matching Based on Vehicle Performance," *International Journal of Control and Automation*, **8**(9), pp.53-62.

[82] GT-SUITE®, 2019, *Vehicle Controls (GTISE Help)*, Gamma Technologies LLC, Westmont, IL.

[83] Hyundai Forklift, 2016, Electric Counterbalance Trucks, https://www.hyundaiforkliftamericas.com/wp-content/uploads/2016/11/22-25-30-35BH-9-1.pdf/ Accessed on June 10, 2019 [Online].

[84] Skogestad, S., 2003, "Simple Analytic Rules for Model Reduction and PID Controller Tuning," *Journal of Process Control*, **13**(4), pp.291-309.

[85] GT-SUITE®, 2019, *Optimization (GTISE Library)*, Gamma Technologies LLC, Westmont, IL.

[86] Ansari, E., 2017. "Combustion, Emissions, and Performance Optimization in a DI/PFI-RCCI Diesel/Natural Gas Turbocharged Engine," PhD thesis, Mechanical Engineering, Michigan Technological University.

[87] Toyota Material Handling, 2018, Electric Powered Forklift 4.0-5.0 ton, https://www.forkliftcenter.com/forklifts/files/1080-Toyota7FMBF45GBTB-3731-a4h.pdf/ Accessed on June 20, 2019 [Online].

[88] Higen Motor, 2017, Electric Vehicle Motor, http://www.higenmotor.com/en/bbs/download.asp?job=1&filename=ev%20catalogue%20(english)_2.pdf&no=420&lang=eng/ Accessed on May 5, 2019 [Online].

[89] ICF, II., 2014, "Diesel Generators: Improving Efficiency and Emission Performance in India," *Shakti Sustainalble Energy Foundation.*

[90] GT-SUITE®, 2019, *Application* (*GTISE Library*), Gamma Technologies LLC, Westmont, IL.

[91] Cummins Filtration, 2009, Diesel Exhaust Fluid (DEF) Q &. https://www.cumminsfiltration.com/sites/default/files/MB10033.pdf/. Accessed on June 30, 2019 [Online].

[92] STILL, 2018, RX 70 Techincal Data Diesel and LPG Forklift Trucks, https://data.still.de/assets/products/Vehicles/Diesel_And_LP_Gas_Forklift_Trucks/RX_70_40-50/pdfs/RX_70_40_50_EN_2018_TD_web.pdf?mod=1519653572&download=1&s=3dde970c404aa2d39cc3b971994bbc41 Accessed on June 25, 2019 [Online].

[93] T.oyota Material Handling, 2018, Engine Powered Forklift 3.5 - 8.0 ton https://qpsearch.bt-forklifts.com/PDFSearch/GetPDF.asp?artno=745567-040. Accessed on June 23, 2019 [Online].

[94] U. S. E. I. Administration., 2019, Gasoline and Diesel Fuel Update, https://www.eia.gov/petroleum/gasdiesel/. Accessed on 7/28/2019 [Online].

[95] M. F. Trucks, 2019, Mitsubishi Forklift Briefing https://forkliftbriefing.com/save-money/the-forklift-fuel-robbery/. Accessed on June 13, 2019 [Online].

[96] GT-Suite®, 2014, "Predictive Combustion Modeling," *Gamma Technologies LLC*.

[97] Livengood, J. C., and P. C. Wu., 1995, "Correlation of Autoignition Phenomena in Internal Combustion Engines and Rapid Compression Machines," In *Symposium (International) on Combustion*, **5**(1) pp. 347-356.

Appendix A. Predictive Combustion Model

The predictive DI combustion model is defined in GT-Power using DI-pulse combustion model in which the following multiplier must be calibrated

A.1 Entrainment Rate Multiplier

This parameter is calculated based on conservation of momentum [95] which is represented by the following Equations

Rate of entrained fuel-gas mixture:

$$\frac{dm}{dt} = -C_{ent} * m_{inj.} * u_{inj} * \frac{du}{dt} \quad \text{(A-1)}$$

$$u = \frac{dS}{dt} \quad \text{(A-2)}$$

$$u_{inj} = C_d \sqrt{\frac{2\Delta P}{\rho_l}} \quad \text{(A-3)}$$

where,

m_{inj} is initial mass of injected fuel packet

u_{inj} is the injection velocity at the injector nozzle tip

C_{ent} is the entrainment multiplier used for calibration

S is the spray penetration length of a pulse at a time 't'

ρ_l is the density of the liquid fuel

ΔP is the pressure difference across the injector nozzle

C_d is the coefficient of discharge of the injector nozzle

A.2 Ignition delay multiplier

Ignition delay is the time between injection of fuel into the cylinder and start of fuel combustion. It is the function of EGR, bulk cylinder temperature and cetane number of the fuel [66] represented by the following Equations

$$\tau = C_{ign} * \rho^{C_{ign2}} * e^{\frac{C_{ign3}}{T}} \cdot f(EGR) \qquad \text{(A-4)}$$

where,

C_{ign} is the multiplier used for model calibration

Ignition delay is evaluated by the relation provided in [96], which is the function of pressure and temperature.

$$\int_{t_{soi}}^{t_{soi}+t_{id}} \frac{dt}{\tau(p,T)} = 1 \qquad \text{(A-5)}$$

A.3 Premixed combustion multiplier

Rate of premixed combustion mass is a function of the kinetic rate constant, temperature, air-fuel equivalence ratio, and EGR, which is represented in Equation below [95].

$$\frac{dm}{dt} = -C_{pm} * m * (t - t_{ign}) * f(k, T, \lambda, EGR) \qquad \text{(A-6)}$$

where,

C_{pm} is the premixed combustion rate multiplier

t is the time after injection event of the fuel packet,

t_{ign} is the injection delay

k is the kinetic rate constant for the combustion reaction ,

m is the mass of air-fuel mixture developed during the ignition delay period

λ is the air-fuel equivalence ratio

A.4 Diffusion Combustion Rate Multiplier

Rate of diffusion combustion mass is a function of EGR and oxygen concentration in the air-fuel mixture which is defined by Equation below [66]

$$\frac{dm}{dt} = -C_{df} * m * \frac{\sqrt{k}}{\sqrt[3]{V_{cyl}}} * f(EGR, [O_2]) \quad \text{(A-7)}$$

where,

V_{cyl} is the cylinder volume,

k is the kinetic rate constant,

$[O_2]$ is the oxygen concentration in the air-fuel mixture

m is the mass of the air-fuel mixture available at diffusion combustion stage

C_{df} is the diffusion combustion multiplier

These multipliers are calibrated using experimental data by IAV GmbH for a particular diesel engine which is being used in this study.

Appendix B. Extended Zeldovich Model

Reaction Mechanism for Extended Zeldovich mechanism used in GT power involves following reactions:

N_2 oxidation rate Equation:	$O + N_2 = NO + N$	(R1)
N oxidation rate Equation:	$N + O_2 = NO + O$ (2)	(R2)
OH reduction rate Equation:	$N + OH = OH + H$	(R3)

The reaction rates for R1, R2, and R3 reaction are represented by k1, k2 and k3 which are provided in [65]

$$k1 = F_1 * 7.60 * 10^{10} * e^{-38000*A_1/T_b} \quad \text{(B-1)}$$

$$k2 = F_2 * 6.40 * 10^{6} * T_b * e^{-3150*A_2/T_b} \quad \text{(B-2)}$$

$$k3 = F_3 * 4.10 * 10^{10} \quad \text{(B-3)}$$

where,

F_1 is N_2 oxidation rate multiplier

F_2 is N oxidation rate multiplier

F_3 is OH reduction rate multiplier

A_1 is N_2 oxidation activation energy multiplier

A_2 is N oxidation activation energy multiplier

T_b is burned sub-zone temperature (K)

Calibrated NOx model from the experimental data provided by IAV GmbH is used in this study to predict NO formation during combustion.

Appendix C. Convection Temperature Evaluation

The convective heat transfer rate between those burned and unburned zones is given by convection temperature evaluation represented by the following equations in GT-Suite® [65]

$$Q = Ah(T_g - T_w) \quad \text{(C-1)}$$

$$Q = Ah(T_g - T_w) \quad \text{(C-2)}$$

where,

Q is convective heat transfer rate [W]

A is surface area [m^2]

h is the convective heat transfer coefficient [W/m^2K]

T_w is wall temperature [K]

T_g is effective gas temperature [K]

T_u is unburned zone temperature

α is a weighting coefficient

Appendix D: Calculation of Urea-solution Amount from the Injected Mass of NH_3

NH_3 is generated by urea decomposition. The reactions involved in urea decomposition are thermal decomposition and hydrolysis reaction which are as follows

Thermal decomposition:

$$(NH_2 - CO - NH_2)_{aq} \rightarrow NH_{3(g)} + HNCO_g \quad \text{(D-1)}$$

Hydrolysis reaction:

$$HNCO_{(g)} + H_2O_{(aq)} \rightarrow NH_{3(g)} + CO_{2(g)} \quad \text{(D-2)}$$

Urea solution contains 32.5% urea and 67.5% water [90]

1 mole of urea = 60.06 gm

1 mole of water = 18.015 gm

1mole of NH_3 = 17 gm

Considering NH_3 generation from urea is 100% efficient. The mass of urea can be computed using back-calculation shown in the following steps.

- 2 moles of ammonia is produced by 1 mole of urea
- 1 mole of urea solution = 0.325*60.06 + 0.675*18.015 = 31.68 gm
- 1 mole of urea is obtained from (31.64/0.325 = 97.48) gm of urea solution
- Urea mass flow rate = 2.867*(mass flow rate of NH_3)

Appendix E: Battery Sizing Calculation

Battery parameters are calculated by the following procedure:

Power capacity of battery:

$P_{battery} = \frac{P_{motor}}{\eta_{motor}} - P_{e/g}$ = 90/0.95 -31.5 = 65 kW (approx..)

Energy/Power ratio of Li-ion battery = 0.1 h [49]

Cell capacity = 7 Ah

Required battery capacity = $P_{battery}/0.1$ = 65 kW-hr

Nominal voltage of battery : 3.3 V

Battery Voltage : 3.3* $N_{sereies}$ = 3.3*97 = 320 V

$N_{parallel} = \left(\frac{6500}{320*7}\right)$ = 2.9 = 3

Battery capacity = 3*7*320 = 6.72 kWh

Appendix F: Cost Estimation of the After-treatment Components

The cost estimation of after-treatment components for DOC, DPF, and SCR are tabulated in Table F.1, Table F.2, and Table F.3, respectively. The cost of the after-treatment components for conventional diesel engine and the reduced size are calculated based on the empirical formula provided in the reference. [20].

Table F.1: Cost comparison for the DOC components

Application	Conventional engine	Hybrid
Engine displacement [L]	2.0	2.0
Catalyst volume, CV (SVR=0.7)	1.4	1.0
Pt cost, 0.94g/L * CV * $30/g	$39	$27
Pd cost, 0.47 g/L x CV x $30/g	$20	$14
Total PGM cost	$59	$41
Substrate ($6.0*CV)	$8	$6
Wash coat ($13*CV)	$18	$13
Total PGMs+ wash coat + substrate	$86	$59
Canning ($5*CV)	$7	$5
Accessories	$17	$15
Total Manufacturing	$103	$74

** SVR = Sweep volume ration

** CV = Catalyst volume

Table F.2: Cost comparison for the catalyzed DPF components

Application	Conventional engine	Series Hybrid
Engine displacement [L]	2	2
Catalyst volume, CV (SVR=2.0)	4	2.33
Pt cost, 2/3*0.2g/L * CV * $31/g	$17	$10
Pd cost, 1/3*0.2 g/L x CV x $7/g	$7	$4
Total PGM	$24	$14
Substrate ($23*CV)	$92	$54
Wash coat ($10*CV)	$40	$23
Total PGMs+ washcoat + substrate	$156	$91
Canning ($5*CV)	$20	$12
Accessories	$10	$22
Regeneration system	$81	$81
Total Manufacturing	$247	$193

Table F.3**:** Cost comparison for SCR components

Application	**Conventional engine**	**Series Hybrid**
Engine displacement	2	2
Catalyst volume, CV (SVR=2.0) litres	4	0.943
NH3 slip catalyst	$3	$3
Pt, Pd, and Rh are not required for NOx control	0	$0
Total PGM	$3	$3

Substrate and washcoat (Zeolites: $18/L*CV)	$72.00	$16.97
Canning (25*CV)	$100.00	$23.58
PGMs+ wash coat + substrate	$175	$43
Urea tank volume (6*Vd), liters	$12	$12
Tank accessories	$30	$30
Urea tank cost	$85	$85
Urea level sensor	$48	$48
Urea pump	$49	$49
Urea injector	$33	$33
Tubing stainless steel	$14	$14
Urea injection mounting parts	$15	$15
Urea Injection pipe section	$14	$14
Urea heating system -200W, 12 V DC	$38	$38
Temperature sensors (x2)	$84	$84
Dosing control unit	$200	$200
Urea mixer	$20	$20
Total manufacturing cost	$817	$685

** The empirical formulas for the components of the urea dosing system is not provided in the reference. Therefore, cost of urea dosing components for 1.7 L diesel is used without any adjustment to compute the total manufacturing cost.

Appendix G: Energy Recuperated in Regenerative Braking

The energy recuperated during five VDI cycles is computed using integration block in GT-Suite®. The OCV of battery and negative terminal current are multiplied to obtain instantaneous power, which is integrated to determine total recuperated energy. The total energy recuperated during in 5 VDI cycle for two cases are tabulated in Table G.1

Table G.1: Parameters used for regenerative braking calculation

BSFC of engine	209.88 gm/kW-hr
Generator efficiency	0.9
Inverter efficiency	0.95
1 L of diesel Fuel	3.40 kW-hr
Density of diesel fuel	0.835 kg/L

The amount of energy that will be provided by fuel considering losses in engine, generator, and inverter is given by:

1 L Fuel equivalent = (1000/209.88)*0.9*0.95*0.835 = 3.4 kW-hr

The total energy recuperated for 60 VDI cycles :

= 12 * Average energy recuperated in 5 drive cycle(kW-hr)

Appendix H: Fuel and Urea Consumption Calculation

Fuel and urea consumption for VDI cycle is calculated using the following Equations and parameters

Table H.1: Parameters used for calculation

Efficiency of generator	0.9
Efficiency of inverter	0.95
BSFC	209.88 gm/kW-hr
1 L of diesel equivalent energy	3.402 kW-hr
Fuel consumption rate	2.042 gm/sec
Density of diesel	835 kg/m^3
Density of urea	1085 kg/m^3
Battery capacity	6.72 kW-hr
Forklift operation in a day	60% of 8-hour shift per day
Forklift operation in a year	260 days/year
Cost of diesel fuel	$ 3.09 /L

- Energy provided by battery :

$$(\text{Initial SOC} - \text{Final SOC}) * \text{Battery Capacity}$$

- Fuel Equivalent energy in L/h : $\frac{\text{Energy Provided by battery}}{\text{1L of diesel equivalent energy}}$
- Fuel consumption in kg/hr : $\frac{\text{Engine on duration} * \text{Fuel consumtpion rate}}{1000}$
- Fuel consumption in L/h : $\frac{\text{Fuel consumption in kg/hr}}{\text{density of diesel}}$
- Total equivalent fuel in L/h : $\text{Fuel consumption in L/h} + \text{Fuel Equivalent energy in L/h}$
- Urea consumption in L/h = $\frac{\text{Total Urea consumption mass in VDI 60 cylce}}{\text{density of urea}}$

- Percentage of urea consumption = $\frac{\text{Urea consumption in L /h}}{\text{Fuel consumption in L/h}}$
- Fuel saving in year = Fuel saving in hour $*$ operating hours per day $*$ operatng days in a year
- Fuel cost saving = Fuel saving in a year * Cost of diesel per liter

Table H.2: Urea consumption in 60 VDI cycles

Case No	Fuel consumption [L]	Urea consumption		Urea consumption % w.r.t fuel consumption
		[gm]	[L]	
1	4.56	32.20	0.03	0.77
2	4.61	32.20	0.03	0.76
3	4.56	32.20	0.03	0.77
4	4.57	32.20	0.03	0.76
5	4.56	32.20	0.03	0.77
6	4.49	31.41	0.03	0.76
7	4.31	30.28	0.03	0.76
8	4.13	28.88	0.03	0.76
9	3.89	27.30	0.03	0.76
Average				0.76

-

Appendix I: Program and Data File Summary

Following images and model files are used for this thesis are mentioned in the table below:

Table I.1: Chapter 1 figure files

File name	File description
Figure 1_1.jpg	Figure 1.1

Table I.2: Chapter 2 figure files

File name	File description
Figure 2_1.jpg	Figure 2.1
Figure 2_2.jpg	Figure 2.2
Figure 2_3.jpg	Figure 2.3
Figure 2_4.jpg	Figure 2.4
Figure 2_5.jpg	Figure 2.5
Figure 2_6.jpg	Figure 2.6
Figure 2_7.jpg	Figure 2.7

Table I.3: Chapter 3 figure files

File name	File description
Figure 3_1.jpg	Figure 3.1
Figure 3_2.jpg	Figure 3.2
Figure 3_3.jpg	Figure 3.3
Figure 3_4.jpg	Figure 3.4
Figure 3_5.jpg	Figure 3.5
Figure 3_6.jpg	Figure 3.6
Figure 3_7.jpg	Figure 3.7

Figure 3_8.jpg	Figure 3.8
Figure 3_9.jpg	Figure 3.9
Figure 3_10.jpg	Figure 3.10
Figure 3_11.jpg	Figure 3.11
Figure 3_12.jpg	Figure 3.12

Table I.4: Chapter 4 figure files

File name	**File description**
Figure 4_1.jpg	Figure 4.1
Figure 4_2.jpg	Figure 4.2
Figure 4_3.jpg	Figure 4.3
Figure 4_4.jpg	Figure 4.4
Figure 4_5.jpg	Figure 4.5
Figure 4_6.jpg	Figure 4.6
Figure 4_7.jpg	Figure 4.7
Figure 4_8.jpg	Figure 4.8
Figure 4_9.jpg	Figure 4.9
Figure 4_10.jpg	Figure 4.10
Figure 4_11.jpg	Figure 4.11
Figure 4_12.jpg	Figure 4.12
Figure 4_13.jpg	Figure 4.13
Figure 4_14.1jpg	Figure 4.14
Figure 4_15.jpg	Figure 4.15
Figure 4_16.jpg	Figure 4.16
Figure 4_17.jpg	Figure 4.17
Figure 4_18.jpg	Figure 4.18
Figure 4_19.jpg	Figure 4.19

Figure 4_20.jpg	Figure 4.20
Figure 4_21.jpg	Figure 4.21
Figure 4_22.jpg	Figure 4.22
Figure 4_23.jpg	Figure 4.23
Figure 4_24.jpg	Figure 4.24
Figure 4_25.jpg	Figure 4.25

Table I.5: Chapter 5 figure files

File name	**File descripton**
Figure 5_1.jpg	Figure 5.1
Figure 5_2.jpg	Figure 5.2
Figure 5_3.jpg	Figure 5.3
Figure 5_4.jpg	Figure 5.4
Figure 5_5.jpg	Figure 5.5
Figure 5_6.jpg	Figure 5.6
Figure 5_7.jpg	Figure 5.7
Figure 5_8.jpg	Figure 5.8
Figure 5_9.jpg	Figure 5.9
Figure 5_10.jpg	Figure 5.10
Figure 5_11.jpg	Figure 5.11
Figure 5_12.jpg	Figure 5.12
Figure 5_13.jpg	Figure 5.13
Figure 5_14.jpg	Figure 5.14
Figure 5_15.jpg	Figure 5.15

Table I.6: Files used for GT-Suite® simulation model and result analysis

Filename	**File description**
Full_Powertrain_Model.gtm	GT-power simulation model setup for powertrain and after treatment using engine performance data
Aftertreatment_model.gtm	After_treatment model in GT power using engine data for simulation.
Optimzation_ Step1.gu	Results of optimization for step 1
Optimzation_ Step2.gu	Results of optimization for step 2
Optimization_Step1.xlsx	Results and plots for step1 DOE analysis and sensitivity analysis
Optimization_Step2.rar	Data files and uniplot files of the results
After-treatement_Performance.xlsx	Data and results for DOC, DPF, SCR and cold start simulation
Coldstart_Simulation.xlsx	Data summary for coldstart simulation
Ureadosing.ipz	Uniplot files for urea-dosing
Vehicle_Performance.gu	GT-post result files for powertrain performances in Chapter 5
Cost_of_after-treatment_component.xlsx	Cost calculation of after-treatment Component
Final_Results_Calculation.xlsx	Evaluation of regenerative braking, fuel consumption, energy utilization and comparison of fuel comparison for different forklift model in VDI cycle

Appendix J: Copyright Documentation

1. This permission is for Figure 2.5

To: sales@epectec.com

Subject: Permission to reproduce figure for my thesis study

May I have permission to re-use Figure "Energy Density Comparison of Size & Weight" available in https://www.epectec.com/batteries/cell-comparison.html for my Thesis topic "Optimization of Diesel Engine and After-treatment systems for Series Hybrid Forklift Application"?

Please leave this text in your reply.

Thanks in advance.

Regards,

Roman Maharjan

Graduate Student, Mechanical Engineering

Michigan Tech. University

Houghton, Michigan

rmaharja@mtu.edu

9063708775……..

Hi Roman,

I was forwarded your email. You can most certainly use that Photo for your Thesis topic. If you could please just give us a Photo Credit mention.

I appreciate you asking.

Thanks
-Keith
Keith Araujo

Director of Marketing | Epec Engineered Technologies
Office: (508) 995-5171 x1214 | Toll Free: (888) 995-5171 |
Mobile: (508) 525-5139 | www.epectec.com

2. This permission is for all the figures and tables that are taken from GT-Suite® Application

To: support@gtisoft.com

Subject: Permission to reproduce material in my MS thesis

Hi,

May I have permission to re-use Figures in GT-Power Manual and Table for reaction chemistry of after-treatment components for my Thesis topic "Optimization of Diesel Engine and After-treatment systems for Series Hybrid Forklift Application"?

Please leave this text in your reply.

Thanks in advance.

Roman

……

Hello Roman,

Thanks for asking GT about this. You can use Figures from the manual as long as you properly cite where it came from.

Regards,

-Michael

Michael Pennisi, PMP

Senior Engineer

Tel: 1(630)325-5848x292

601 Oakmont Lane, Suite 220, Westmont, IL, 60559